A STUDY ON THE SEEPAGE FAILURE OF SANDY GROUND WITH ACCOUNT FOR AIR BUBBLE DYNAMICS

December 2009

by

Hirotaka Sakai

A Study on the Seepage Failure of Sandy Ground with account for Air Bubble Dynamics

TABLE OF CONTENTS

INTRODUCTION

Part 1 Experimental Study on the Seepage Failure around Sheet Pile of Sandy Ground and Image Analysis by using Particle Image Velocimetry

Part 2 Experimental Study on the Seepage Failure of Dike with account for Air Bubble Dynamics and Rainfall

Part 3 Development of the Seepage Failure Analysis Method of Ground with Smoothed Particle Hydrodynamics

INTRODUCTION

1 General Introduction

Recently, localized torrential downpours, large-scale typhoons due to climate change, and long rainfall events have caused ruptures of river dikes, and consequently, the safety of urban areas has been threatened. The authors experienced a case in which the Shinkawa River dike in Nagoya City broke at about 3:30 on September 12, 2000, due to the Tokai Flood Disaster that started the preceding day, and areas along the river were seriously damaged (The Japanese Geotechnical Society Chubu, 2001). Eyewitness testimony describing the breakage and washout of the Shinkawa River dike mentioned (Chunichi Shinbun, 2000) that "a crack of approximately 1 m width obliquely formed across the dike and white bubbly water escaped. After that, the crack slowly expanded for about 3 hours." This testimony suggests that the progress of an actual seepage failure sometimes takes long time. As shown in Fig. 1, the breakage occurred after the maximum rainfall rate. Therefore, this suggests that the effect of bubble generation on the properties of the ground is worth investigating.

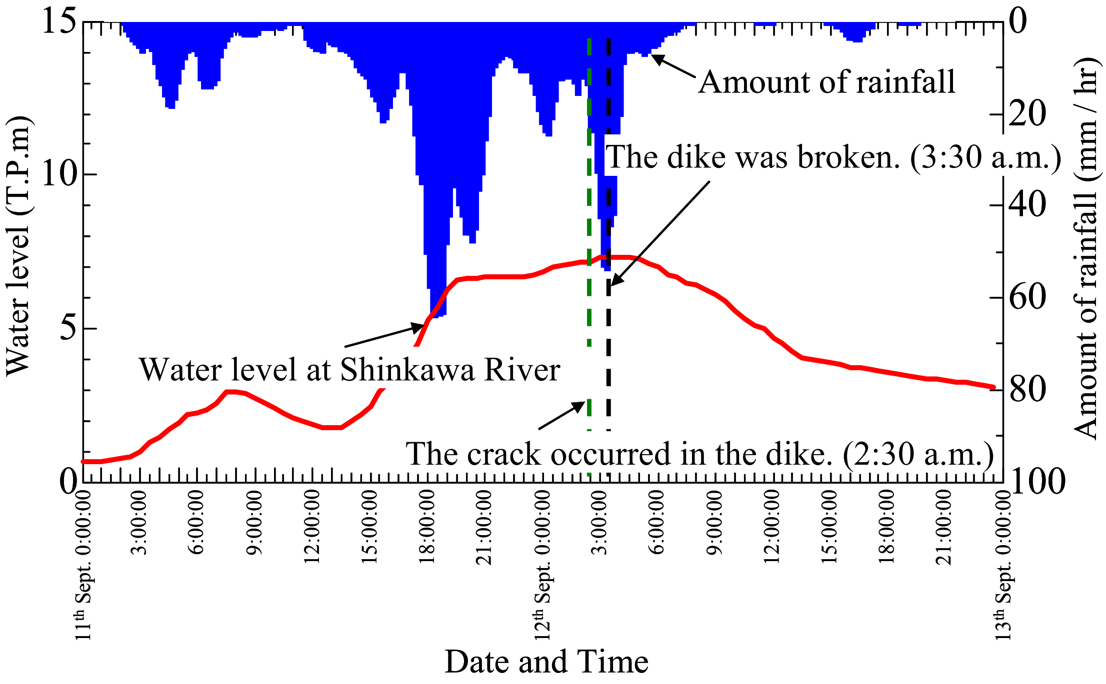

Fig. 1 Water level and hydrograph at Tokai Flood Disaster

2 Brief Review of Previous Studies

The following two sources of air are believed to exist in river dikes:

(1) Pore air. Pore air is surrounded by both a seepage line associated with rainfall and a seepage line within the dike associated with an increase in the level of the river, and consequently, pore air is captured. If the captured pore air is in a place where the curvature of the seepage line is higher than at other places, the air is then compressed along the progress of the seepage line, and released according to the prevailing conditions. This is supported by papers of Akai et al. (1977) and Ohnishi and Nishigaki (1981), in which saturated-unsaturated seepage analyses of soil structures were performed. When a water supply and discharge function was applied to this soil structure, pore air was enclosed during the seepage process. This enclosure of pore air was attributed as the cause of a hysteresis loop. This consideration is also supported by the fact that the curvature of the seepage line was larger than that of the result obtained for the saturated seepage analysis.

(2) Gas dissolved in pore water is believed to be another air source: the dissolved gas can then be eluted as bubbles. In geotechnical engineering analyses, Wheeler (1988), Sills et al. (1991), Nakajima (1985), and Kodaka and Asaoka (1994) studied seepage failures that included air bubbles. These authors report that when the amount of air dissolved in pore water is larger than the theoretical value according to Henry’s law (supersaturated), the air is eluted. When the amount of oxygen dissolved in water is large, the compressibility of pore water is high, and consequently, the seafloor is liquefied by wave action (Yamamoto, 1977; Yamamoto et al., 1978; Yamamoto, 1981; Zen and Yamazaki 1993; Miura et al., 1991). However, the detailed mechanism of liquefaction, the dynamics of air bubbles, such as deformation, development, movement, collapse, and escape from the ground, and the relationship between deformation and ground failure have not yet been sufficiently explained.

In the aforementioned papers of Nakajima (1985), Wheeler (1988), Kodaka and Asaoka (1994) and Sakai and Maeda (2007), the mechanical characteristics of ground that contains air bubbles are described. Nakajima investigated the three-phase problem in an actual dike, and concluded that pore water pressure affected void development during seepage. Kodaka and Asaoka found that high DO values contributed to air bubbles that could cause seepage failure after a long period of time, especially in coastal sandy sediments. Wheeler investigated the generation, aggregation, and development of large bubbles of gas, such as methane, in the sea-bottom floor by examining the balance among internal pressure of bubbles, pore water pressure, and surface tension. However, the detailed ground failure process associated with air bubbles, the relationships between air bubble development and macro (ground surface displacement) or micro deformations (local deformation of the ground around air bubbles) and between air bubble development and pore water pressure changes, and the effect of ground density on the abovementioned relationships, were not investigated in detail. Explaining these matters is very important for preventing and reducing ground failure disasters.

On the other hand, many analytical approaches are also tried as an unsaturated problem using FEM (Finite Element Method), such as Akai et al. (1977) and Ohnishi and Nishigaki (1981). But there is little analytical method that uses particle method in the field of the geomechanics. SPH (Smoothed Particle Hydrodynamics) method was used to obtain the combined benefits of both discrete and continuum methods. SPH is a Lagrangian method employing particles that operate in place of the mesh in finite difference solutions of partial differential equations. This method was originally developed by Gingold and Monaghan (1977) and Lucy (1977) in astrophysics to solve equations of motion for galaxies (Monaghan, 1988). Later, this method was applied to viscid flows and failure of solids (Monaghan and Gingold, 1983; Libersky et al., 1993; Monaghan, 1994; Benz and Asphaug, 1995; Randles and Libersky, 1996; Morris et al, 1997).

3 Objective and Scope

The present thesis has two main objectives: clarify the seepage failure mechanism with bubbles and proposal of the effective countermeasure of dike.

The experimental study on the seepage failure around sheet pile of sandy ground and image analysis by using Particle Image Velocimetory consists of the following subjects to be performed:

- Evaluation of DO and the Degree of Supersatuation
- Calculation of Velocity and Strain Fields of Ground
- Observation of Air Bubble
- Calculation of the Critical Hydraulic Gradient and the Hydraulic Gradient
- Measurement of Settlement in a Loading Test
- Ground Deformation based on the Amount of Ground Surface Displacement
- Changes in Critical Water-level Difference caused by Air Bubbles
- Relationship between Ground Deformation and DO the Quantity of Generated Air Bubbles, or Ground Density
- Image Analysis using Particle Image Velocimetry
- Changes in the Size and Shape of Air Bubbles
- Transformation of both Bubble and Surrounding Soil of Bubble
- Upstream Ground Deformation due to Air Bubble Escape
- Results of Water Pressure Measurement
- Air Bubble Generation on the Soil Particle Surface
- Development of Air Bubbles
- The Seepage Failure Phenomenon on Multiple Scales

The experimental study on the seepage failure of dike with account for rainfall consists of the following subjects to be performed:

- Appearance of Phreatic Lines and Bubble Development in the Dike
- Residual Height against Overflow

Development of the seepage failure analysis method of ground with Smoothed Particle Hydrodynamics consists of the following subjects to be performed:

- Continuum Continuity and Motion Equations
- Comtomioty and Motion Equations in SPH
- Equations of State for Fluids and Constitutive Models of Soil Used
- Interaction between Solid and Fluid Proposed
- Time Integration
- Treatment of Boundary
- Introduction of Suction
- Implementation for SPH Analysis
- Analytical Results and Discussions (Single-phase, Two-phases and Three-phases)

Suggestion of Countermeasure Method against Rainfall and Overflow of Dike with account for Air Bubbles consists of the following subjects to be performed:

- Experimental Results
- Analytical Results

Figure 2 indicates objective and scope of this thesis.

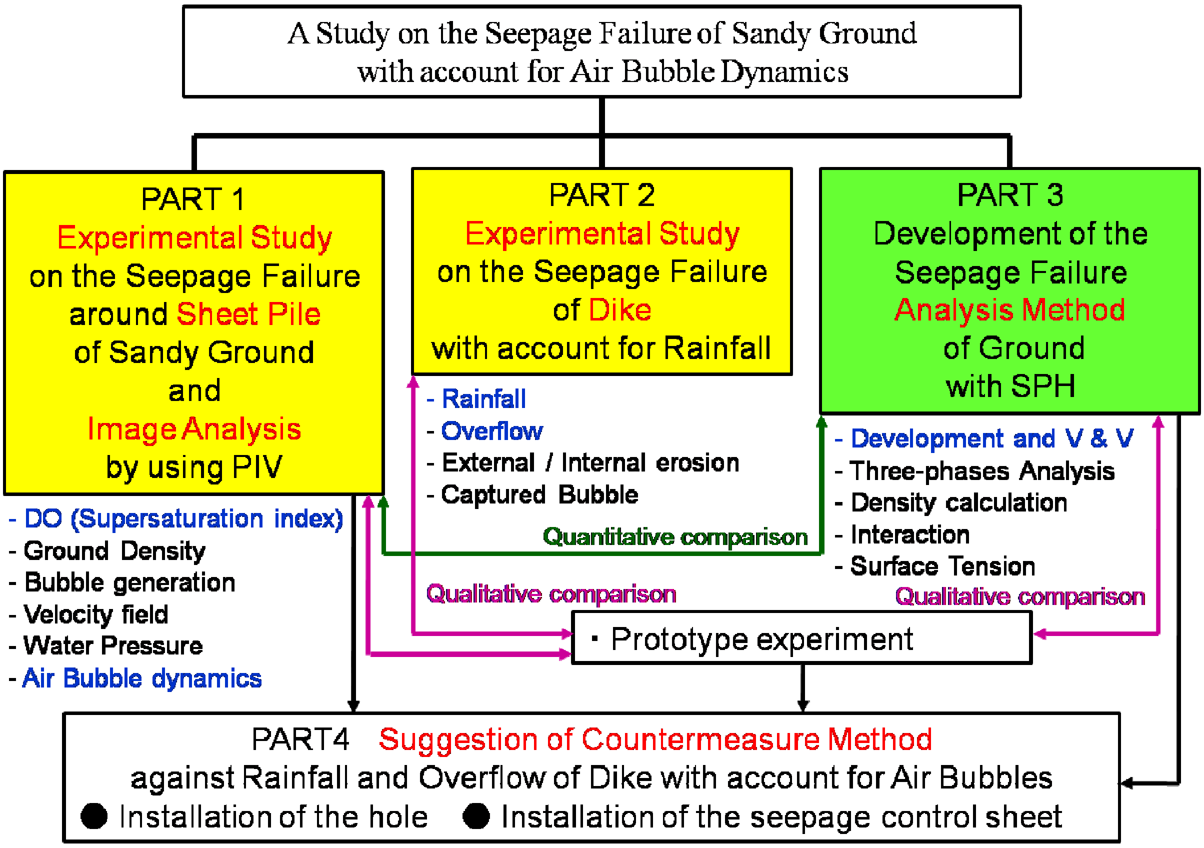

Fig. 2 Objective and Scope

4 Composition of the present thesis

The composition of the present thesis is as follows:

Part 1 Experimental Study on the Seepage Failure around Sheet Pile of Sandy Ground and Image Analysis by using Particle Image Velocimetry

In Part 1 the seepage failure phenomena around sheet pile of sandy ground. This study investigates the mechanism underlying seepage failures of ground containing air bubbles. In the study, the plane strain around a sheet pile was investigated using a model that is often used for seepage failure tests because of its well-defined experimental conditions. The experimental methods and conditions followed those of Kodaka and Asaoka. Using Particle Image Velocimetry (PIV) analysis, the relationship among air bubble dynamics, ground deformation, and failure was investigated at the micro (the bubble level) and macro scales (the whole ground).

Part 2 Experimental Study on the Seepage Failure of Dike with account for Air Bubble Dynamics and Rainfall

In Part 2 the seepage failure phenomenon of dike model. In this part, an experiment with account for rainfall was carried out to compare the seepage failure of dike. In this experiment, some geomaterial were used to compare these seepage characteristics. In addition, pore pressure and moisture content by volume were also obtaioned. The appearance of phreatic lines and buble development in the dike (especially captured bubbles) due to rainfall and overflow are investigated.

Part 3 Development of the seepage failure analysis method of ground with Smoothed Particle Hydrodynamics

In Part 3 development of the seepage failure analysis method of ground with smoothed paricle hydrodynamics. Large flowage deformations and hydraulic collapse of ground (e.g. dikes) induced by permeation of water through ground, play important roles in the destabilization of dikes during floods, liquefaction and other damage mechanisms that occur during injection driving of pile and/or improvement materials into ground. It is necessary to model progressive seepage failure in the soil in order to analyze these phenomena more precisely. In this study, the development of a new analytical method for investigation of seepage failure was attempted in order to account for interactions among all three phases of soil, water and air. The smoothed particle hydrodynamics method (SPH), a completely mesh-free technique, was used to obtain the combined benefits of both discrete and continuum methods. SPH is a Lagrangian method employing particles that operate in place of the mesh in finite difference solutions of partial differential equations. In this study, SPH with a new method for calculating density in multi-phase conditions is proposed. The seepage in the dike base is also expressed by devising equations for solid-fluid phase interactions.

Part 4 Suggestion of Countermeasure Method against Rainfall and Overflow of Dikewith ac-count for Air Bubbles

In Part 4, we propose some reinforcement methods against the influence of air bubble, rainfall and overflow. And the effects of the reinforcement are verified by both experimental approach and analitical approach. There are two reinforcement methods; one is the installation of the hole to remove air bubbles in a dike, another is the installation of the seepage control sheet with high peameability against air. First, the effect of the reinforcement of the seepage control sheet is verified by experimental approach. In this part, effect of the seepage control sheet is compared with the sheet that has low permeability against both air and water (this means the reinforcement like asphalt facing of the dike). And then, the effect of seepage control sheet that has different setting position is examined. Next, effects of two reinforcements are verified by analytical approach using Smoothed Particle Hydrodynamics. In this approach, there are two patterns to examine; one is the installation of the hole in the dike from the center of the dike to the crest, another is the installation of the seepage control sheet whole of the dike.

PART 1

Experimental Study on the Seepage Failure around Sheet Pile of Sandy Ground and Image Analysis by using Particle Image Velocimetry

Chapter 1

Seepage Failure Phenomenon around Sheet Pile of Sandy Ground

Generally, in a seepage failure situation, when the water-level difference ΔH between the upstream and the downstream sides of a dike is defined as the external force causing the failure, and the critical water-level difference ΔH_{cr} across the dike is defined as the force's strength, the failure is said to occur at the time $\Delta H = \Delta H_{\mathrm{cr}}$ because of an increase in the water-level difference, ΔH. Figure 1.1.1 shows an experimental model that is often used for describing seepage failure. In this model, water seepage near an impermeable sheet pile can be readily observed. When the water-level difference reaches a certain value, seepage failure occurs. The water-level difference ΔH when seepage failure occurs is defined as ΔH_{cr}. When $\Delta H < \Delta H_{\mathrm{cr}}$, the ground is stable.

However, the above-mentioned Shinkawa River breakage differed from general seepage failure phenomena, since it did not occur when the water-level difference was the largest (1 h before the peak time). Rather, this seepage failure developed slowly, and bubbles were observed. Actually, a number of seepage failures accompanied by air bubbles have been witnessed in the past, and these types of phenomena have been said to mimic "a toad blowing bubbles." Moreover, a phenomenon has been reported in which a large quantity of air bubbles blew off from the inside of an old deversoir at the time of overflow. Approximately 30% of river dikes in Japan are reported to be insufficiently safe against seepage failure (Ministry of Land, Infrastructure, Transport and Tourism, 2004). When the added effect of air bubbles is taken into consideration, a higher percentage of river dikes may in fact be facing the possibility of seepage failure. Therefore, a full understanding of the mechanism of river dike seepage failure, which includes the effect of air bubbles, is very important, and countermeasures against this type of seepage failure are urgently required.

This study investigates the mechanism underlying seepage failures of ground containing air bubbles. In the study, the plane strain around a sheet pile was investigated using a model that is often used for seepage failure tests because of its well-defined experimental conditions. The experimental methods and conditions followed those of Kodaka and Asaoka. Using Particle Image Velocimetry (PIV) analysis, the relationship among air bubble dynamics, ground deformation, and failure was investigated at the micro (the bubble level) and macro scales (the whole ground).

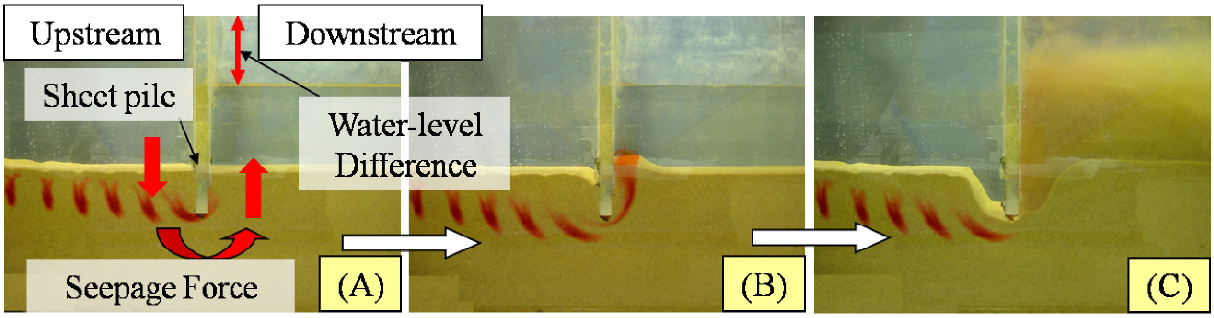

Fig.1.1.1 The well-known seepage failure phenomenon

Chapter 2

Methods of the Experimental Study

2.1 Experimental Apparatus and Procedure

To investigate the generation of air bubbles, the experimental apparatus shown in Fig. 2.1.1 was manufactured. Toyoura sand ($e_{\max}$ = 0.97, $e_{\min}$ = 0.60, and G_s = 2.65) and tap water were used for the experiment. After arranging a loose three-layer simulated ground using Toyoura sand dropped into the water, the ground's relative density was controlled by the number of compactions applied by a tamping rod. The compaction numbers per layer of middle and dense ground are 78 and 480 times, respectively. Figure 2.1.2 shows the relative density and the number of compactions. The penetration depth of the sheet pile was set to be 50 mm, and the temperature of the tap water stored in the primary tank was controlled using a thermo-regulator. During the experiment, the water temperature, the DO value in the experimental soil tank, and the permeable water volume were measured. The DO value was controlled by an aquarium aerator, which is installed in the secondary tank (Fig. 2.1.1). A preliminary experiment determined how the measured DO value increased with the output volume of air from the aerator. A tensiometer was installed in the experimental soil tank (Fig. 2.1.1). The excess pore water pressure ratio was obtained by dividing the measured value of pore water pressure by the initial vertical effective stress σ'_{v0}.

Table 2.1.1 shows the details of the seepage water tests. To study water level changes, three tests were performed: a monotonic raising test, in which the water-level difference was gradually raised, similar to general seepage failure tests (without bubbles); a holding test, in which the water-level difference was maintained at a certain value (with bubbles); and a re-raising test, which corresponds to the creep test in dynamic tests (with bubbles).

In the monotonic raising test, the water level at one side of the sheet pile (upstream) was raised, and the critical water-level difference ΔH_{cr} at which seepage failure occurred was investigated in different ground densities without air bubble generation. The water level was maintained for 5 min after each rise, because after the water level was raised, ground displacement continued for approximately 1 min (similar to the creep phenomenon). By pausing in between water level rises, the water-level difference could be precisely measure when seepage failure occurred. In addition, deformation does not occur until 100 mm of water-level difference at all. The first water level rise was 50 mm. It was 10 mm in the middle of the test, and the final water rise was 5 mm. This alternate raising and holding of the water level was repeated until seepage failure occurred, and the elapsed time was expressed as $t_{raising}$ (Fig. 2.1.3(I)). Table 2.1.1 shows the water-level difference between the upstream and downstream sides when seepage failure occurred (the critical water-level difference) at different ground densities.

In the holding test, the water-level difference below the critical water-level difference (ΔH was 60%–85% of ΔH_{cr}) was maintained for as long as 114 hours. During this period, air bubbles were generated within the ground. The time at which the water-level difference was set was 0 hour, and the elapsed time was $t_{holding}$ (Fig. 2.1.3(II)). In addition, the water level was raised until it reached a predetermined water-level difference ΔH, similar to the monotonic raising test. Table 2.1.2 shows the experimental conditions for the holding test. In this test, the conditions around the sheet pile were recorded every 15 min using a digital camera (approximately 8 million pixels). In the re-raising test, after the holding test was completed, and if the ground had not failed, the water level was raised from that of the holding test, and the water-level difference when seepage failure occurred was investigated. The elapsed time of this test was expressed as t (Fig. 2.1.3(III)).

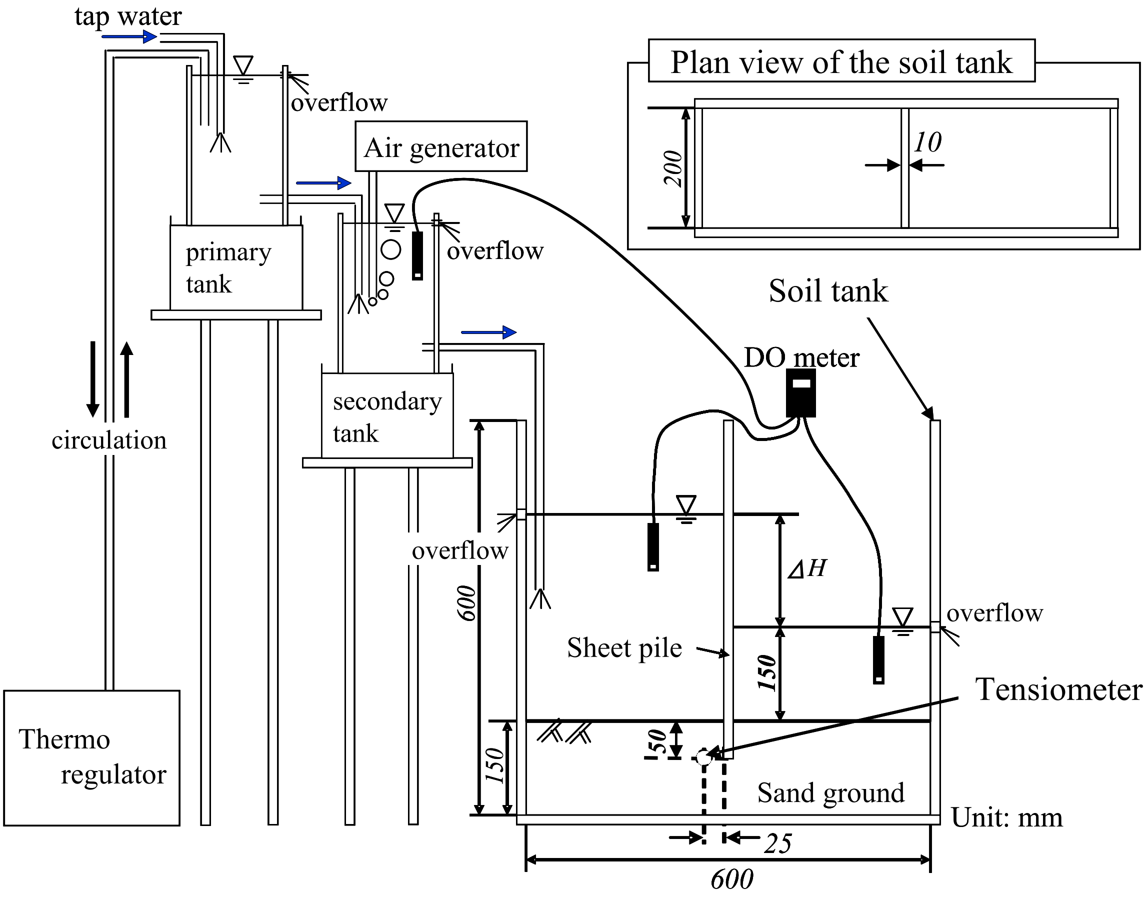

Fig.2.1.1 Experimenal apparatus of seepage failure experiment around sheet pile

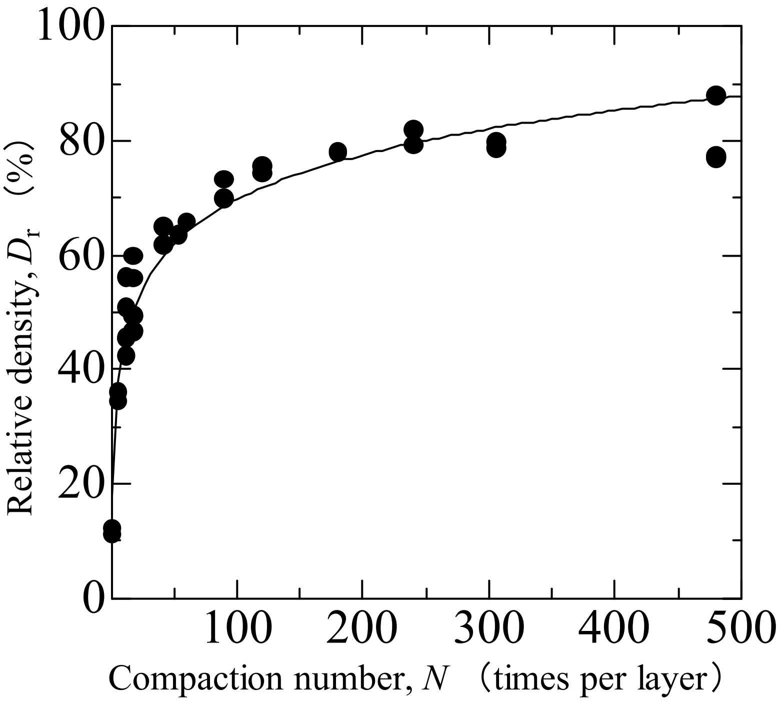

Fig.2.1.2 Relationship between relative density and compaction number

Table 2.1.1 The scheme of seepage failure tests

Existence of Bubble	Ground Condition	
	Loose (Dr = 14%)	Dense (Dr = 81%)
Without air bubbles	[Monotonic raising test] ΔH_{cr} = 142mm (=const.) $\delta(\Delta H) \geq 0$	[Monotonic raising test] ΔH_{cr} = 194mm (=const.) $\delta(\Delta H) \geq 0$
With air bubbles	[Holding test] ΔH = 100 or 120mm (=const.)	[Holding test] ΔH = 140 or 170mm (=const.)
	[Re-raising test] $\delta(\Delta H) \geq 0$	[Re-raising test] $\delta(\Delta H) \geq 0$

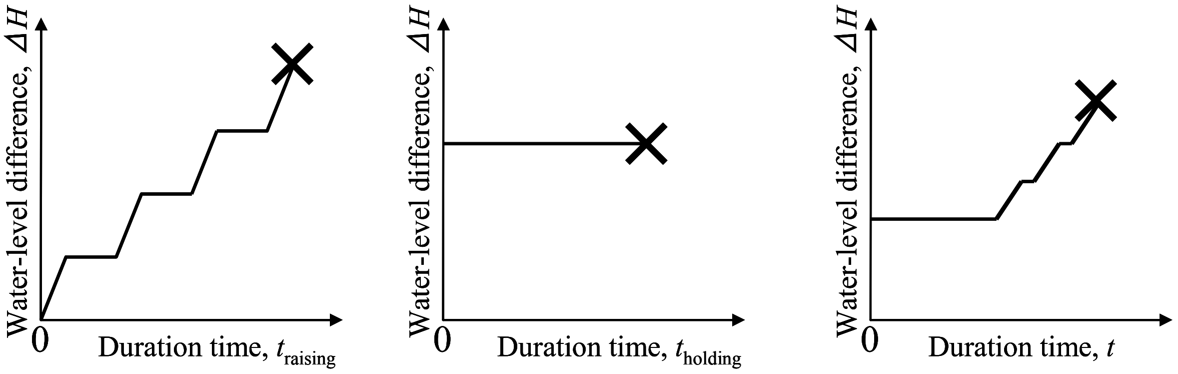

(I) Monotonic raising

(II) Holding

(III) Re-raising

Fig.2.1.3 The type of hydraulic surcharge employed in the test

Table 2.1.2 Experimental conditions (holding test)

Case	Density	ΔH (mm)	$\Delta H/\Delta H_{\mathrm{cr}}$	DO	failure	Holding time up to failure (hour)
L-1	Loose	120	0.85	Supersaturation	No	—
L-2	Loose	120	0.85	Saturated	Yes	38
L-3	Loose	120	0.85	Unsaturated	Yes	94
L-4	Loose	100	0.70	Unsaturated	No	—
D-1	Dense	170	0.89	Supersaturation	Yes	95
D-2	Dense	170	0.89	Saturated	Yes	114
D-3	Dense	170	0.89	Unsaturated	Yes	18
D-4	Dense	140	0.73	Supersaturation	No	—

2.2 Evaluation of DO and the Degree of Supersaturation

Because dissolved gas in pore water primarily consists of nitrogen and oxygen, the pore water DO was measured in this study. In general, the critical mass of gas dissolved in a solvent (its solubility) can be expressed by the mole fraction m of the gas in the solvent (The chemical Society of Japan, 2004). When the gas partial pressure is 1 atmosphere, the following equation can be used:

$$\ln(m) = A + B/(T/100) + C\ln(T/100) \tag{2.2.1}$$

where T expresses the absolute water temperature, and A, B, and C are constants related to the gas and solvent. When the gas is oxygen and the solvent is water, A, B, and C are –66.735, 87.475, and 24.453, respectively. The mole fraction m is then converted into the DO saturation value. Figure 2.2.1 shows the relationship between DO (saturation DO: DO_{sat}) and water temperature. In addition, this figure includes some plots of DO values in nature. Generally speaking, when oxygen is dissolved until it reaches the critical value calculated by Eq. (2.2.1), or the saturation state.

However, in nature, more gas is often dissolved in a solvent than is indicated by the critical value (called supersaturation) because of a change in water temperature or pressure. In Fig. 2.2.2, most river water is saturated or supersaturated (Ministry of Land, Infrastructure, Transport and Tourism, 2008). As shown in Fig. 2.2.2(II), whether pore water is supersaturated can be judged by the difference between the measured DO values and the saturated DO value; that is, $DO - DO_{\mathrm{sat}}$. When this value is positive, the water is supersaturated. As shown in Fig. 2.2.2(I), the DO and DO_{sat} values change substantially depending on the water temperature. Therefore, this study considered fluctuation relative to DO_{sat} as shown in Eq. (2.2.2) and defined the index of supersaturation I_{ss} as follows:

$$I_{ss} = \{(DO - DO_{sat}) / DO_{sat}\} \times 100 \tag{2.2.2}$$

As shown in Fig. 2.2.2(III), even if water temperature changes, this index can identify supersaturated and unstable DO values.

Figure 2.2.3 shows the relationship between I_{ss} and water temperature, which was obtained using Eq. (2.2.2) relating DO and temperature of water body in nature and the frequency distribution of I_{ss}. As shown in this figure, I_{ss} in an actual body of water is mostly distributed between –20% and 20%, and supersaturation is not unusual in the natural world.

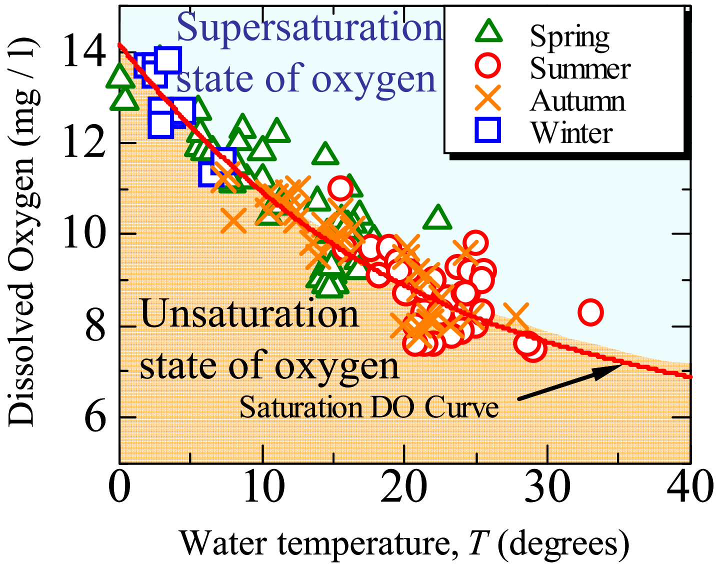

Fig.2.2.1 Dissolution state of oxygen with saturation DO curve and DO values in a typical class A river in Japan

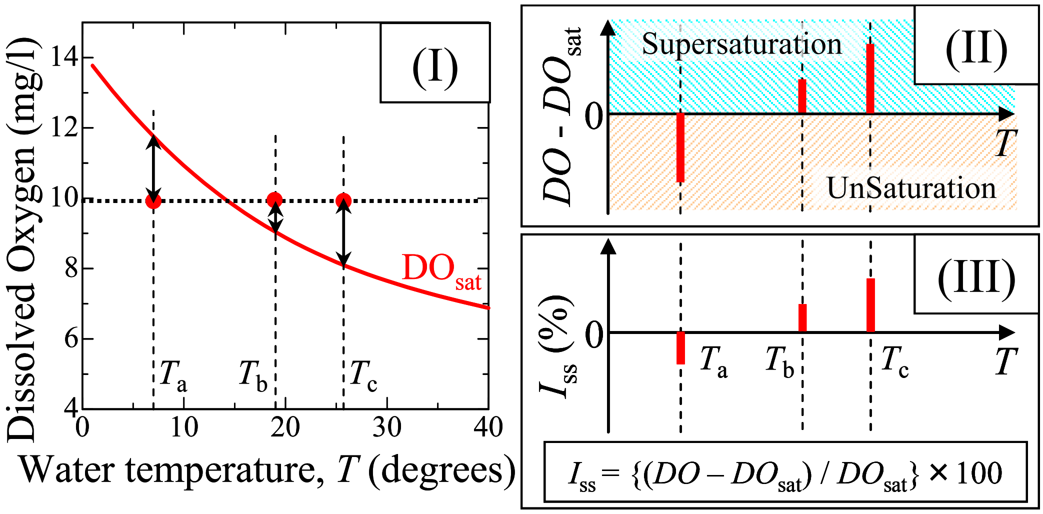

$$I_{ss} = \{(DO - DO_{sat}) / DO_{sat}\} \times 100$$

Fig.2.2.2 Introduction of "Index of supersaturation: I_{ss}"

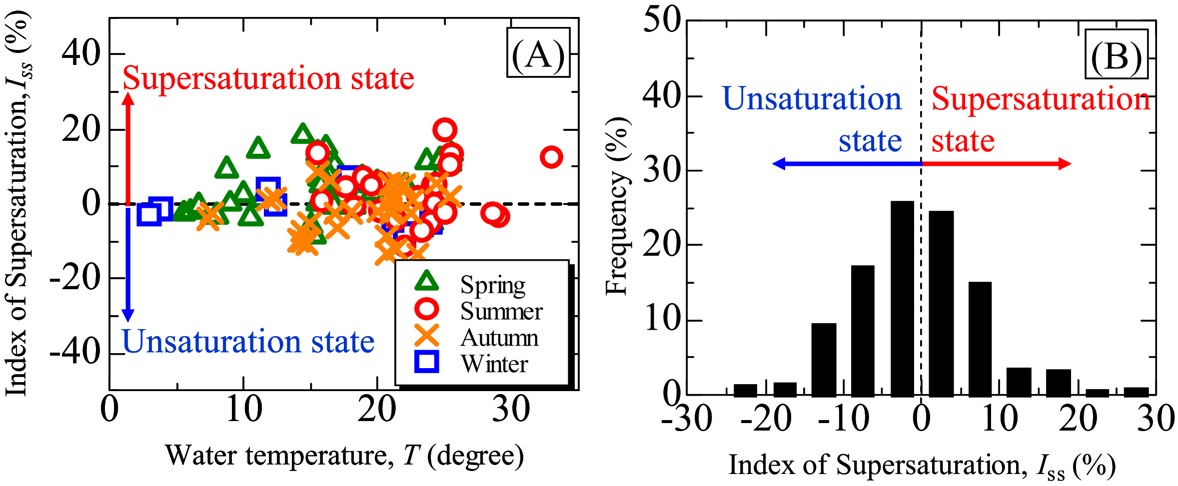

Fig.2.2.3 Index of supersaturation in nature: (A) I_{ss} of typical class A river in Japan (B) Frequency of I_{ss}

2.3 Calculation of Velocity and Strain Fields of Ground

Based on the photographs taken in the experiment, the velocity distribution of the ground was calculated using Particle Image Velocity (PIV) analysis. PIV is an analytical method in which the brightness values of two photographs taken at different times are measured, and tracer particle movements (here, Toyoura sand) are calculated based on the differences between the brightness values of the two photographs (The Visualization Society of Japan, 2002). Based on the results of the PIV analysis, the maximum shear strain rate can be expressed. Since PIV can be used to obtain the velocity of a lattice point fixed in space, the strain rate on an element was obtained, assuming that the velocity in the lattice was linearly distributed.

2.4 Observation of Air Bubble

In photographs of the ground in which air bubbles were generated (The left side of Fig. 2.4.1: *D* marked on the figure means initial penetration depth of the sheet pile), air bubbles are obviously darker than the soil particles, which allowed the two-dimensional quantity of bubbles to be analyzed. This image was divided into a fine lattice with a pixel unit grid, and the difference in brightness between the ground and air bubbles was determined. The air bubbles' area and the change in their shape were also analyzed. Although the analytical accuracy depends on the photograph resolution, this study could detect air bubbles of 0.2 mm diameter or larger, was and this size was almost equal to that of the average diameter D_{50} of the Toyoura sand. Since Kamiya et al. (1996) reported that the void diameter of sandy soil was 20%–30% of the average particle diameter, the void diameter of Toyoura sand was approximately 0.05 mm. Therefore, the air bubbles detected were considered to be clogged voids of Toyoura sand that accumulated and expanded.

Terzaghi (1942) reported that heaving and seepage failure of downstream ground occurred within $D/2$–D when the penetration depth of the sheet pile was expressed as *D*. A similar result was obtained in the present study, in which the area of air bubbles in the square of width *D* on the downstream side (the square shown in the left side of Fig. 2.4.1) was analyzed. The right side of Fig. 2.4.1 shows an example of the results obtained with the air bubble analysis. In a photograph, distortion generally arises near the margin owing to the influence of the lens, and consequently, these parts become darker than the rest of the photo. Therefore, we cut off 15% of each margin and analyzed the area surrounded by the dashed line so that the analytical result clearly expresses the only distribution of air bubbles. In this study, it is assumed that the bubble existence percentage in direction of depth is homogeneous in an arbitrary section.

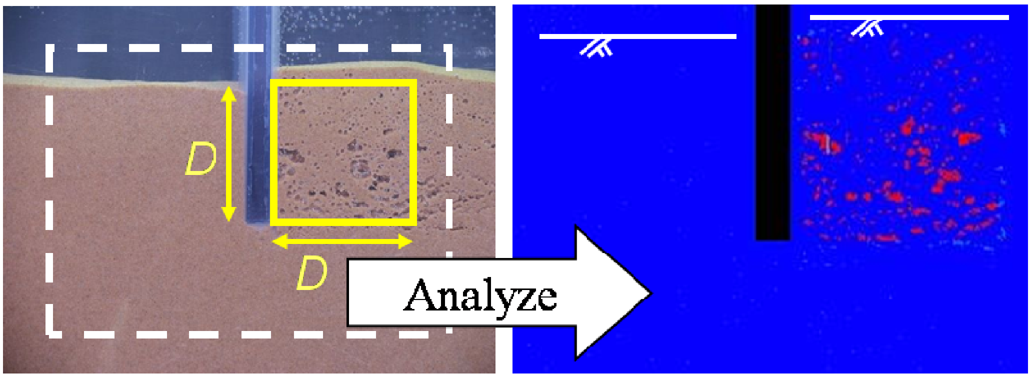

Fig.2.4.1 Example of bubble area calculation

2.5 Calculation of the Critical Hydraulic Gradient and the Hydraulic Gradient

In general, the critical hydraulic gradient i_{cr}, when ground seepage failure occurs in a one-dimensional vertical upward flow, is expressed as follows:

$$i_{cr} = (G_s - 1)/(1 + e) \tag{2.5.1}$$

where G_{s} expresses the specific gravity of the ground particles and e expresses the void ratio. The area of air bubbles is obtained from a two-dimensional sample of the soil tank surface (or observation surface). Based on the air bubble area obtained, the simple void ratio was calculated. Then, using the downstream side of the sheet pile (the square shown in the left side of Fig. 2.4.1) when the test was initiated, the critical hydraulic gradient was calculated using Eq. (2.5.1) and the obtained void ratio. The ground particle specific gravity G_{s}=2.65 was used.

The calculation procedure was as follows: (1) the initial pore area in the calculating area was determined with the initial void ratio, and (2) after adding the air bubble generation area, the newly obtained area with initial bubbles was converted into the final void ratio. All of the air bubble volume generated in the area used for calculations was assumed to substitute for the soil particle volume without considering the influence of dilatancy.

The hydraulic gradient i in a one-dimensional flow can be expressed with the following equation.

$$i = \Delta H / L \tag{2.5.2}$$

where the water-level difference ΔH is a fixed value for the holding test. However, since displacement occurs on the ground surface at both the upstream and downstream sides, a change in the seepage distance must be considered. The hydraulic gradient i was therefore calculated by calculating the seepage distance L in the ground shown in the photograph. In general, a seepage failure is very local and the shear strength of the ground is very important. However, for simplification, one-dimensional seepage was assumed for the current study.

2.6 Measurement of Settlement in a Loading Test

For a simple evaluation of the strength of ground in which air bubbles were generated, cylinder-shaped weights (20 mm in diameter and 10 mm in height, made of aluminum) were piled on the ground surface (Fig. 2.6.1). The experimental procedure is as follows: first, a hollow cylinder is put on the ground surface. Second, a cylinder-shaped weight is placed in the hollow cylinder, then, the ground subsidence is measured. After completing the first measurement, the next weight is added to the cylinder. Special attention was paid to prevent impacts during the piling of the weights.

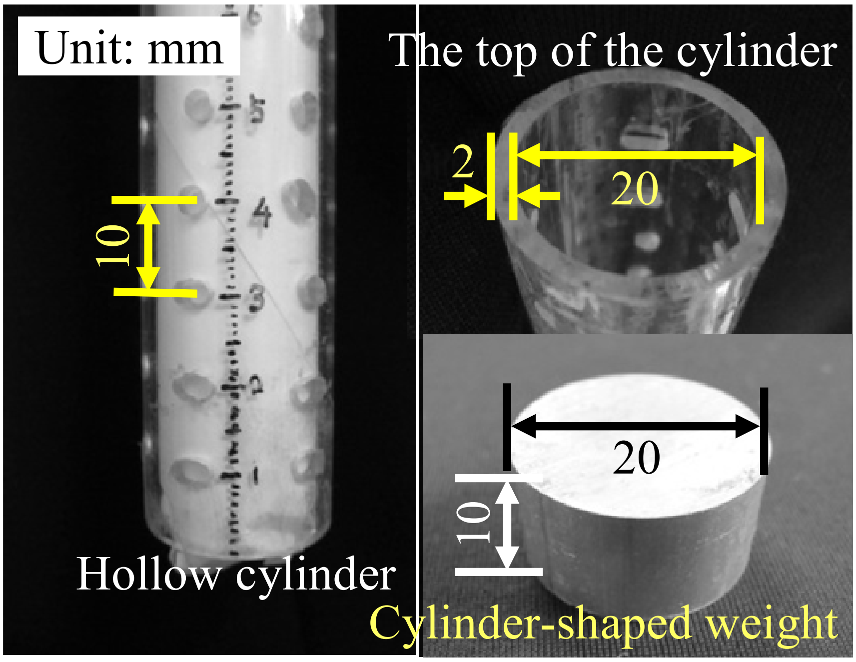

Fig.2.6.1 Loading test apparatus

Chapter 3

Seepage Failure Phenomenon in Macro Scale

3.1 Ground Deformation Based on the Amount of Ground Surface Displacement

Figure 3.1.1 shows the change in ground surface displacement of loose and dense ground in a monotonic raising test. As shown in Fig. 1.1.1, displacement occurred before seepage failure. In this study, ground failure was defined as the time when “sand boiling” occurs, and the “×” in Fig. 3.1.1 indicates the failure point. As shown in this figure, water-level differences of 125 and 175 mm for loose and dense grounds, respectively, were achieved before a clear displacement occurred on the ground surface on the upstream side in normal seepage failure. These differences were 80%–90% of the critical water-level differences shown in Table 2.1.1. Moreover, the amount of ground subsidence upstream was equal to the amount of uplift downstream.

Figure 3.1.2 shows ground deformation around the sheet pile in the holding test (Cases L-3 and D-1). Air bubbles developed around the sheet pile as time proceeded. In loose ground, air bubbles were distributed around the sheet pile upstream and downstream. In the dense ground, air bubbles were only downstream.

Fig. 3.1.3(A) shows the amount of ground surface displacement at upstream and downstream. Unlike the seepage failure phenomenon in ground without air bubbles shown in Fig. 3.1.1, when the ground contained air bubbles, the ground surface deformed and repeatedly subsided and uplifted. Finally, failure would occur after a long period of time even though the water-level difference was maintained at a stable value less than ΔH_{cr}. This failure is similar to creep phenomena. Although ground density did not appear to influence ground surface displacement on the downstream side, the degree of displacement on the upstream side prior to failure was larger in dense ground than in loose ground. On the other hand, no large difference was observed in the displacement of loose and dense ground at the downstream side, even after a long period of time. The reason for this could be that the generation of air bubbles disregarded the downstream ground density. In loose ground, the upstream ground rose when the test was initiated (Fig. 3.1.2), likely because air bubbles were even generated in the ground upstream and raised the ground.

Fig. 3.1.3(B) plots the ground surface displacement when seepage failure did not occur even after the holding test. In this case, the ground upstream was not deformed at all even though air bubbles were generated in the ground downstream and the ground was degraded. However, because no subsidence was observed in the ground upstream, the effect of air bubbles did not reach upstream. However, when the deformation reached upstream, failure rapidly occurred. In other words, failure of ground affected by air bubbles does not occur until the upstream ground starts to subside, regardless of the existence of air bubbles on the downstream side. However, as shown Fig. 3.1.2, the ground subsidence in this case was localized and was larger in dense ground then in loose ground. Therefore, when monitoring is performed on full-size structures, a system that can measure displacement of a large area or can predict deformation by numerical analysis is required.

As shown in Fig. 3.1.3(A), the dense ground on the upstream side did not deform at all for a long period of time, and then deformation suddenly started at about 55 hours. On the other hand, this tendency was not observed in loose ground. Therefore, the time between failure signs and actual failure was short in dense ground. Regarding safety management for seepage failure of soil structures, it is important to monitor upstream ground deformation, regardless of the existence of air bubbles. Subsidence causes for ground failure on the upstream side are described later.

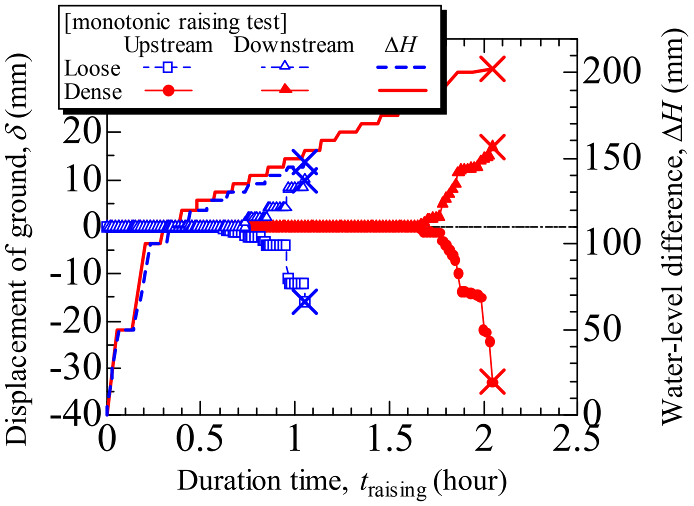

Fig.3.1.1 Relationship between water-level difference and ground displacement (monotonic raising test)

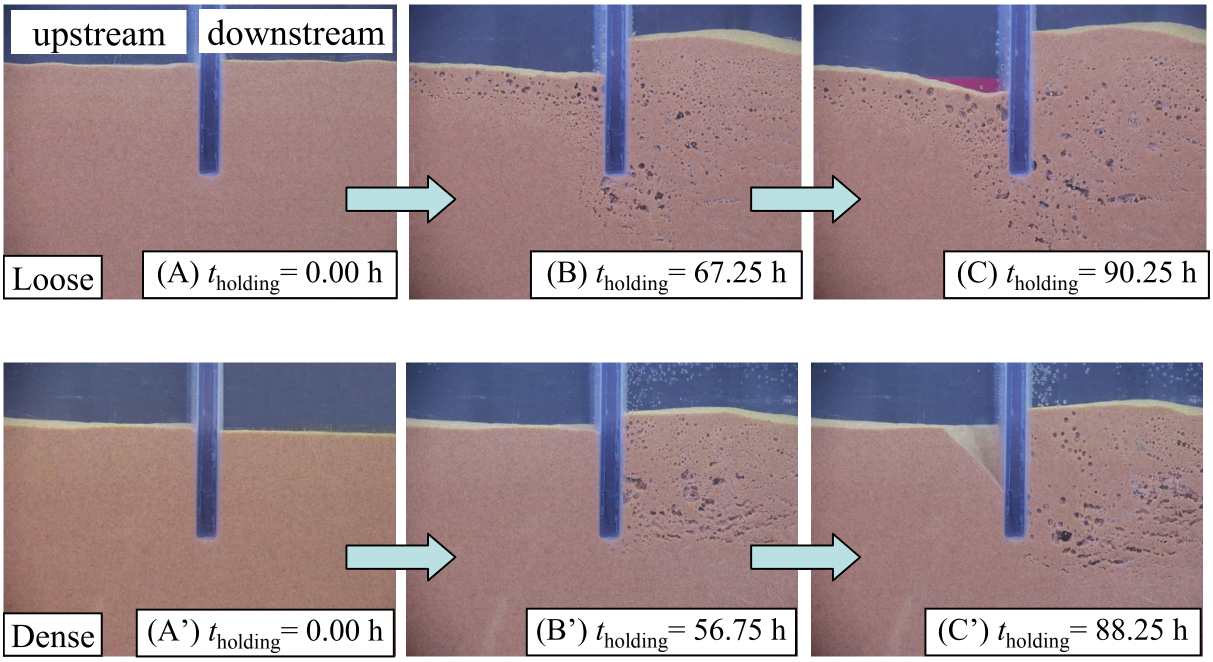

Fig.3.1.2 Deformation of ground around sheet pile due to generation and evolution of air bubbles (Loose: Case L-3 Dense: Case D-1)

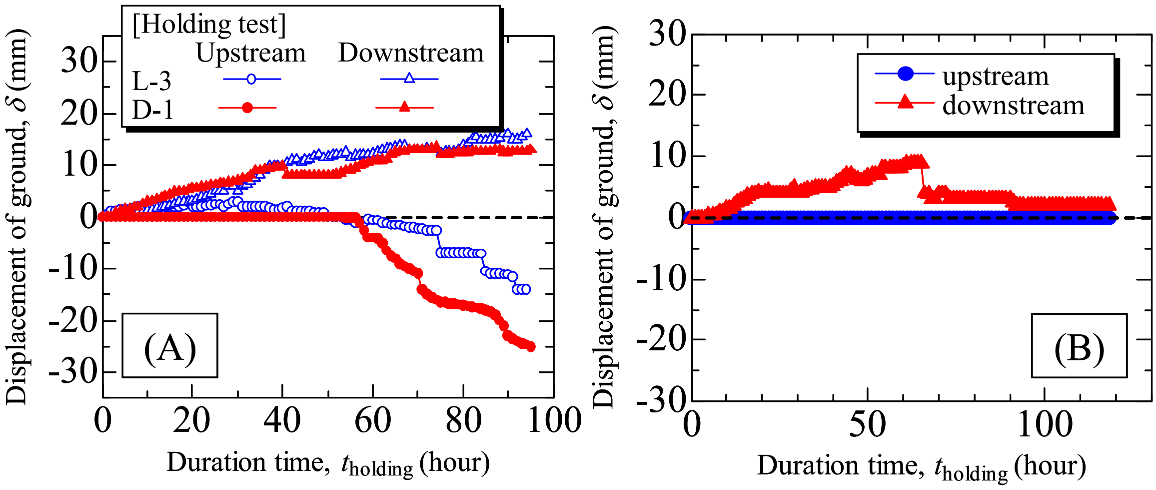

Fig.3.1.3 Amount of ground displacement: (A) holding test (B) Case D-4 (non-failure)

3.2 Decrease in Critical Water-level Difference caused by Air Bubbles

Figure 3.2.1 shows temporal changes of the ratio of water-level difference ΔH to the critical water-level difference ΔH_{cr} until seepage failure in all of the tests (monotonic raising, holding, and re-raising tests). In the monotonic raising test, seepage failure did not occur until $\Delta H_{\mathrm{cr}} = \Delta H$. As indicated by Kodaka et al., seepage failure occurred after a long period of time even when $\Delta H_{\mathrm{cr}} > \Delta H$ in the holding test. In this study, even for the holding test case in which no seepage failure occurred for a long period of time, during the re-raising test when the water level was raised again, seepage failure occurred even if $\Delta H_{\mathrm{cr}} > \Delta H$. This is a new finding. In other words, ground strength against seepage failure was reduced in ground that contained air bubbles.

For a simple evaluation of the ground's degree of degradation, the relationship between settlement and loading pressure was investigated. As shown in Fig. 3.2.2, although the settlement of ground without air bubbles was approximately 8 mm, settlement increased with loading pressure in the ground with air bubbles. Settlement increased as the number of air bubbles increased, and the final settlement of the ground with more air bubbles was 5 times that of the ground without air bubbles. Therefore, a decrease in strength against seepage failure as a result of air bubbles was demonstrated. Unlike in normal load tests, a tendency towards a gradual decrease in settlement was observed. The reason for this could be that the settlement test was performed near the sheet pile, and consequently, lateral displacement was confined.

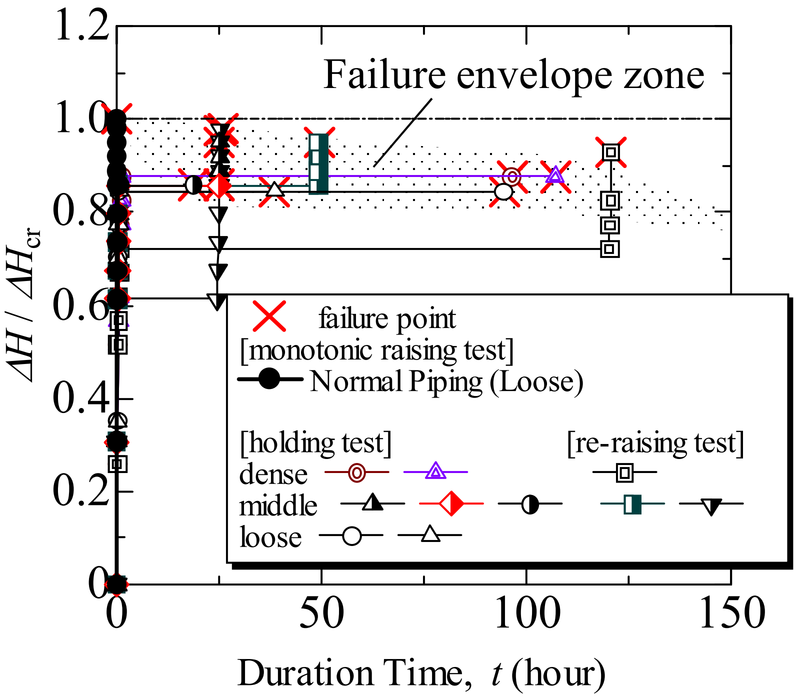

Fig.3.2.1 Real water-level difference (ΔH) to critical water-level difference (ΔH_{cr}) (Decrease in ground strength)

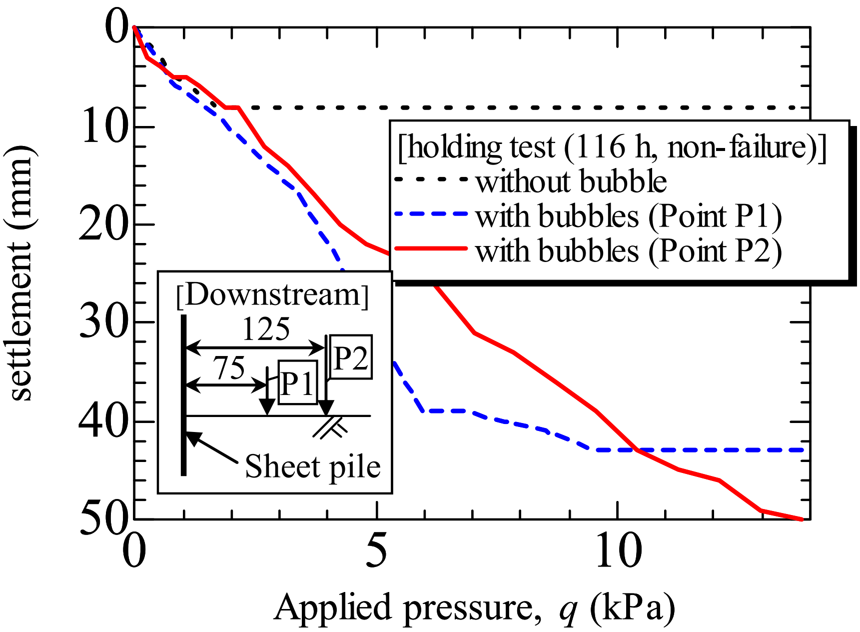

Fig.3.2.2 Relationship between settlement and loading pressure

3.3 Relationship between Ground Deformation and I_{ss}, the Quantity of Generated Air Bubbles, or Ground Density

The relationship between ground deformation and the quantity of air bubbles generated was investigated.

Figures 3.3.1 and 3.3.2 show temporal changes in I_{ss} and the quantity of air bubbles generated in ground of various densities on the downstream side in holding tests. As shown in these figures, I_{ss} upstream was between 5% and 10%, similar to values of an actual body of water. The maximum quantity of air bubbles generated was larger in L-1, D-1, and D-4 than in the other ground types, and the upstream areas of these three cases were supersaturated. Moreover, the quantity of air bubbles generated became smaller as the average I_{ss} decreased. The quantity of air bubbles generated sometimes decreased when air bubbles exited the ground (details described later).

Figure 3.3.3 shows temporal changes in the quantity of air bubbles prior to their escape from ground of various densities. In loose ground, the duration until air bubble generation was shorter and the development speed was faster as I_{ss} was higher. In denser ground, no clear difference was observed in the length of time prior to air bubble generation, and air bubbles were generated early in all ground types. Therefore, the effect of density was larger than the effect of the degree of supersaturation on air bubble generation. In case D-3, air bubble generation was observed although the water was undersaturated. This observation indicated that air bubble generation was affected not only by the degree of pore water supersaturation but also by contact between water and soil particles during seepage and by a slight pressure fluctuation. A possible reason for this is that because dense ground contains more particles than loose ground per unit area, water is more often agitated by contact with particles in dense ground. In other words, air bubbles are primarily generated by contact between water and soil particles, and the generation speed is faster in higher ground density and higher I_{ss}, so a difference in the degree of supersaturation clearly appears in loose ground. In cases L-1 and D-1, there was a point at which the air bubble generation speed changed (indicated by a circle in Fig. 3.3.3).

Temporal changes in ground surface displacement were investigated for every ground type with different densities in detail to clarify the relationship between ground surface displacement and the quantity of air bubbles on the downstream side. In Fig. 3.3.4, the ground surface displacement and the quantity of air bubbles generated in cases L-3 and D-1 at the downstream side are shown. Although the water-level difference was maintained at a fixed value, deformation occurred in the ground downstream, accompanied by the generation and development of air bubbles. Air bubbles intermittently escaped from the ground regardless of the ground density, and the ground surface on the downstream side subsided as air escaped. This was more noticeable in dense ground than in loose ground. Therefore, not only the generation and development of air bubbles but also the ground surface displacement when air bubbles escaped were important for seepage failure.

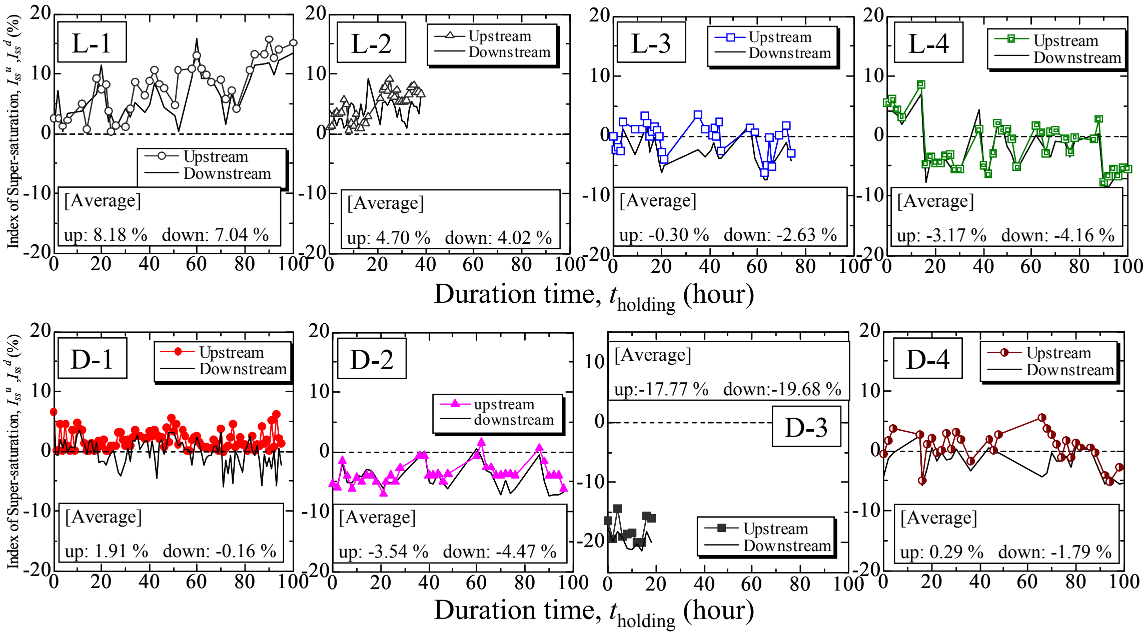

Fig.3.3.1 Changes in supersaturation index (constant water-level difference)

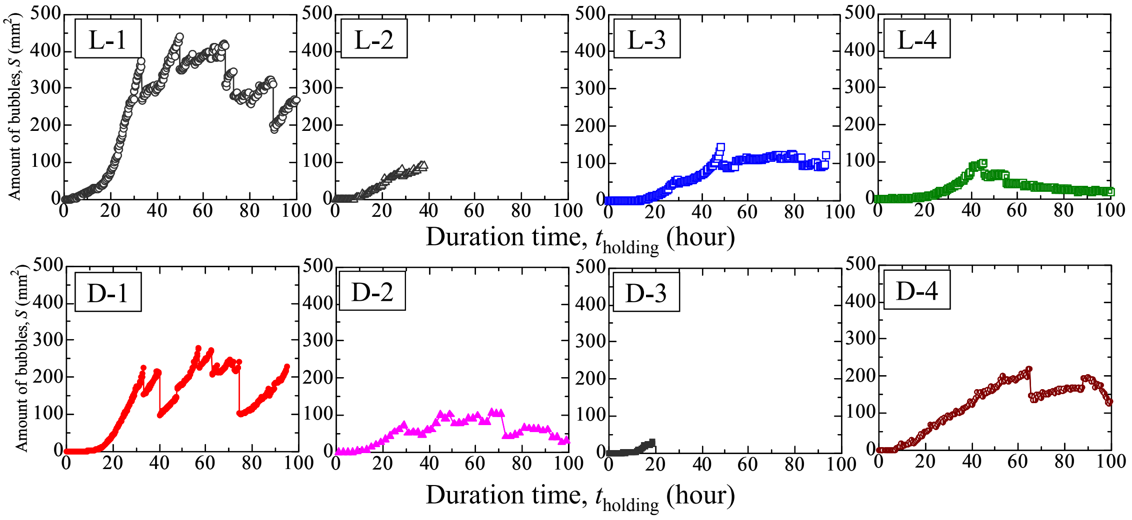

Fig.3.3.2 Changes in amount of bubbles (constant water-level difference)

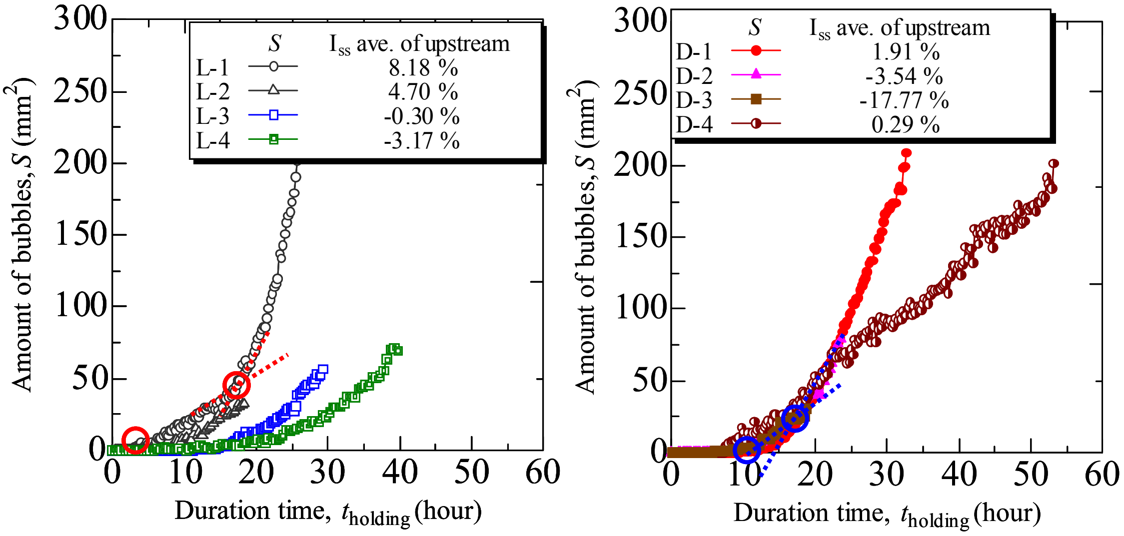

Fig.3.3.3 Quantity of downstream bubbles of each density from start to bubble blow off of the first time

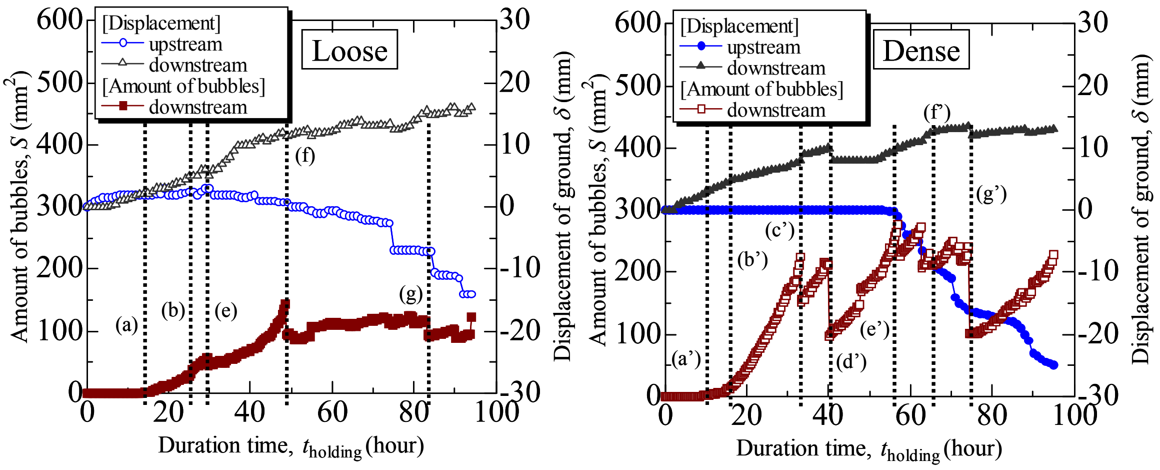

Fig.3.3.4 Changes in ground displacement and quantity of bubbles (Loose: Case L-3 Dense: Case D-1)

3.4 Image Analysis using PIV (Macro)

Figure 3.4.1 shows results of the PIV analyses and the maximum shear strain rates calculated from the velocity vector obtained from PIV analysis in case of L-3 and D-1. These analytical results indicate that the maximum speed of soil particles at the tip of the sheet pile was 8.3×10^{-7} m/s in loose ground and 7.5×10^{-8} m/s in dense ground; that is, the speed in dense ground was approximately an order of magnitude slower than in loose ground. This could have been because soil particle movement was more confined in dense ground than in the loose ground.

From the lower side in Fig. 3.4.1, the maximum shear strain rates were 4.1×10^{-2} 1/s in loose ground and 2.0×10^{-3} 1/s in dense ground. The shear strain rate was distributed widely and in homogeneously, centering on the sheet pile. The existence of air bubbles caused complicated deformations in the ground.

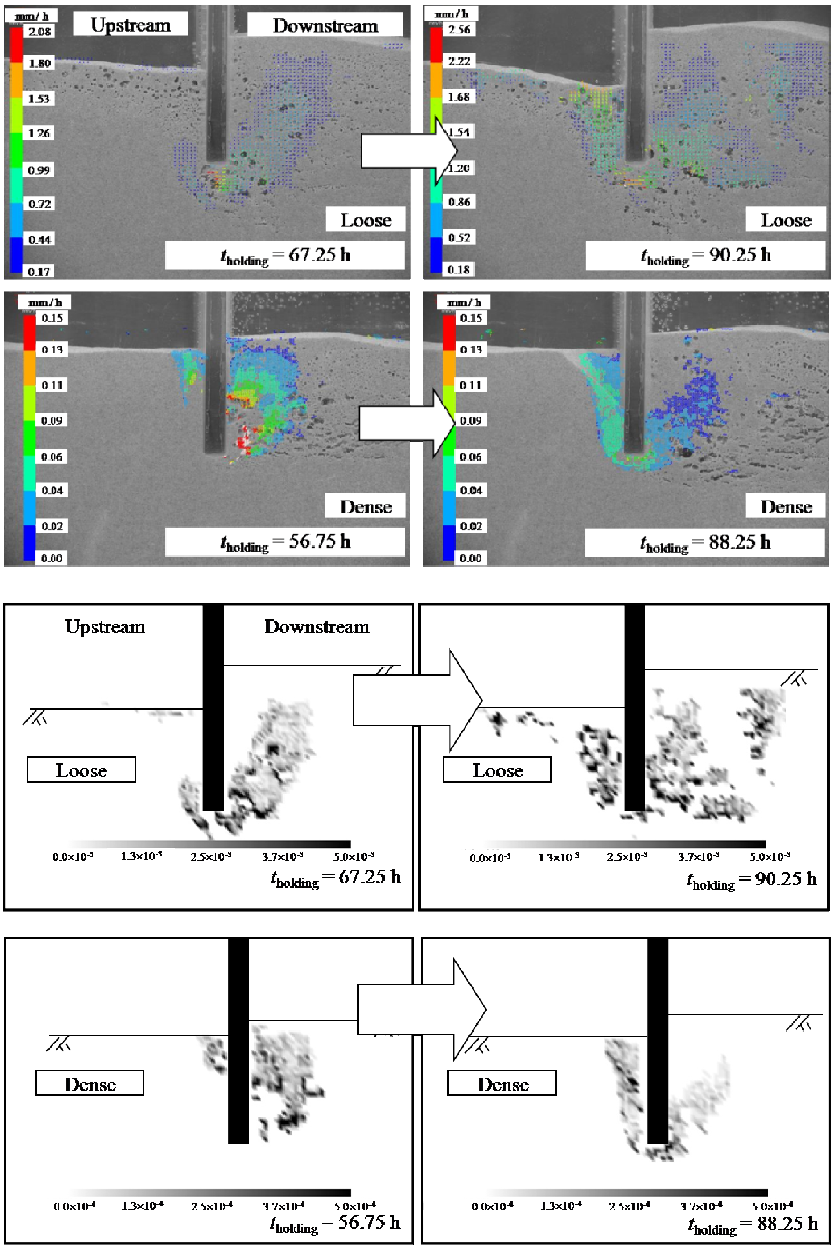

Fig.3.4.1 Result of PIV analysis (upper side) and the distribution of the maximum shear strain rate (lower side) (Loose: Case L-3 Dense: Case D-1)

3.5 Summary

Seepage failure phenomenon in macro scale is summarized as follows:

(1) Water-level differences were achieved before a clear displacement occurred on the ground surface on the upstream side in normal seepage failure. These differences were 80%–90% of the critical water-level differences

(2) Unlike the seepage failure phenomenon in ground without air bubbles, when the ground contained air bubbles, the ground surface deformed and repeatedly subsided and uplifted. Finally, failure would occur after a long period of time even though the water-level difference was maintained at a stable value.

(3) The ground subsidence in this case was localized and was larger in dense ground then in loose ground.

(4) In the loading test, settlement increased as the number of air bubbles increased, and the final settlement of the ground with more air bubbles was 5 times that of the ground without air bubbles.

(5) The effect of density was larger than the effect of the degree of supersaturation on air bubble generation. And air bubble generation was affected not only by the degree of pore water supersaturation but also by contact between water and soil particles during seepage and by a slight pressure fluctuation.

(6) The shear strain rate was distributed widely and inhomogeneously, centering on the sheet pile. The existence of air bubbles caused complicated deformations in the ground.

Chapter 4

Micro Scale Seepage Failure Phenomenon

4.1 Changes in the Size and Shape of Air Bubbles

In Fig. 3.3.3, a change in the speed of air bubble development in supersaturated conditions was identified. Figure 4.1.1 shows images of bubble development of many air bubbles with different sizes and shapes. It can be easily imagined that the impact of larger air bubbles on the ground is greater than smaller bubbles. In addition, a change in the shape of air bubbles means that they shear the ground around them to cause a local failure, resulting in a serious influence on their dynamics. Therefore, the size and shape of air bubbles are worth investigating.

Figures 4.1.2 and 4.1.3 show the distribution of bubble areas (Fig. 4.1.2), the distribution with the number of bubble shapes (aspect ratios: Fig. 4.1.3(A1, A2)), and the distribution of the area fraction of air bubbles with different shapes (Fig. 4.1.3(B1, B2)), respectively, in case D-1. As shown in Fig. 4.1.2, approximately 80% of the air bubbles were fine, with areas of 0.1 mm^2 or smaller in the early stage (10 h). The distribution shifted to the right as time passed, and the percentage of fine bubbles decreased and that of medium-sized bubbles (larger than 0.1 mm^2) rapidly increased. From 13.5 h to 16 h, when the slope of the curve showing the quantity of air bubbles changed, the number of bubbles with areas of 0.3 mm^2 or smaller decreased compared with the previous 3.5 h period (from 10 h to 13.5 h), and the number of air bubbles with areas 0.3 mm^2 or larger rapidly increased. From 16 h to 17.5 h, the percentage of these larger air bubbles increased further. Generation of fine air bubbles and their coalescence were the main cause of the increased quantity of air bubbles in the early stage. As time progressed, further development of air bubbles from coalescence became the main cause of the increase in the quantity of air bubbles.

After 33 h, just before the first escape of air bubbles from the ground, the percentage of large air bubbles became highest, and some of the air bubble diameters exceeded 2 mm when the air bubble areas changed into a cubic shape. After the first escape (33.25 h), the number of medium-sized air bubbles with areas of 0.5 mm^2 or larger especially decreased; in other words, the air bubbles that developed and became large blew out from the ground. Bubbles with areas of 0.5 mm^2 or larger were the major type present just prior to seepage failure.

Next, the shapes of air bubbles were investigated (Figs. 4.1.3 and 4.1.4). Bubbles with aspect ratios below 1 have flat shapes (developed in the horizontal direction, perpendicular to the seepage flow). An aspect ratio of 1 indicates a circular shape. An aspect ratio above 1 indicates a slender shape (developed in the vertical direction parallel to the seepage flow). The seepage flow was directed upward through the ground on the downstream side. In Fig. 4.1.3(A1, A2), since air bubbles with flatness values of 1 or larger comprised 65% of the total air bubbles just after air bubbles were generated, air bubbles tended to develop parallel to the seepage flow. As time proceeded, the percentage of air bubbles with aspect ratios of 1 or larger decreased and those with aspect ratios of 1 or smaller increased. Because the percentage of air bubbles with aspect ratios of 2 or larger decreased and those with aspect ratios between

1 and 2 increased, the shapes of air bubbles gradually became closer to globular with time. In the period between 33 h and before the first blow out, the percentages of the above two shapes were similar. Under magnification, air bubbles with flatness values below 0.3 (developed in the horizontal direction perpendicular to the seepage flow and having extremely oblong shapes) existed just before escape (33 h). Since these air bubbles disappeared after air escaped (33.25 h), air bubbles were apparently forcefully compressed by the seepage flow or the movement of soil particles that accompanied the seepage flow. On the other hand, although the percentage of air bubbles with aspect ratios between 0.3 and 1 increased with time from the beginning, this group tended to decrease just before the escape (33 h). Therefore, these air bubbles were believed to unite to form air bubbles with extremely oblong shapes.

When the change of air bubble shapes was investigated relative to the area fraction in Fig. 4.1.3(B1, B2), the air bubble's aspect ratios in the early stage (10 h) was opposite that of the blow out stage (33 h). In the image in Fig. 4.1.1 showing the early stage of air bubble generation, all of the air bubbles at the lower end of the area where air bubbles were generated developed in upward and laterally, while lower parts of the air bubbles were fixed at the lower end of the generation area. A possible reason for this was the expansion of the air bubble caused by buoyancy. In the image taken after 25 h, when the air bubbles have expanded to some degree, adjacent expanding air bubbles united to form many air bubbles with overall oblong shapes.

In order to investigate the main location of air bubble development, the ground at the downstream side of the sheet pile was divided into the upper layer, middle layer, and lower layer, and a temporal change in the air bubble diameter distribution was investigated in each layer (Fig. 4.1.4(A)). In the period between the initiation of the test and approximately 15 h after the initiation, no significant change in the air bubble diameter distribution was observed in the vertical direction, and small air bubbles with areas of 0.2 mm^2 or smaller were the majority. After 20 h, large air bubbles started to appear in the middle layer, slightly large air bubbles appeared in the middle layer, and the ratio of small air bubbles was larger in the upper layer than the other layers. The possible reason for this is that since the overburden pressure in the upper layer is small, air bubbles are blown out from the ground due to their buoyancy before they become larger. Although air bubbles can become slightly larger in the lower layer due to its large overburden pressure, the slightly larger air bubbles are carried to the middle layer due to the seepage force. In the middle layer, since the overburden pressure is significant, the slightly larger air bubbles carried from the lower layer are clogged and gathered between soil particles, thus developing into large air bubbles. Thus, the air bubble size is determined according to the depth, and the location where air bubbles are easily gathered depends on the balance between the overburden pressure, buoyancy, and seepage force.

Next, a change in the air bubble size before and after the first blow out of air bubbles (after 33 and 33.25 h) was investigated (Fig. 4.1.4(B)). Consequently, it was blown out that the ratio of large air bubbles with areas of 2–4 mm^2 was particularly smaller after the blow out than before, and the overall air bubble size was smaller after the release than before in the lower layer. The reason for this is probably that air bubbles in the lower layer united with each other to form large air bubbles, and the formed air bubbles blew out of the ground. During this process, the ground was disturbed and degraded. Although the regions of the development and blow out of air bubbles differ according to the penetration depth of the sheet pile, assumption or specification of these regions is very important for proposing countermeasures against seepage failure, taking air bubbles into consideration.

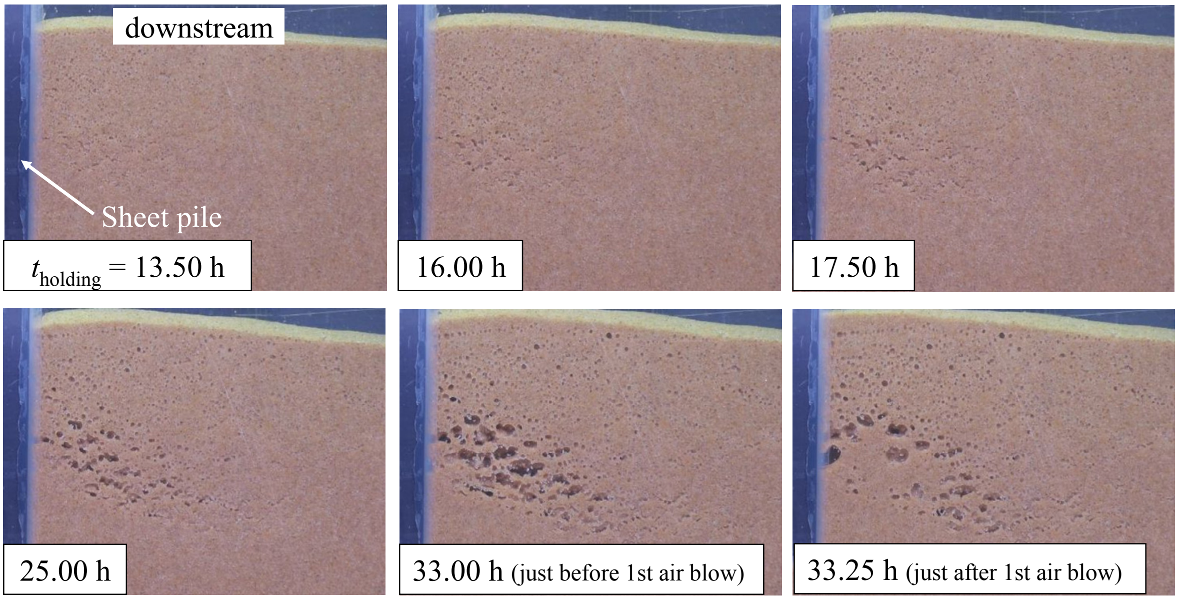

Fig.4.1.1 Appearance of bubble development downstream from the sheet pile: Case D-1

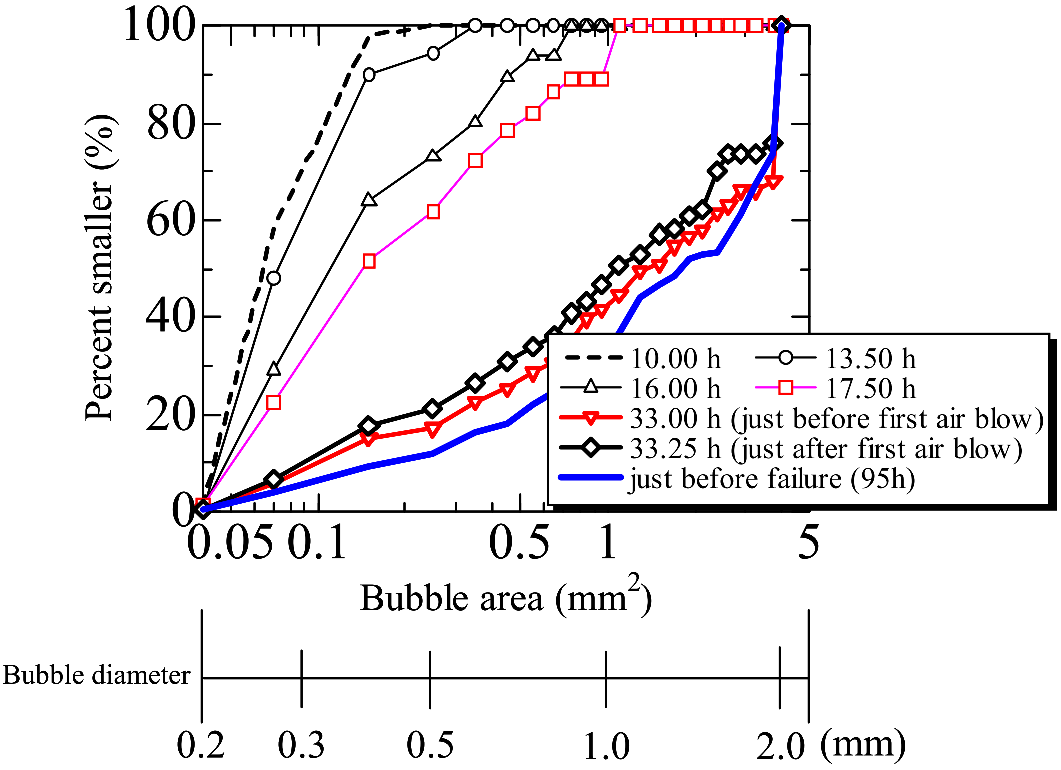

Fig.4.1.2 Bubble area distribution: Case D-1

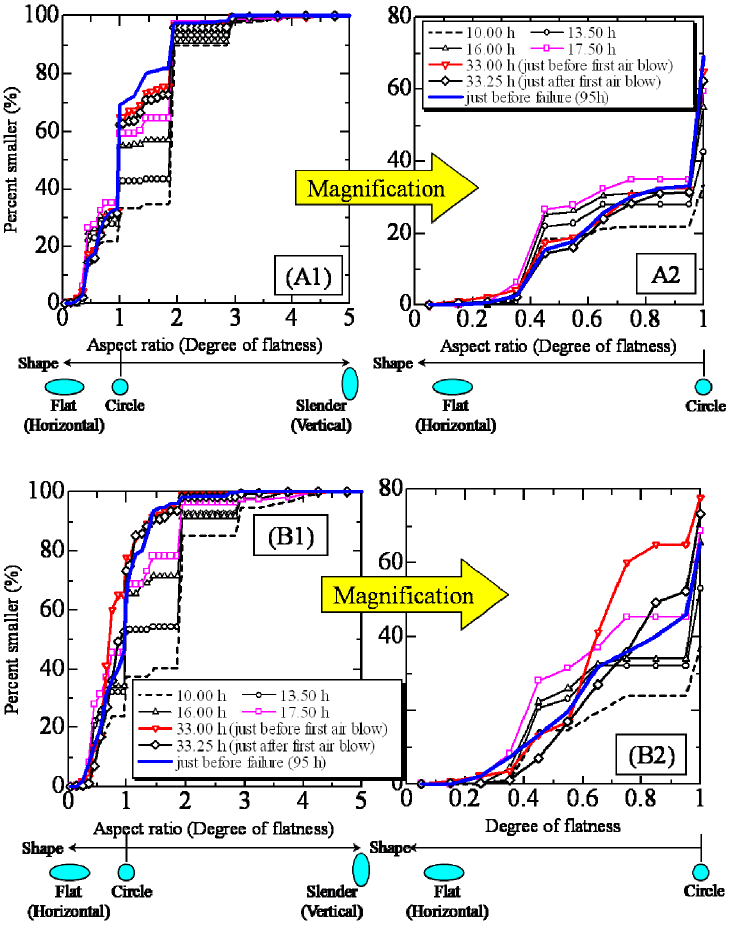

Fig.4.1.3 Bubble shape distribution with the number of air bubbles (A1, A2) and bubble shape distribution with the area fraction of air bubbles (B1, B2) in the case of D-1: (A1, B1) original (A2,B2) magnified view

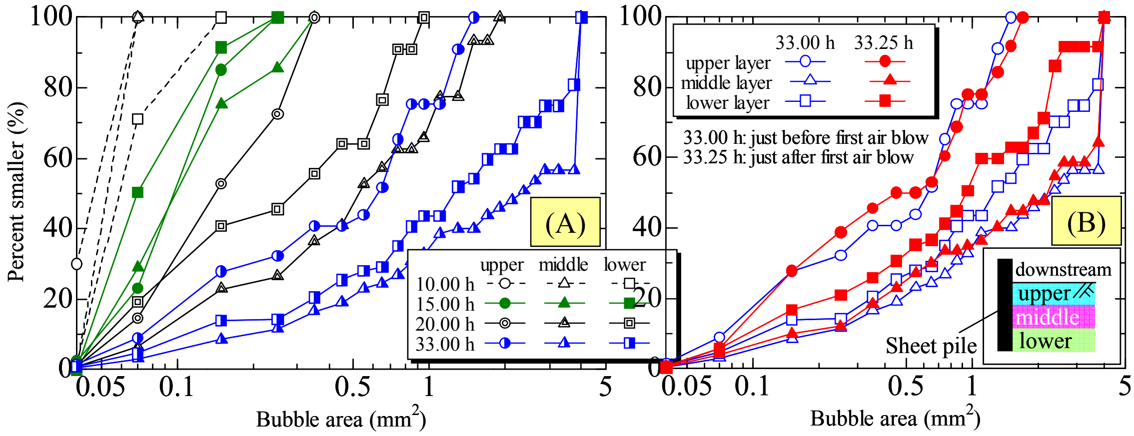

Fig.4.1.4 Bubble shape distribution by depth: (A) expansion of bubbles (B) before and after the size of bubbles

4.2 Transformation of both Bubble and Surrounding Soil of Bubble

Left side in Fig. 4.2.1 shows the PIV analytical result for the same time as the elapsed time (f’) in Fig. 3.3.4 just before the 5th air emission (70.25 h) in D-1. Focused air bubble was evident in the left side of Fig. 4.2.1, and ground movements around each air bubble were investigated from its generation to its emission from the ground. Right side in Fig. 4.2.1 shows the temporal change in soil particle velocity at the top and bottom of air bubbles. In the period between the appearance of the air bubble and 10 h after its appearance (t_{holding} = 45 h), soil particles at the top and bottom of the air bubble had clearly moved. This meant the air bubble was moving upward and expanding (parallel to the seepage flow). Figure 4.2.2(a) shows the PIV analytical result for air bubbles in the early development stage (37 h) including a magnified view. Here, signs (a-c) in Fig. 4.2.2 correspond to elapsed times (a-c) in right side of Fig. 4.2.1. The higher magnification shows that the soil particle velocity was nonzero only at the tops of air bubbles. At 37.25 h, the circled air bubble had expanded slightly. This was possibly due to the buoyancy of the air bubble and air bubble development associated with the elution of dissolved gas from pore water.

Figure 4.2.2(b) shows the PIV analytical result for air bubbles at 50.75 h and includes a magnified view. At higher magnification, it is clear that air bubbles moved slightly to the right because of seepage flow; air bubbles moved and expanded in it as time progressed, as shown in the right side of Fig.4.2.1.

Figure 4.2.2(c) shows the PIV analytical result for air bubbles at 67.5 h and includes a magnified view. In ground containing air bubbles, the vector distribution shown in the left side of Fig. 4.2.1 is typical. However, when an air bubble moved and expanded, the velocity at the bottom of the air bubble commonly increased and the air bubble was compressed by soil particles, as shown in Fig. 4.2.2(c). When the internal pressure of the air bubble increased from this process, the air bubble moved upward and expanded. Air bubbles move upward while repeatedly expanding and being compressed via this mechanism, and they finally escape from the ground.

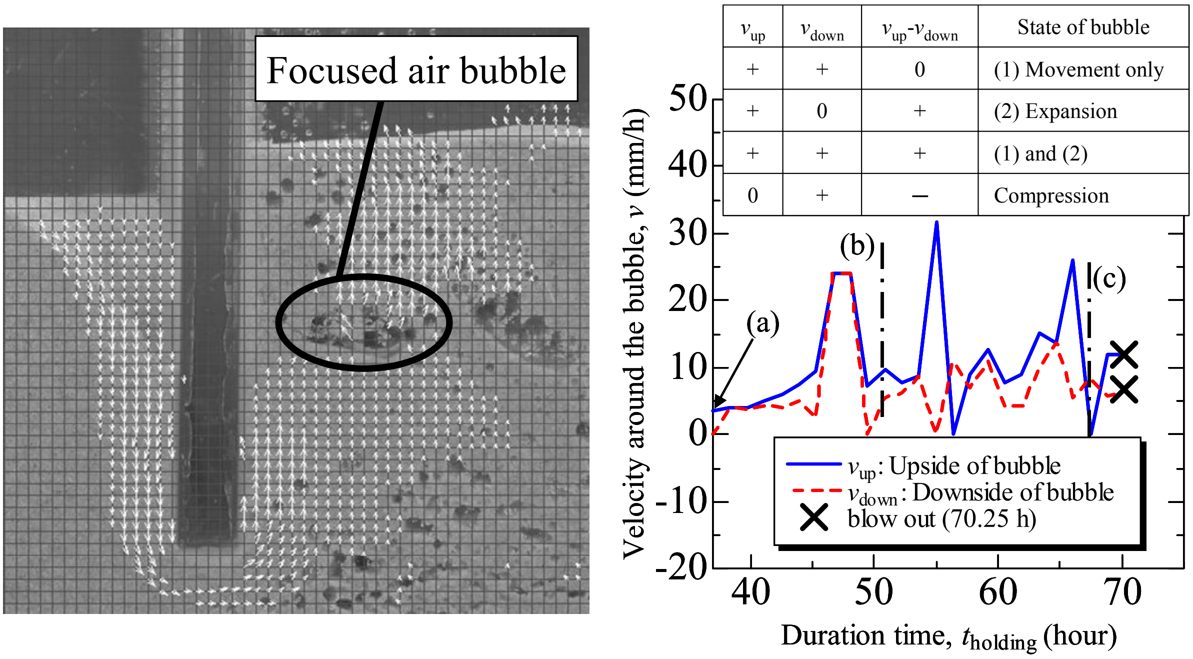

v_{up}	v_{down}	v_{up}-v_{down}	State of bubble
+	+	0	(1) Movement only
+	0	+	(2) Expansion
+	+	+	(1) and (2)
0	+	–	Compression

Fig.4.2.1 A result showing the downstream part of sheet pile (left side) and the change in the soil particle velocity at the top and bottom of the bubble (right side)

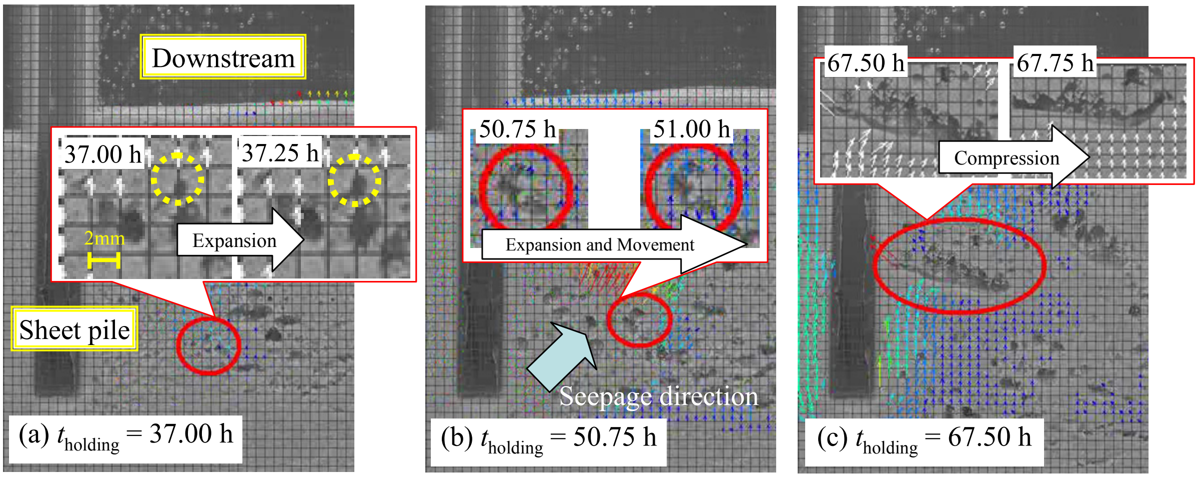

Fig.4.2.2 Expansion and deformation of a bubble: (a) Expansion (b) Expansion and Movement (c) Compression

4.3 Upstream Ground Deformation due to Air Bubble Escape

As shown in Figs. 3.1.3(A) and 3.3.4, deformation rapidly progressed downstream and subsidence slowly occurred upstream in the holding test in which the water-level difference was maintained at a fixed value. Loose ground expanded and then subsided upstream because of air bubble generation at the upstream side. To explain the reason for ground subsidence upstream after ground deformation downstream, the PIV analytical result for the large air bubble escape from the ground (the elapsed time of Fig. 3.3.4(c')–(e')), and the maximum shear strain rate distribution were investigated (Fig. 4.3.1).

The red line in the left side of Fig. 4.3.1 indicates the tip of the velocity vector on the upstream side. As shown in this figure, the deformation propagated upstream, rounding below the sheet pile and accompanying the air bubble escape from the ground downstream, and then the ground upstream started to subside (the elapsed time of Fig. 3.3.4(e')). As shown by the ground surface displacement, at about 40 h in D-1 in Fig. 3.3.4, when air bubbles initially escaped from the ground downstream, the ground upstream did not subside. The likely reason for this is that at the time of the air bubble escape on the downstream side, the space generated by the escape was filled by the falling elevated ground (the elapsed time of Fig. 3.3.4(d')). This assumption was supported by the velocity vector distribution obtained from the PIV analysis. However, when the deformation propagated to the ground upstream and ground upstream started to subside, the subsidence on the downstream side was not as active as that on the upstream side (elapsed times of Fig. 3.3.4(g) and (g')). This tendency was particularly notable in dense ground. The velocity vector distribution obtained from the image analysis showed that the ground above the air bubbles had not subsided significantly at the time of the air escape, and the ground from below the air bubbles to the upstream side through the sheet pile moved downstream, probably because of seepage flow.

As mentioned above, seepage failure does not occur until the ground upstream starts to subside, regardless of the existence of air bubbles. The dynamics (generation, movement, development, and blow out) of air bubbles accumulating in the whole area downstream of the sheet pile initiate the subsidence.

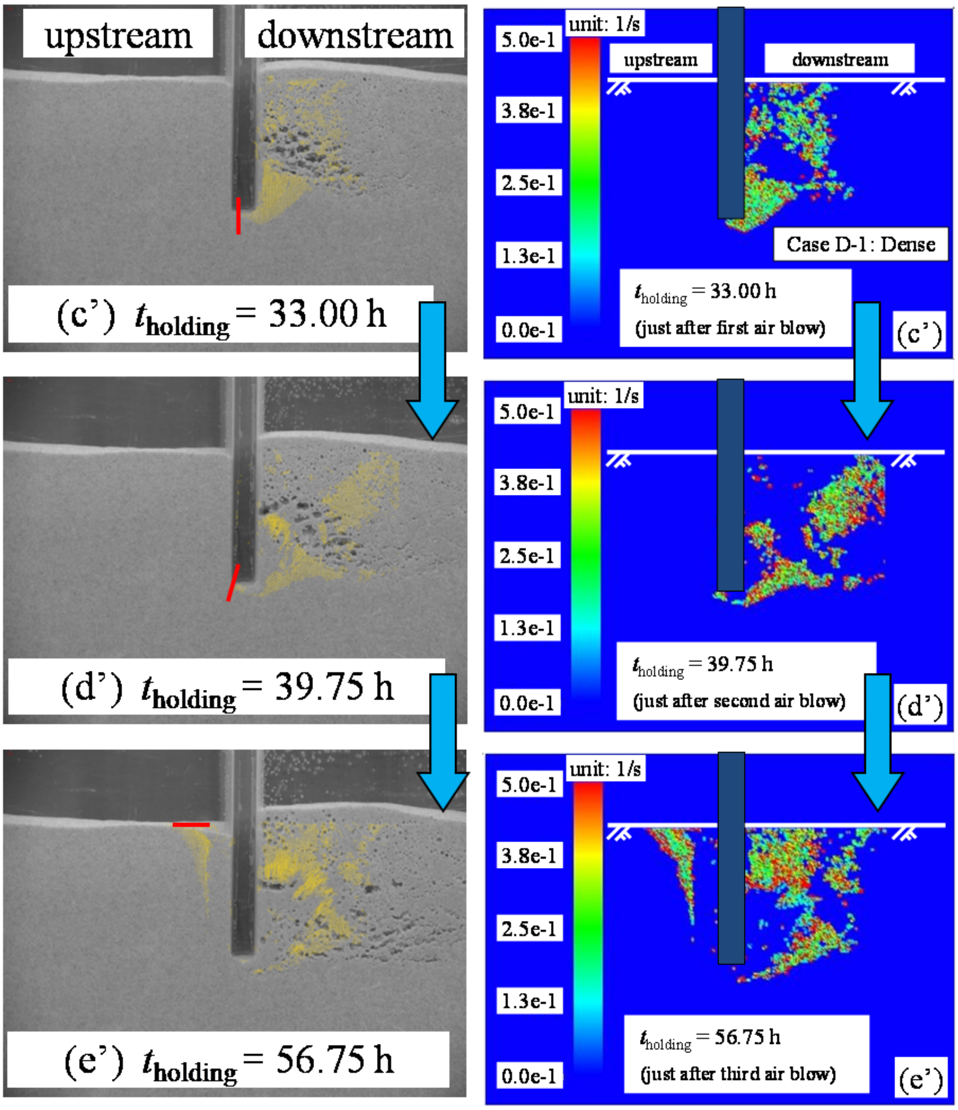

Fig.4.3.1 Spread of upstream destruction in dense ground: Case D-2 (left side: PIV analysis, right side: Maximum shear strain rate distribution)

4.4 Results of Water Pressure Measurement

Figure 4.4.1 shows an example of the tensiometer results (upper side: monotonic raising test, lower side: holding test). In the monotonic raising test, the excess pore pressure ratio increased with the water level upstream, and finally seepage failure occurred. In the holding test, the excess pore pressure ratio also increased, although the water-level difference was maintained at a fixed value. Between 10 and 15 h after the test beginning, the excess pore pressure ratio decreased and air bubble releases around the sheet pile were observed. The reason for this was likely due to the change in the dilatancy of the ground, accompanied by the movement of air bubbles.

Figure 4.4.2 shows the excess pore pressure ratio measured using the tensiometer in loose ground during the holding test, which was the different from the case in the lower side of Fig. 4.4.1. The excess pore pressure ratio gradually increased during the test, and at time (A), the excess pore pressure ratio rapidly increased. At that time, a large air bubble (bubble diameter is about 3 mm) escaped around the tensiometer, as shown in the photograph in Fig. 4.4.2. This rapid increase in the excess pore pressure ratio was also measured at about 186 and 210 h. Therefore, complicated changes in the momentary variations of pressure in the ground caused by air bubbles were quantitatively confirmed.

Next, we paid attention to the value of excess pore water pressure ratio. The excess pore pressure ratio in monotonic raising test indicates between 0.6 and 0.7, as shown in the upper side of Fig. 4.4.1, where ΔH is 120 mm. Otherwise, the excess pore water pressure ratio shows lower value than 0.6 before air bubble released from the ground surface in Fig. 4.4.2. However, the excess pore water pressure ratio increases rapidly up to 0.65 due to blow out of air bubble at the point of (A) in Fig. 4.4.2. This means that the compressibility of air bubble decreases excess pore water pressure around the air bubble. The blow out of air bubble induces increment of excess pore water pressure.

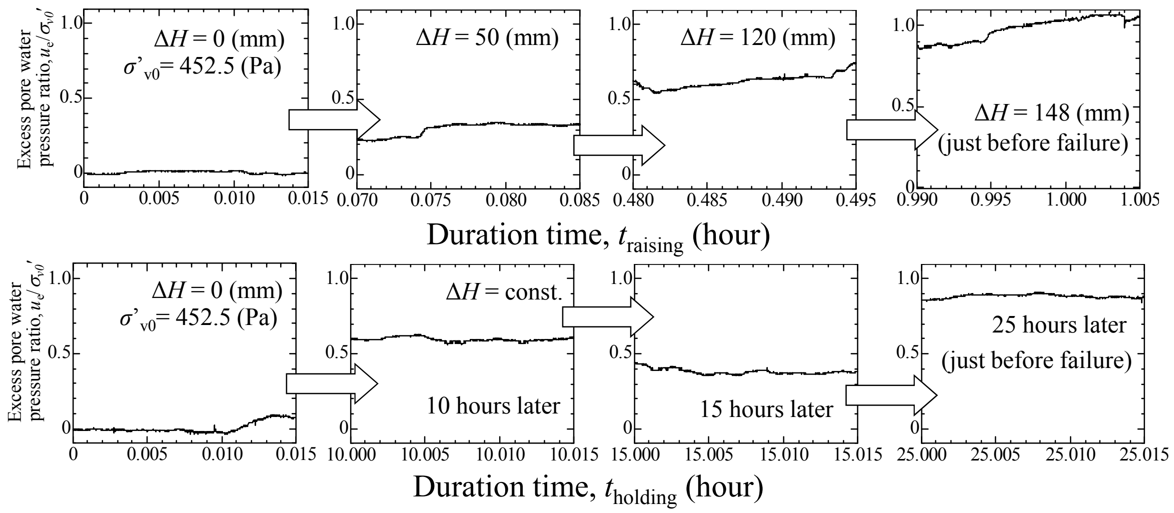

Fig.4.4.1 Changes in the excess pore water pressure ratio(upper side: monotonic raising test, lower side: holding test)

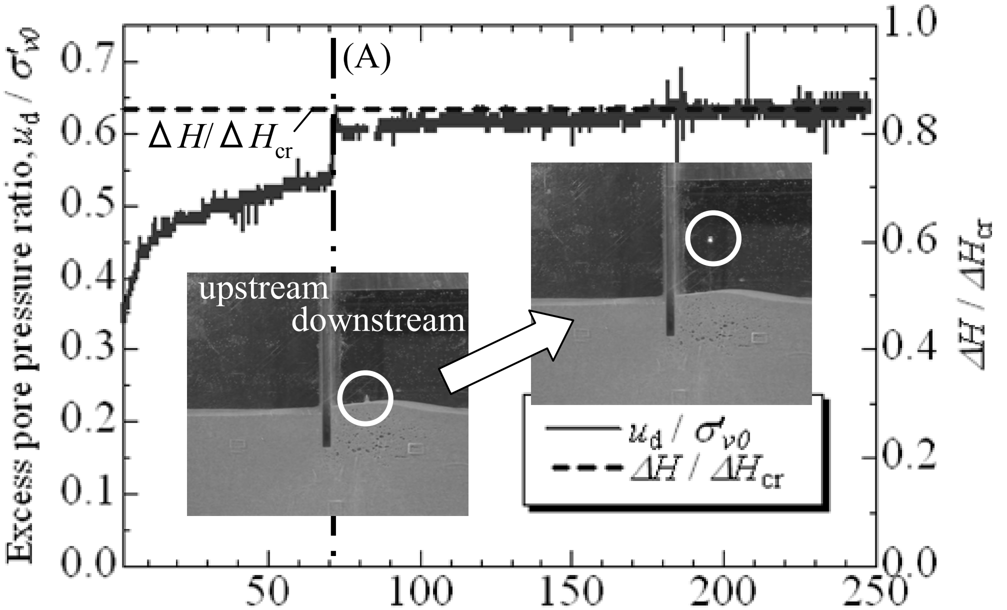

Fig.4.4.2 Increase in the excess pore water pressure ratio with air blow: holding test, Loose, ΔH=120mm, t_{holding}=72.68h

4.5 Critical Hydraulic Gradient and Hydraulic Gradient

Figure 4.5.1 shows temporal changes in the void ratio and the critical hydraulic gradient i_{cr} obtained using Eq. (2.5.1) for Cases L-3 and D-1 at the downstream side. Although the void ratio changed with the quantity of air bubbles, it tended to increase on the whole. The critical hydraulic gradient tended to decrease with the increase in the void ratio. When seepage failure occurred, the void ratio and the critical hydraulic gradient were higher and lower than those of the initial stage by approximately 10%.

The right side of Fig. 4.5.2 shows the temporal changes in the seepage distance L and the permeable water volume Q in case D-2. To simplify the calculations in this study, seepage in the sheet-pile penetration area was assumed to be parallel to the sheet-pile, and seepage below the sheet-pile tip was assumed to occur in a semicircle with the radius W: the distance between the sheet-pile and the seepage distance line (left side of Fig. 4.5.2). In addition, deformation of the ground is very local in the seepage phenomena. And the amount of surface displacement at $W = D/2$ upstream was equal to the average value of all ground surface displacements. So we use $D/2$ as the value of W. Here, the permeable water volume rapidly increased after about 65 h. Although the seepage distance increased from the test beginning to 65 h, it tended to decrease after 65 h. Since the water-level difference was maintained at a fixed value in this test, no large difference should be generally observed. Therefore, the increase in permeable water volume was likely due to the local decrease in seepage distance. In loose ground, the whole area around the sheet pile was deformed. In dense ground, as shown in Fig. 3.1.2(C’), the seepage distance greatly decreased at a specific site near the sheet pile. Since an appropriate correspondence was observed between the permeable water volume and the seepage distance, as shown in the right side of Fig. 4.5.2, the permeable water volume appeared to be greatly affected by the decrease in the seepage distance.

Based on the seepage distance and the water-level difference, the hydraulic gradients in cases L-3 and D-1 were then calculated using Eq. (2.5.2) (Fig. 4.5.3). As shown in this figure, the hydraulic gradient initially decreased in both loose and dense ground. The reason for this could have been that the ground downstream expanded upward because of air bubble generation, and consequently, the seepage distance increased. Following this, the hydraulic gradient increased. In dense ground, since the seepage force just before seepage failure was larger than at the beginning, the presence of air bubbles had a strong negative effect on the ground. As seepage failure of the ground containing air bubbles progressed, the seepage distance changed and was accompanied by the generation and development of air bubbles, and consequently, the seepage force changed.

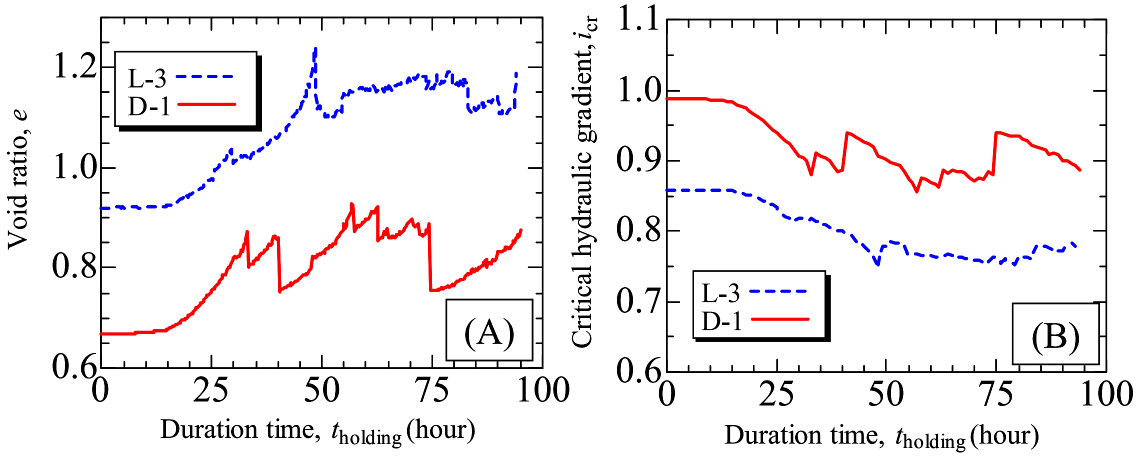

Fig.4.5.1 Changes in void ratio and critical hydraulic gradient dowunstream of the sheet pile: (A) void ratio (B) critical hydraulic gradient

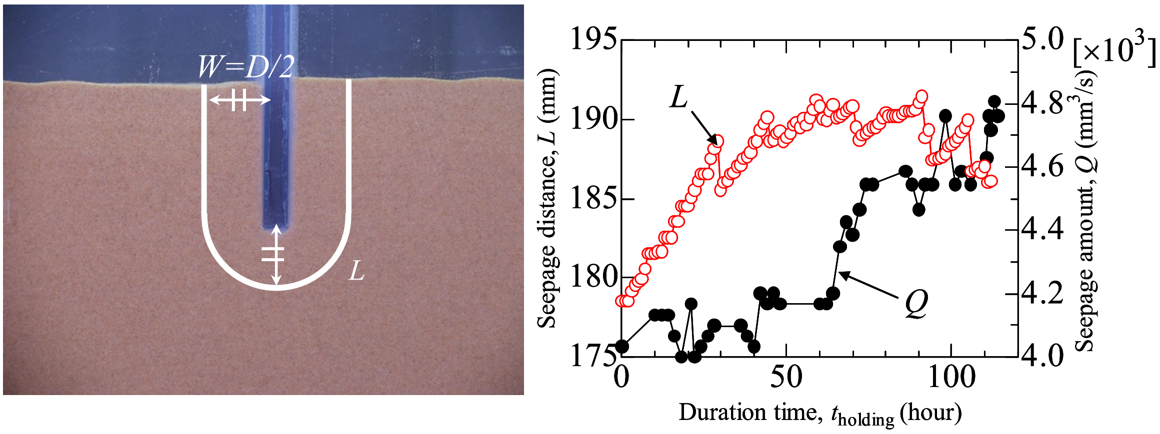

Fig.4.5.2 Definition of seepage distance (left side) and seepage amount (right side): Case D-2

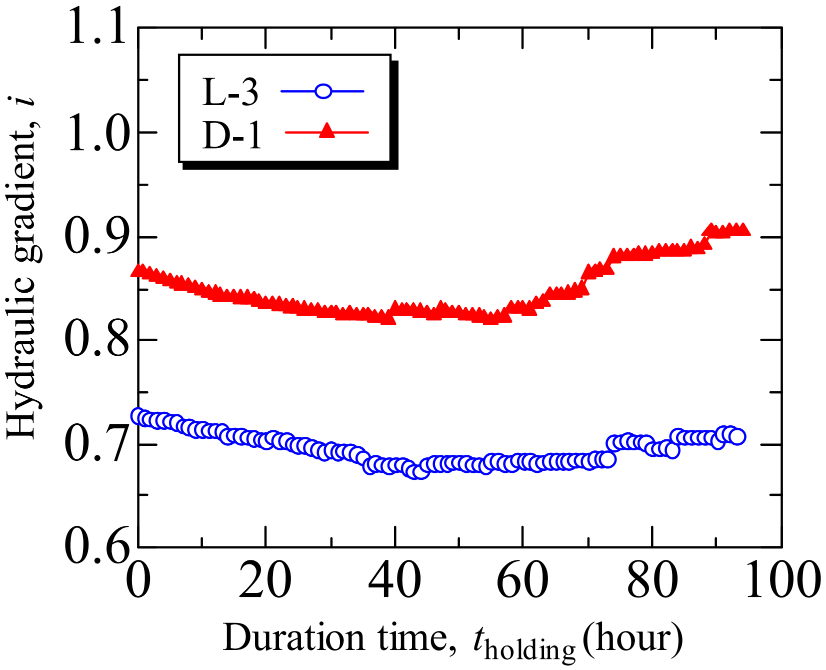

Fig.4.5.3 Changes in the hydraulic gradient at each density

4.6 Summary

Maicroscale seepage failure phenomenon is summarized as follows:

(1) It can be easily imagined that the impact of larger air bubbles on the ground is greater than smaller bubbles. In addition, a change in the shape of air bubbles means that they shear the ground around them to cause a local failure, resulting in a serious influence on their dynamics. Therefore, the size and shape of air bubbles are worth investigating. We can examin to both bubble shapes and sizes by using proposed image analysis method.

(2) In order to investigate the main location of air bubble development, the ground at the downstream side of the sheet pile was divided into the upper layer, middle layer, and lower layer, and a temporal change in the air bubble diameter distribution was investigated in each layer. Then the air bubble size is determined according to the depth, and the location where air bubbles are easily gathered depends on the balance between the overburden pressure, buoyancy, and seepage force.

(3) Although the regions of the development and blow out of air bubbles differ according to the penetration depth of the sheet pile, assumption or specification of these regions is very important for proposing countermeasures against seepage failure, taking air bubbles into consideration.

(4) Seepage failure does not occur until the ground upstream starts to subside, regardless of the existence of air bubbles. The dynamics (generation, movement, development, and blow out) of air bubbles accumulating in the whole area downstream of the sheet pile initiate the subsidence

(5) The compressibility of air bubble decreases excess pore water pressure around the air bubble. The blow out of air bubble induces increment of excess pore water pressure.

(6) When seepage failure occurred, the void ratio and the critical hydraulic gradient were higher and lower than those of the initial stage by approximately 10%.

(7) The hydraulic gradient initially decreased in both loose and dense ground. The reason for this could have been that the ground downstream expanded upward because of air bubble generation, and consequently, the seepage distance increased. Following this, the hydraulic gradient increased.

Chapter 5

Air Bubble Lifetimes on Multiple Scales

The effect of air bubbles on the ground has been described using the observations and image analyses in this paper. However, air bubble generation and development have not been sufficiently explained. This mechanism must be verified on multiple scales. Therefore, by integrating chemical and geotechnical knowledge and information, air bubble generation and development in soil particles were dynamically investigated.

5.1 Air Bubble Generation on the Soil Particle Surface (Micro Level)

For an air bubble to be generated in liquid, an “air bubble nucleus” is required (Techno System Co. Ltd., 2005; Leighton, 1994). An infinite number of air bubble nuclei from nanometers to micrometers in size exist in normal liquid. An example of a typical structure providing such a nucleus is a notch (gas pocket) on a hydrophobic solid surface. Within the notch, an air bubble nucleus can exist stably because of the balance between pressure and surface tension (Young-Laplace equation) as shown in Eq. (5.1.1). Stage 1 in Fig. 5.1.1 demonstrates this process, described by the following equation:

$$u_a - u_w = \frac{2S_t}{R} \qquad (5.1.1)$$

where u_a expresses the internal pressure of an air bubble, u_w expresses the pore water pressure on the air bubble surface, S_t is the surface tension, and R is the curvature radius. Since an infinite number of fine concave-convex locations exist on a soil particle's surface, these places can act as notches that hold air bubble nuclei. Therefore, the initial conditions required for air bubble generation were considered to be sufficiently satisfied in this study.

One of the most important considerations is the existence of the transitional region of dissolved gas and elution gas (Wheeler, 1988). This area surrounds each bubble, and non-dissolved gas in the region (non-dissolved gas pressure: u_g) can move in between the bubble and the area according to Henry's law as follows:

$$u_a = \alpha u_g \qquad (5.1.2)$$

where α expresses the Henry constant. Since the non-dissolved gas pressure u_g in supersaturated pore water is high, gas is captured by a nucleus on the soil particle surface and fills the pocket. In addition, the nucleus is stable in the gas pocket using the Eq. (5.1.1): ($u_a < u_w$). Supersaturated pore water, including more non-dissolved gas, causes the non-condensing gas layer around these bubbles to expand, and it is incorporated into the air bubble to satisfy Henry's law, and consequently, air bubble development is promoted further. For these reasons, fine air bubbles are believed to develop particularly around the sheet pile, where a large amount of supersaturated pore water is supplied. But the development speed of a bubble using this mechanism is very slow, as shown in Fig. 3.3.3 (before 10 h).

After developing to a certain degree, an air bubble escapes from a concave-convex place on the surface of soil particles and moves forward among the soil particles. When the air bubble reaches the downstream side, it expands because of the newly supplied pore water and a decrease in static water pressure. When the air bubble exceeds the pore diameter, it ceases moving (Stage 2 in Fig. 5.1.1). This type of air bubble continues to develop not only because of supersaturated water, but also when it unites with other fine air bubbles rising from the backside (lower part) of the dam with the seepage water. At this point, since the air bubble does not have an internal pressure sufficient to push soil particles away, these slender air bubbles consequently lie along the seepage flow. At this point, these air bubbles are not united because of their small surface tensions (by which air bubbles pull on each other) associated with their small sizes. (See Young-Laplace equation of Eq. (5.1.1).) However, the surface tension effect soon causes these bubbles to unite and become globular. Thus, the shape of air bubbles changes from slender to globular as time progresses, as shown in Fig. 4.1.3.

Moreover, another mechanism could be used. Using Eq. (5.1.1), large bubbles have a lower pressure than small ones under constant water pressure (u_w). Using Eqs. (5.1.1) and (5.1.2), large bubbles also have small non-dissolved gas pressure (u_g). In other words, the non-dissolved gas pressure of a small bubble is thicker than the pressure of a large one. Since gas density becomes homogeneous, gas transfer occurs with the bubble movement from small bubbles to large ones. Thus, large bubbles are grown by collecting many small bubbles. In this process, a bubble doesn't need a long time to develop, as in the "transport of the non-dissolved gas" process. So when bubbles cease to move by the void diameter, the mechanism of bubble development is changed from a slow type to a rapid type (Fig.3.3.3: changing in the slope of the curve).

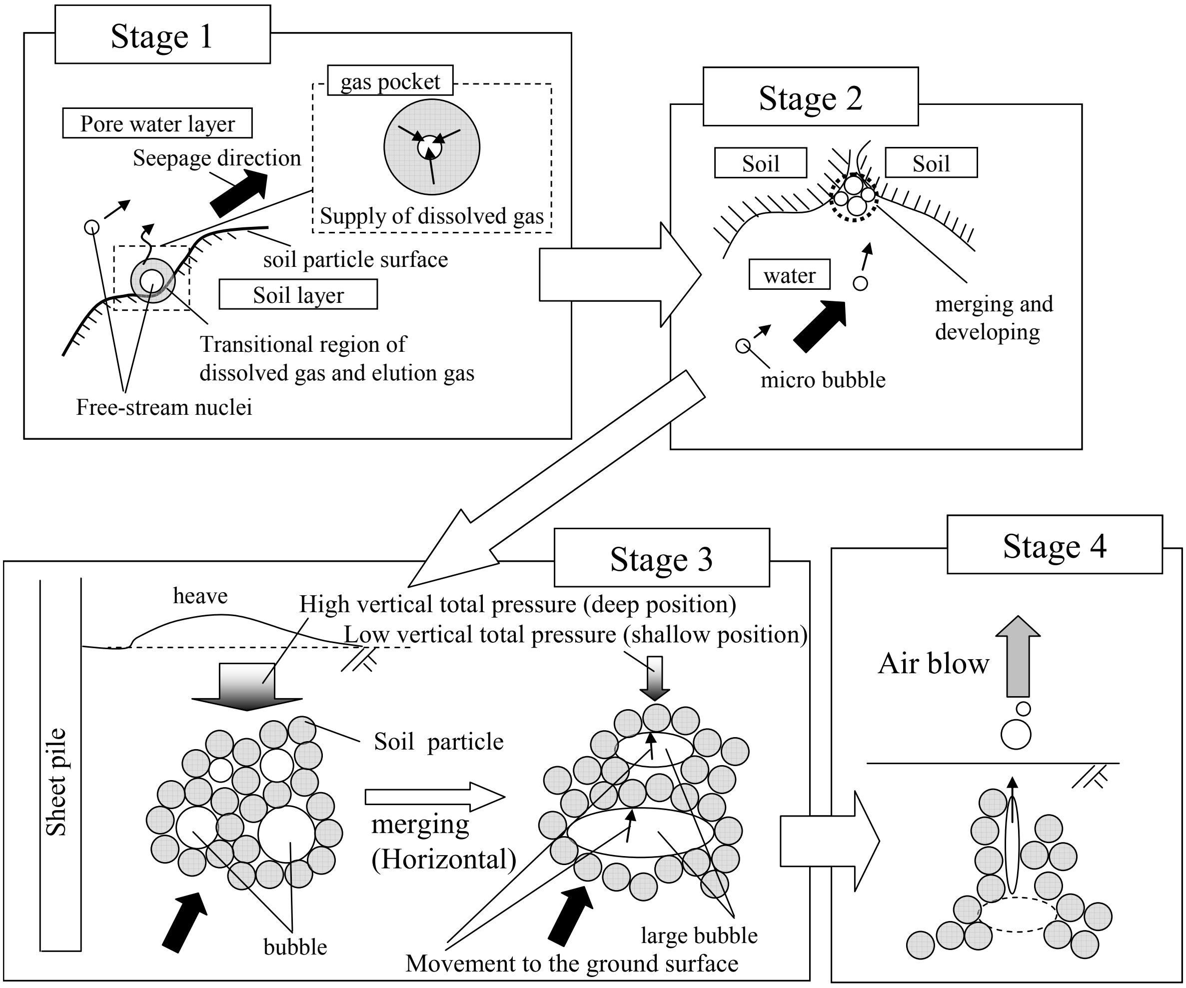

Fig.5.1.1 Bubble development process by stage

5.2 Development of Air Bubbles (Macro Level)

A micro side air bubble develops and expands farther due to the above-mentioned mechanism. Air bubbles uniformly develop in the ground near the sheet pile at the downstream side, and developed air bubbles are united. As shown in Fig. 4.1.4, air bubbles mainly developed in the middle layer at the downstream side of the sheet pile. The reason for this is considered to be that since the overburden pressure in the upper layer is small, air bubbles are released from the ground before they become larger. In the lower layer, since air bubbles do not sufficiently grow, and since gaps between soil particles are larger than air bubbles, air bubbles pass through the gaps. As shown in Fig. 4.1.1 (25 and 33 h), adjacent air bubbles are united to become an air bubble with a flat shape. The reason for this is possibly that air bubbles basically move in the upward direction due to the balance between the overburden pressure above the air bubbles, their buoyancy, and the seepage force from below. However, before growing to a certain size, air bubbles cannot move in the upward direction due to their small buoyancy. Consequently, air bubbles continuously grow at the same position and adjacent air bubbles are united (Stage 3 in Fig. 5.1.1).

Horizontally anisotropic air bubbles increase in volume and have decreased internal pressures. The air bubble becomes flatter from the vertical earth pressure and the seepage force from below, and consequently, its internal pressure increases. In ground where air bubbles are generated, the void ratio increases, and air bubbles closer to the ground surface escape more readily. Since the hydraulic gradient increases as the seepage distance decreases, air bubbles escape more easily, so that escape becomes easier with time. When the buoyancy of an air bubble exceeds the vertical earth pressure above it, the air bubble becomes slender and escapes the ground, strongly shearing the soil above it (Stage 4 in Fig. 5.1.1).

Air bubbles are believed to initiate, develop, and escape from the ground by this mechanism, which is summarized in Fig. 5.1.2. Preventing air bubble formation is likely to be very difficult in natural waters unless pore water exists in an unusual degassed condition. In other words, few measures in nature will inhibit air bubble generation from pore water.

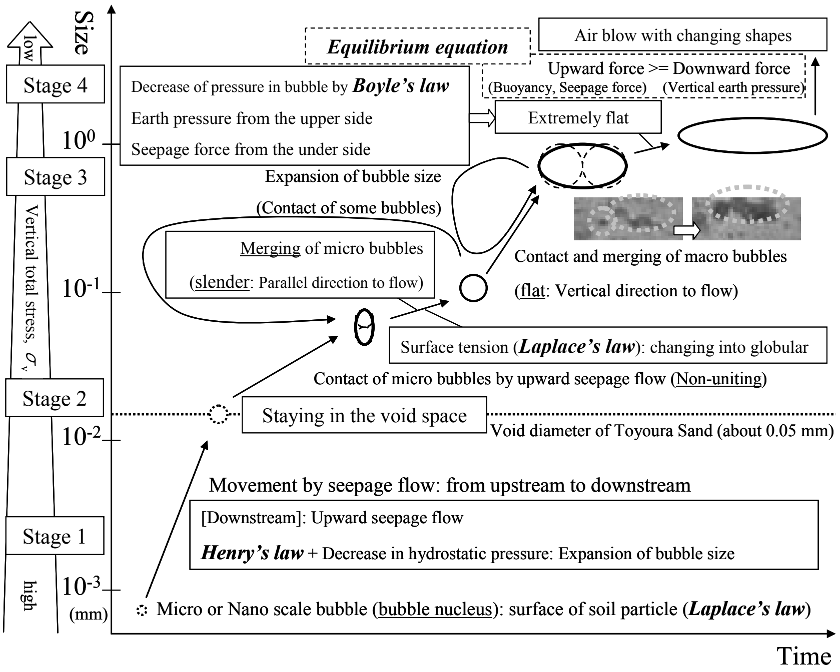

Fig.5.2.1 Evolution and disappearance of bubble (Lifespan of a bubble)

5.3 Summary

In this chapter, we explained the lifespan of a bubble. Air bubble lifespans on multiple scales is summarized as follows:

(1) The principles required to explain the life of an air bubble were the Young-Laplace equation, Henry’s law, surface tension, void diameter, air bubble diameter, Boyle’s law, and balance between air bubble buoyancy and the vertical earth pressure above.

(2) Preventing air bubble formation is likely to be very difficult in natural waters unless pore water exists in an unusual degassed condition. In other words, few measures in nature will inhibit air bubble generation from pore water.

Chapter 6

The Seepage Failure Phenomenon with account for the Bubble Dynamics

6.1 The Seepage Failure Phenomenon on Multiple Scales

Figure 6.1.1 shows the temporal change in the safety factor, which was obtained by dividing the critical hydraulic gradient (Fig. 4.5.1(B)) by the hydraulic gradient (Fig.4.5.3). Seepage failure occurred when the safety factor was nearly at its smallest value in every case. Moreover, in L-1, where seepage failure did not occur, the safety factor did not change substantially. Therefore, ground seepage failure where the water-level difference is fixed is believed to occur because of the synergistic effect of the increase in the hydraulic gradient, a macroscopic process. This is associated with the decrease in the seepage distance and decrease in the critical hydraulic gradient, accompanied by an increase in the quantity of air bubbles, which are microscopic processes.

Figure 6.1.2 shows a flow chart of seepage failure that includes the influence of air bubbles. Seepage failure of ground containing air bubbles basically occurs because of the decrease in the critical hydraulic gradient i_{cr}, an increase in the void ratio e because of air bubble generation, and the increase in i accompanied by the decrease in L.

Based on the results obtained in this study, monitoring upstream ground surface displacement is particularly important for predicting seepage failure. However, since ground deformation is localized, particularly in dense ground, a system that can measure displacement over a wide area or a system that can predict the location of deformation would be required.

In the case of real scale ground conditions (a large overburden pressure or a large pore water pressure), bubble development hardly occurs because of the size of the bubbles due to external pressure. But, near the slope of a dike or in a shallow part of a ground with seepage, these phenomena can occur using the same mechanism, and bubbles can assist the seepage failure phenomenon. Moreover, since the majority of natural ground is undersaturated, the influence of air bubbles cannot be limited to river dikes. Therefore, the influence of air bubbles must be taken into consideration for any ground experiencing seepage flow. Since the results obtained in the holding test and re-raising test revealed that the danger of seepage failure increases when air bubbles exist in the ground, air bubbles remaining in ground after construction or air bubbles trapped by rainfall may negatively affect the strength of any ground.

To examine these phenomena, we are developing a numerical analysis to account for bubble effect using Smoothed Particle Hydrodynamics (Maeda et al., 2006).

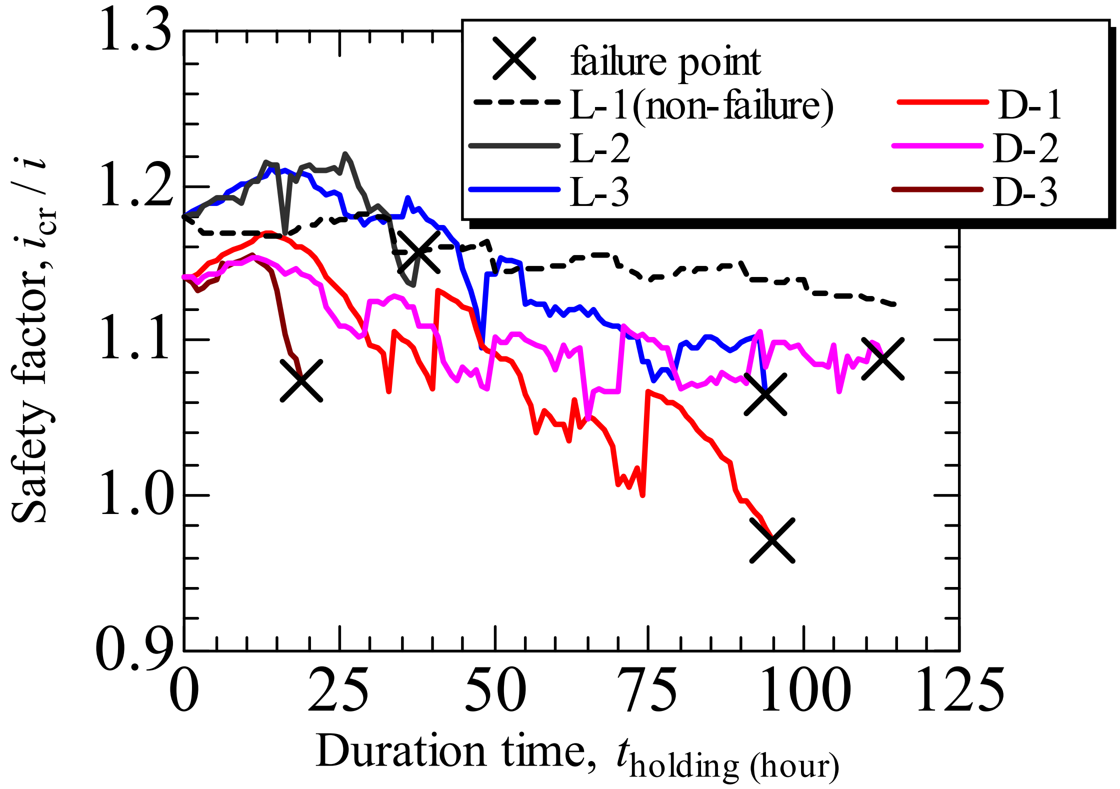

Fig.6.1.1 Changes in the safety factor: critical hydraulic gradient divided hydraulic gradient

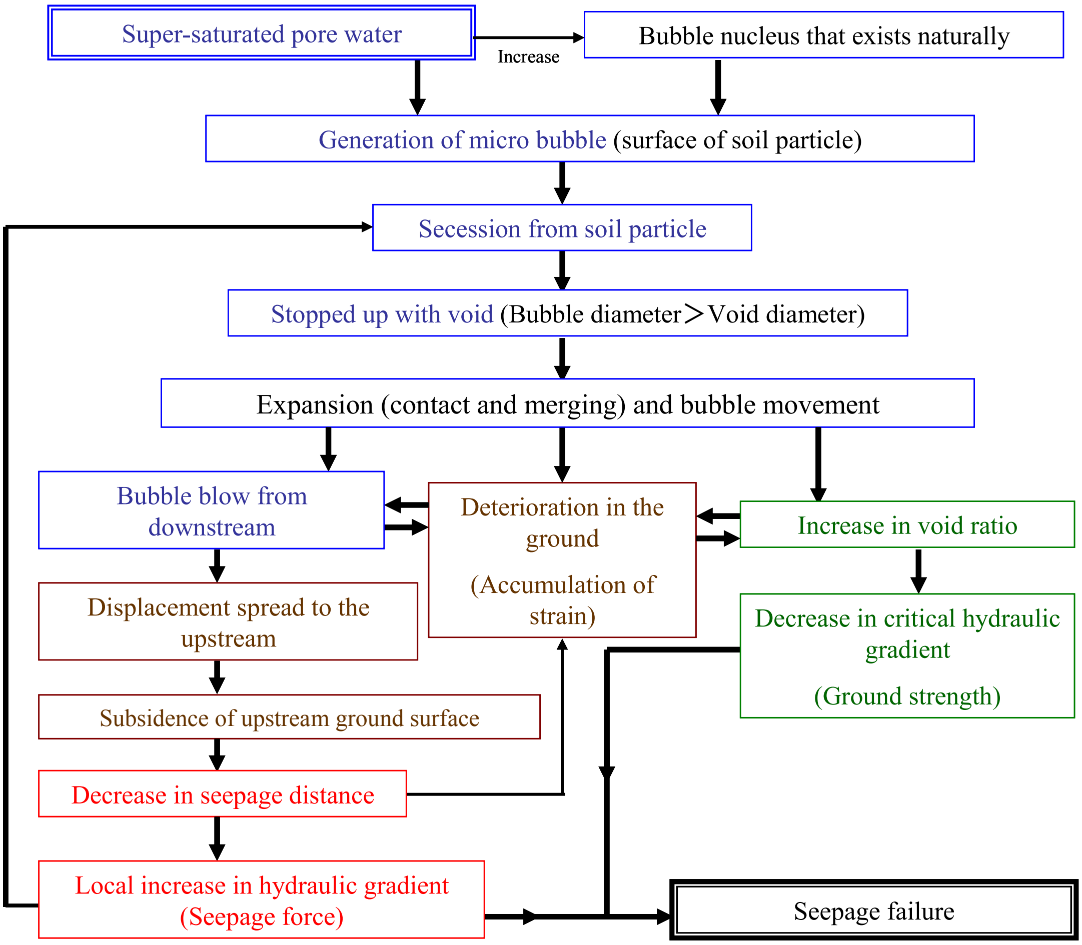

Fig.6.1.2 Flow Chart of seepage failure that considers the influence of bubble dynamics

6.2 Summary

In this study, a two-dimensional seepage failure experiment was performed on the region around a sheet pile. Three tests were employed: (1) a monotonic raising test, in which the water-level difference was monotonically raised, similar to the general seepage failure test; (2) a holding test, in which the water-level difference was maintained at a fixed value less than the critical water-level difference obtained in the monotonic raising test; and (3) a re-raising test, in which the water level was raised after the holding test. Based on the results obtained from these three tests, the effect of air bubbles on sandy ground was investigated macroscopically and microscopically to explain the mechanism of three-phase seepage failure, considering air bubble generation and development and the interactions between soil, water, and air. The results obtained in this study can be summarized as follows:

<*Macro scale*>

(1) The monotonic raising test showed that ground surface displacement started at approximately 80% of the critical water-level difference ΔH_{cr}, at which time the ground surfaces on both the upstream and downstream sides of the sheet pile were symmetrically deformed. The amount of ground surface displacement required for seepage failure was greater in dense ground than in loose ground.

(2) In the holding test, ground surface displacement occurred on both the upstream and downstream sides just after maintaining the water-level difference in loose ground. In dense ground, the ground surface displacement did not occur until later, but it progressed rapidly. Ground displacement on the upstream side occurred when air bubbles escaped from the ground on the downstream side. The region of ground displacement gradually propagated upstream the first air bubbles escaped from the ground on the downstream side.

(3) In the re-raising test, seepage failure first occurred at a water-level difference less than the critical water-level difference ΔH_{cr} (80%–90% of ΔH_{cr}). This means that the ground strength against seepage failure decreased by a maximum of 20% because of air bubbles.

(4) The index of supersaturation I_{ss} (similar to the relative density in geotechnical engineering) allowed the DO values measured during the tests to clearly express the degree of pore water supersaturation.

(5) Contrary to the results reported by Kodaka and Asaoka, air bubble generation was confirmed in the dense ground holding test, even when pore water was undersaturated. Air bubbles were believed to have been generated when during seepage, soil particles forcefully agitated pore water by.

(6) The speed of air bubble development depended on the ground density and I_{ss}. The speed increased as the ground density or I_{ss} increased. In dense ground, the development speed was not greatly affected by I_{ss}. The likely reason for this was that in dense ground, air bubble development was easier than in loose ground because many soil particles held air bubble nuclei and agitation was high. In other words, ground density substantially affected the initial development of air bubbles.

(7) In ground where air bubbles were already generated but had not yet been released, the strength against loading was 1/4–1/5 that of normal ground. The strength of the ground against loading decreased further because of the large quantity of accumulated air bubbles caused by a large overburden.

<Micro scale>

(1) Image analysis of ground displacement around a single air particle showed that an air bubble moved toward the ground surface while expanding and compressing owing to interactions among the bubble, the surrounding ground, and the seepage force. The air bub-

ble would then escape from the ground while forcefully shearing the surrounding ground.

(2) The principles required to explain the life of an air bubble were the Young-Laplace equation, Henry's law, surface tension, void diameter, air bubble diameter, Boyle's law, and balance between air bubble buoyancy and the vertical earth pressure above.

(3) A pore water supply was required for air bubble nuclei or generation of fine air bubbles (microbubbles). The development of microbubbles required the incorporation of pore water DO. Air bubbles became visible at the tip of the sheet pile downstream, where the hydraulic gradient i was largest and the static water pressure had begun to decrease. This finding agreed with those of Kodaka and Asaoka.

(4) From air bubble generation to escape, bubble's shapes changed from slender to globular to flat, and the bubbles gradually moved toward the surface while developing. Just before escaping, the air bubble shapes became slender, and the bubbles sheared the ground above forcefully as they escaped. At this moment, i increased locally and macroscopic seepage failure occurred.

(5) In the period between the holding test start and subsidence of the ground surface on the upstream side, the seepage distance L increased because of ground uplift on the downstream side accompanied by air bubble generation. When the ground upstream side started to subside, the seepage distance L decreased and became shorter than the initial distance in dense ground. The permeable water volume Q exhibited a similar trend. Even though the water-level difference was fixed, i increased as time progressed, and seepage failure also accelerated. In addition, the local deformation width W from the sheet pile was about $D/2$–D of the penetration depth of the sheet pile D in the ground upstream. This was about $D/2$ in the ground downstream, as pointed out by Terzaghi.

PART 2

Experimental Study on the Seepage Failure of Dike with account for Air Bubble Dynamics and Rainfall

Chapter 1

Seepage Failure Phenomenon of Dike Model

We investigated about seepage failure mechanism with account for air bubble dynamics in the PART 1. In this part, another experiment with account for rainfall was carried out to compare the seepage failure of dike. In this study, some geomaterial were used to compare these seepage characteristics. In addition, pore pressure and moisture content by volume were also obtained.

Chapter 2

Experimental Method and Procedure

2.1 Outline of experiment

In this part, the influence of bubble dynamics and rainfall are investigated by using some geomaterials (Silica sand, Kaolin clay and Toyoura sand). Some experimental condition (control of DO value etc.) are same as part 1, so only a point different from part 1 is written in section 2.2.

In this part, it pays attention to the appearance of phreatic lines and bubble development in the dike (especially, captured bubbles), and it is compared to examine the method of measures.

2.2 Experimental Apparatus and Procedure

The experimental apparatus shown in Fig. 2.2.1 was manufactured. In this experiment, Silica sand (No. 6), Toyoura sand, and mixture material (Silica sand and Kaolin clay; weight ratio=17:3) is used. Toyoura sand and Silica sand are dried, but mixture material is adjusted to become optimum moisture content (about 20 %). Coefficient of permeability of each materials are 1.6×10^{-2}, 8.5×10^{-3}, 3.5×10^{-4} cm/s, respectively.

Making procedure of a dike is as follows:

First, after arranging a loose two-base layer (thickness of both layer is equal to 50 mm) simulated ground dropped into the water, density of the ground was controlled by a tamping rod (degree of compaction is about 92 %). Then, dike part was made by the tamping every 50 mm thicknesses after dropped geomaterial into the air. Tap water was used, and DO of the water to rise the water level was controlled by a thermo regulator and air bubble generation device. Rainfall intensity was set to 124 mm / hour, and to keep uniformity of the moisture content of the ground, fog nozzle can move at the speed of 10mm/s. Experimental conditions are shown in Table 2.2.1. As for the rainfall condition, in case of prerainfall before raising water level, prerainfall time was written as the unit of minute. If water level rising and rainfall are given at the same time, prerainfall time was written as 0 minute. Fig. 2.1.3 indicates the install position of moisture meters.

In the dike experiment, strength against overflow of dike is defined as “residual height”, which is the difference of the first and last height.

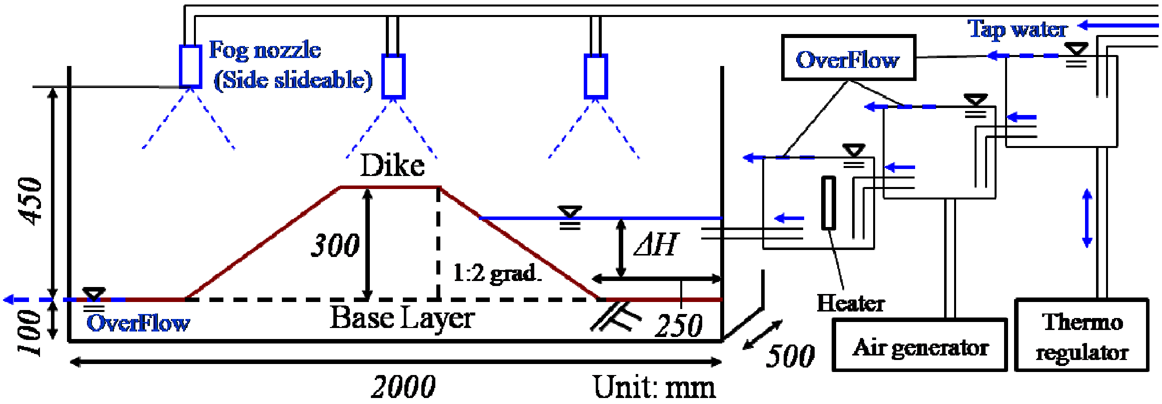

Fig.2.2.1 Experimental apparatus of seepage failure experiment of dike model

Table 2.2.1 Experimental conditions

		Monotonic raising	Holding
Toyoura sand	Without Rainfall	-	-
	Rainfall	(d) Prerainfall: 45min. (continued)	Prerainfall: 0 min. $\Delta H = 100$ mm
Silica sand No.6	Without Rainfall	(a) Yes	(e) $\Delta H = 250$ mm
	Rainfall	(b) Prerainfall: 0 min. (continued)	(f) Prerainfall: 30min. $\Delta H = 150$ mm
Mixture of Silica sand No.6 and Kaolin clay	Without Rainfall	-	$\Delta H = 100$ mm
	Rainfall	(c) Prerainfall: 0 min. (continued)	-

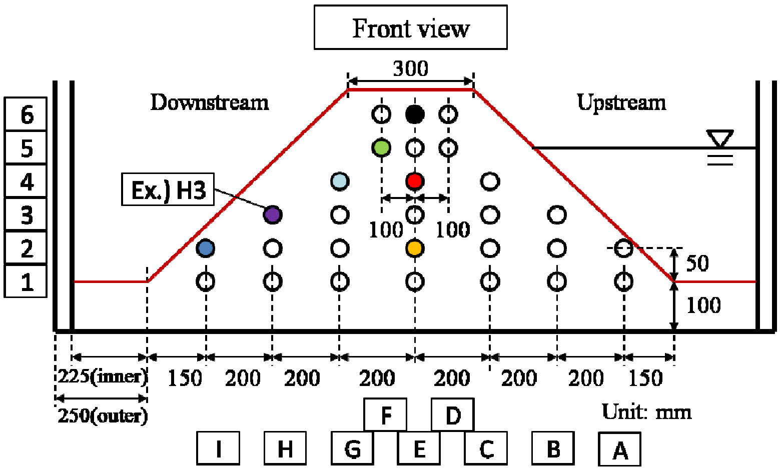

Fig.2.2.2 Install position of moisture meters: Front side of dike

Chapter 3

Experimental Results

3.1 Appearance of Phreatic Lines and Bubble Development in the Dike

In this section, appearance of phreatic line, external erosion of the slope of dike, internal erosion of the dike and development of bubble were investigated as shown in Table 2.2.1((a)-(f)).

3.1.1 Case (a): Monotonic Raising Test, Silica sand, without Rainfall

Figure 3.1.1 shows monotonic raising test using silica sand without rainfall. After phreatic line on the upstream side rises, phreatic line on the downstream side rises delaying. In addition, the top of the phreatic line on the upstream side is higher than the water level on the upstream side due to the effect of suction. The dike is saturated 0.5 h after the initiation, slope on the downstream side was washed out with water level raising. 1.33 h later, the dike was broken with overflow. No bubbles exist in the dike through this case.

3.1.2 Case (b): Monotonic Raising Test, Silica sand, with Rainfall

Figure 3.1.2 shows monotonic raising test using silica sand with rainfall at the same time of water level rising on the upstream side. Differ from Case (a), phreatic line is seen from the toe to the center of the slope on the downstream side, and unsaturated zone which was surrounded by some phreatic lines was made on the downstream side. After the external erosion of the slope surface on the downstream side due to rainfall, dike was broken in 1.33 h after the initiation. In this case, bubble did not exist in the dike.

3.1.3 Case (c): Monotonic Raising Test, Mixture soil, with Rainfall

In this case, monotonic raising test using mixture geomaterial (silica sand and kaolin clay) with rainfall at the same time of water level rising on the upstream side is performed. From the start of this experiment, intense erosion was occurred on the both upstream and downstream side slopes. Collected rainfall on the crest washed out slope surface. The crest becomes lower due to rainfall erosion, and dike was broken by overflow from the upstream side after 1 h initiation.

3.1.4 Case (d): Monotonic Raising Test, Toyoura sand, with Rainfall

Figures 3.1.3 to 3.1.9 show monotonic raising test using Toyoura sand with rainfall. Prerainfall time is 45 minutes. And Fig. 3.1.10 indicates the result of moisture meters. Just the point of the rainfall, phreatic lines generate from the edge of the dike on the both side (Fig. 3.1.3), these lines are generated to the crest (Fig.3.1.4). Figure 3.1.10 indicates these values rapidly decrease 0.5 h after the initiation. The likely reason for this is that bubbles are corrected into the dike. In addition, as shown in Fig. 3.1.10, amount of the decrease around the crest indicates the biggest value. This means that bubble is surrounded by the phreatic line from the lower side (with suction) and upper side (with rainfall). After that, when water-level difference increases with rainfall, phreatic line progresses to the center of the dike (Figs. 3.1.5 and 3.1.6). After sliding begins from the toe on the downstream side with water level raising, it progresses to the crest of dike (Fig. 3.1.7). And existence of a bubble is checked in this step. The likely reason for this is that bubbles captured into the dike are collected by both rainfall and phreatic line due to water level rising, and developed.

When water level at the upstream side becomes higher, a bubble to the upstream is compressed by the phreatic line (Fig. 3.1.8). When just before failure due to overflow, some cracks are developed around the crest, and air blow occurs from the crest (Fig. 3.1.9). In addition, as shown in Fig. 3.1.10, moisture content increases rapidly. This result indicates the escape of bubbles. And it thinks that the crack caused by a tension received from a bubble captured into the dike. This bubble causes uplift of the crest, and suction loses. These cracks and air blows are equal to the phenomenon witnessed at the Tokai Flood Disaster, so it says that this experiment can express the effect of bubble generation enough. After that, the dike was broken with overflow. There was no response of pressure meter through this case.

3.1.5 Case (e): Holding Test, Silica sand, without Rainfall, ΔH=250 mm

Figure 3.1.11 shows holding test (water-level difference equal to 250 mm) using silica sand without rainfall. This figure shows the slope on the downstream side. And just then, water-level difference rises. Some bubbles are blowing out from the toe. When water-level difference reaches to 250 mm, intense erosion occurs from the toe to the crest on the downstream side. And finally, dike was broken due to the erosion of the crest.

3.1.6 Case (f): Holding Test, Silica sand, with Rainfall, ΔH=150 mm

Figure 3.1.13 and 3.1.14 show holding test using silica sand with prerainfall. The time of prerainfall is 30 minutes, and holding water-level difference is 150 mm. After prerainfall, rainfall continues until the end of the experiment. As well as Case (b), slope surface was washed out due to the prerainfall (Fig. 3.1.13). After that, water-level difference rose. Erosion area on the downstream side expanded from the toe to the crest step by step, and this area reaches to the height of the water surface on the upstream side. Then, after erosion direction becomes parallel to the crest, dike was broken after 68 h initiation due to the erosion. In the holding test, micro bubbles are generated in the dike on the upstream side. But in this case, the influence of these bubbles is smaller than the influence of the erosion due to rainfall.

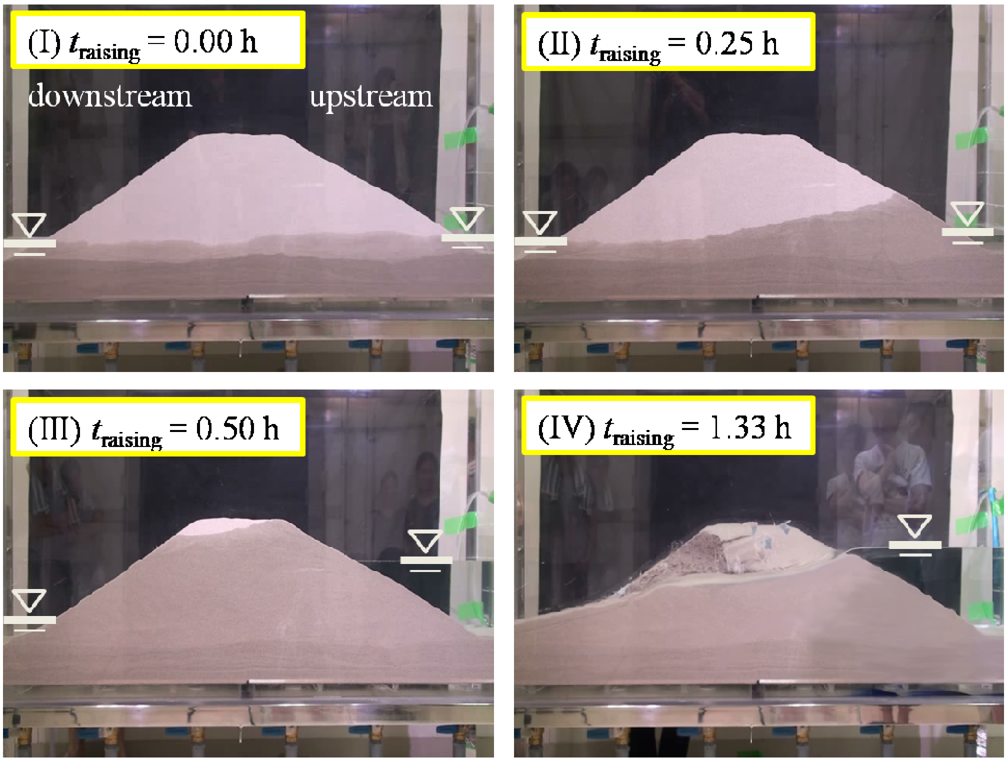

Fig.3.1.1 Appearance of the progress of phreatic lines in case of (a); Monotonic raising test, Silica sand, without rainfall

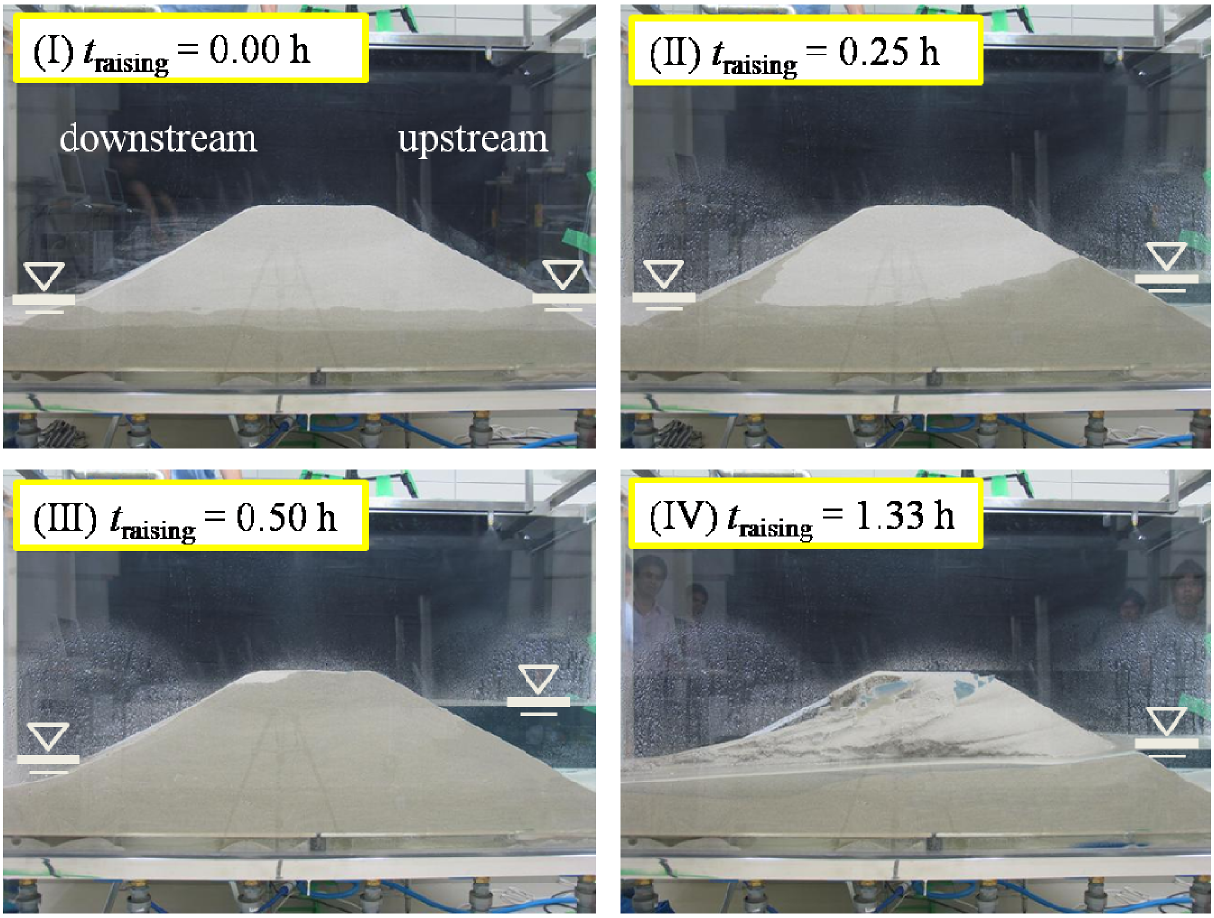

Fig.3.1.2 Appearance of the progress of phreatic lines; Case (b), Monotonic raising test, Silica sand, with rainfall (elapsed time after starting prerainfall = 0.00 h)

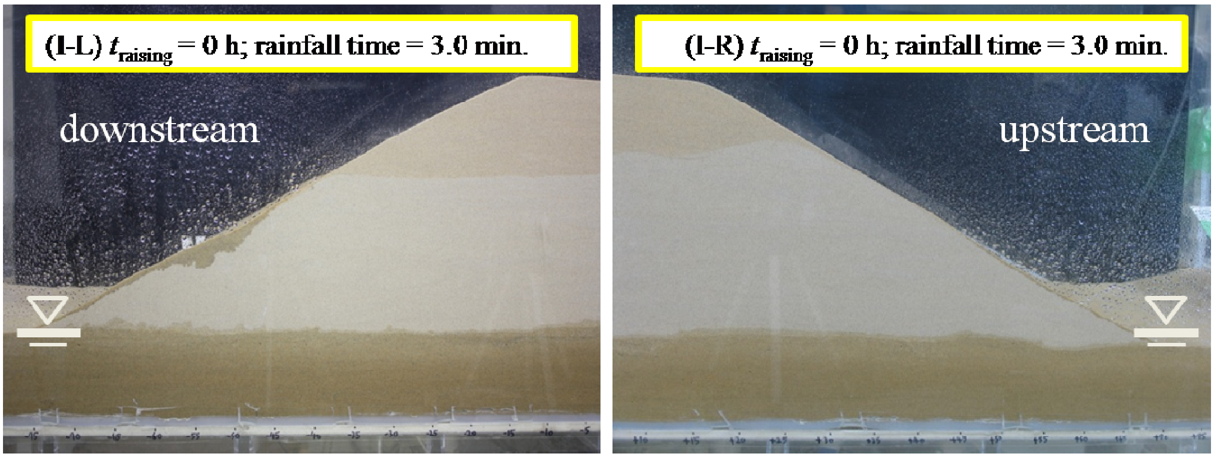

Fig.3.1.3 Case (d), Monotonic raising test, Toyoura sand, with rainfall (elapsed time after starting prerainfall = 3.0 min.); infiltration of downstream side slope

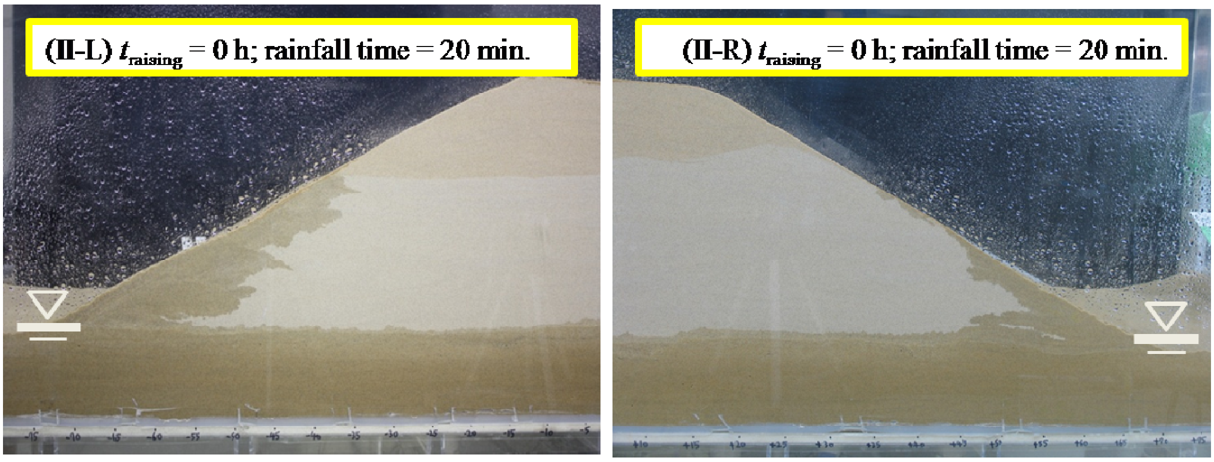

Fig.3.1.4 Case (d), Monotonic raising test, Toyoura sand, with rainfall (elapsed time after starting prerainfall = 20 min.); progress of infiltration from toe to crest

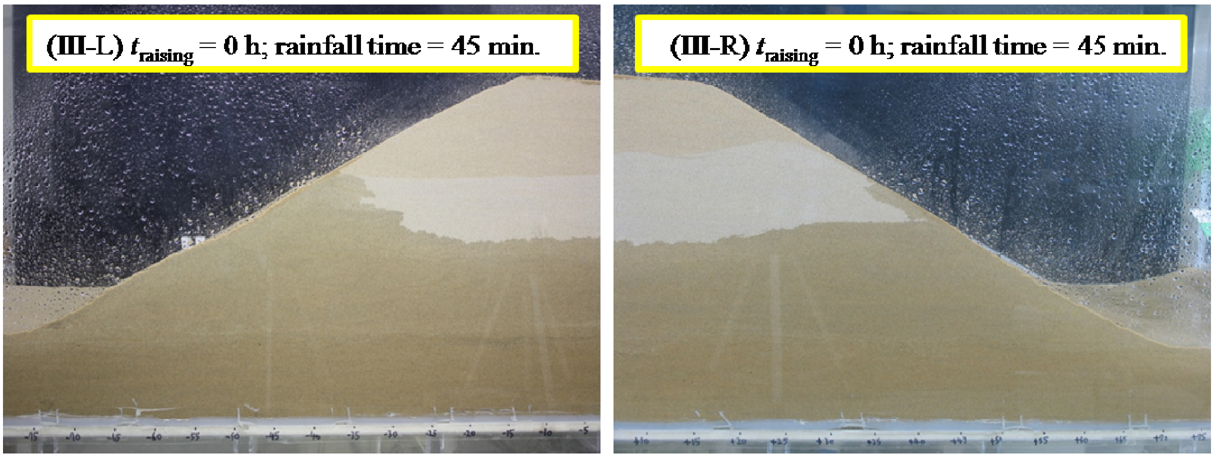

Fig.3.1.5 Case (d), Monotonic raising test, Toyoura sand, with rainfall (elapsed time after starting prerainfall = 45 min., t_{raising} = 0 h); infiltration to the hillside of the dike

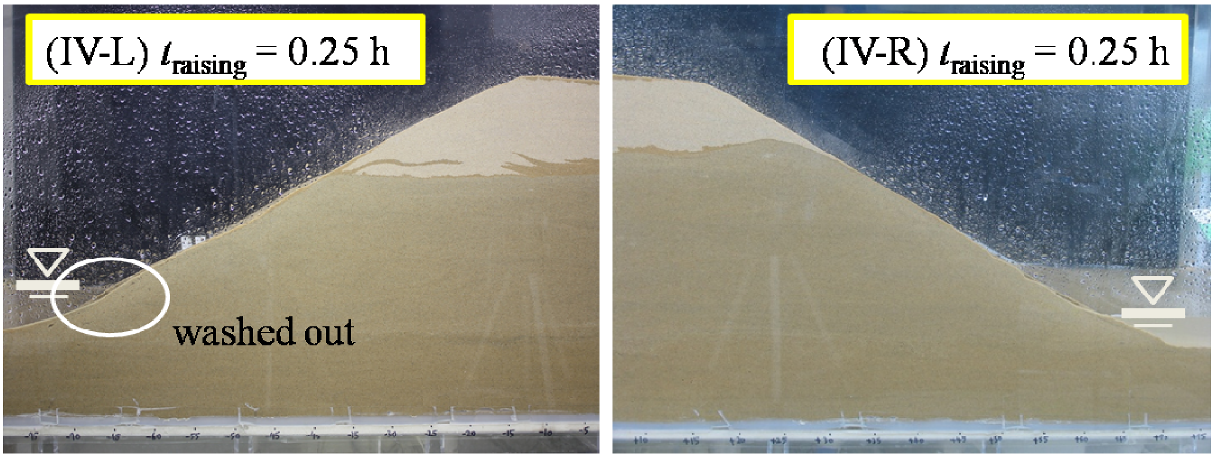

Fig.3.1.6 Case (d), Monotonic raising test, Toyoura sand, with rainfall (t_{raising} = 0.25 h); raising of phreatic area by water level raising, and the toe of downstream side are washed out

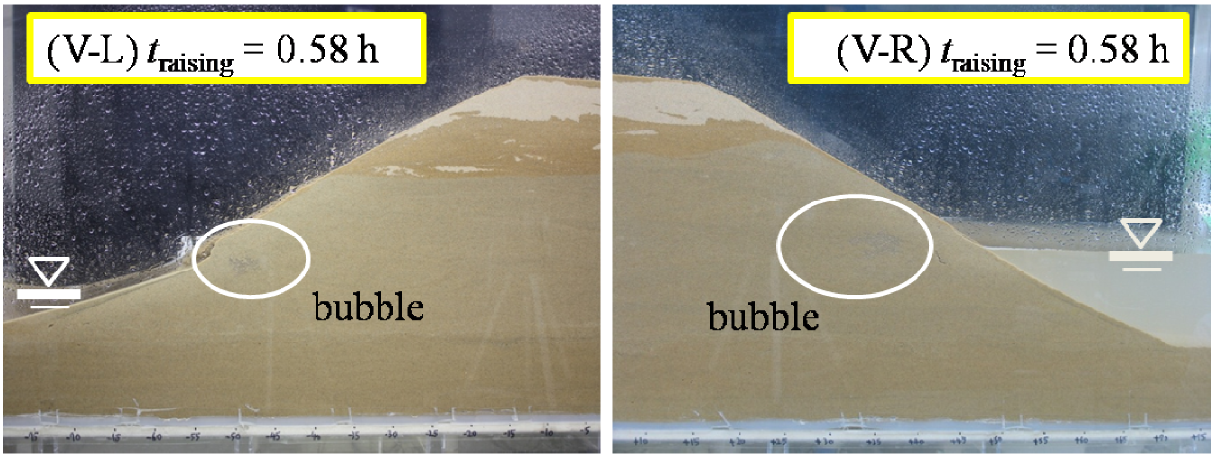

Fig.3.1.7 Case (d), Monotonic raising test, Toyoura sand, with rainfall ($t_{raising}$ = 0.58 h); generation of some bubbles in the dike

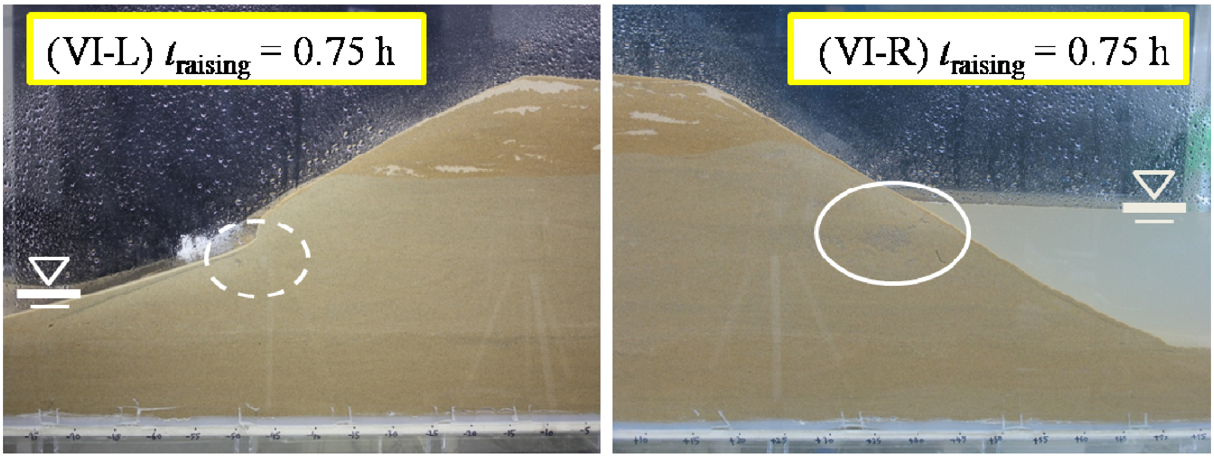

Fig.3.1.8 Case (d), Monotonic raising test, Toyoura sand, with rainfall ($t_{raising}$ = 0.75 h); blow out of the bubble from the downstream side

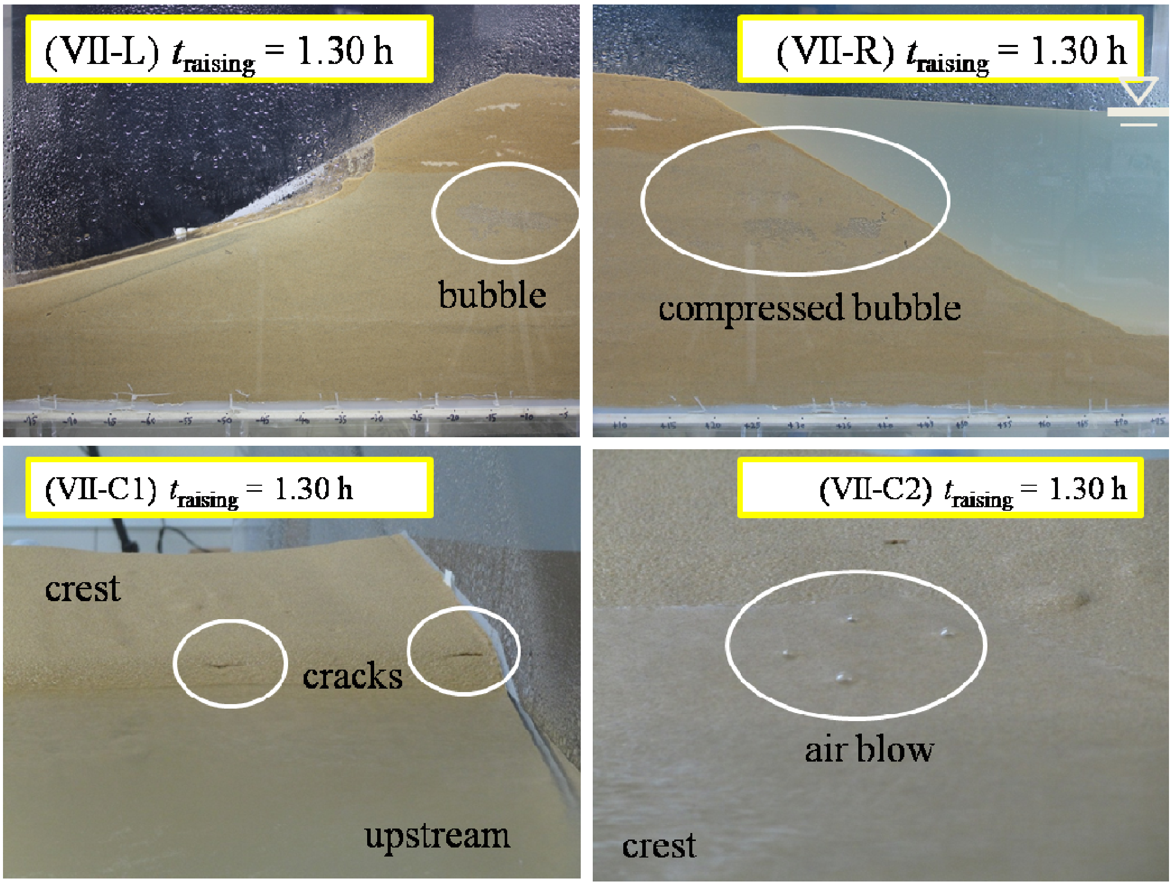

Fig.3.1.9 Case (d), Monotonic raising test, Toyoura sand, with rainfall ($t_{raising}$ = 1.30 h); compression of the bubble in the dike, generation of some cracks at the crest due to uplift of the bubble, and air blow from the crest of the dike (just before overflow)

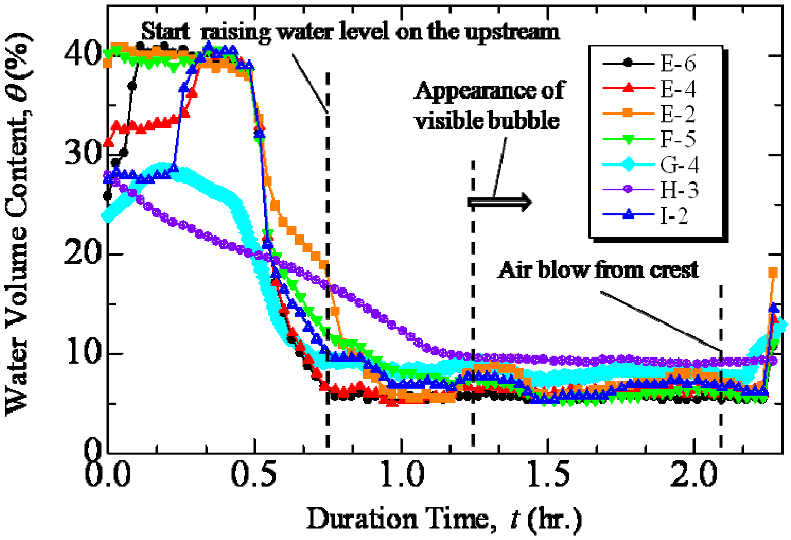

Fig. 3.1.10 Changes in the value of moisture content by volume; Case (d)

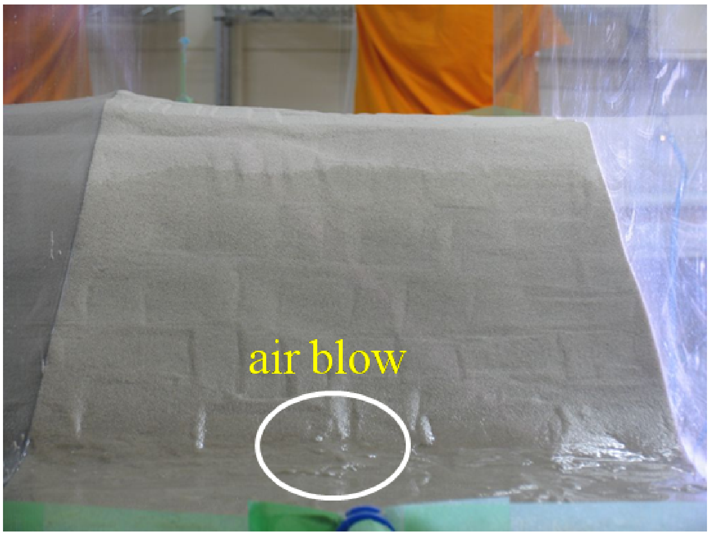

Fig. 3.1.11 Case (e), Slope of downstream; Holding test, Silica sand, without rainfall (just raising upstream water level)

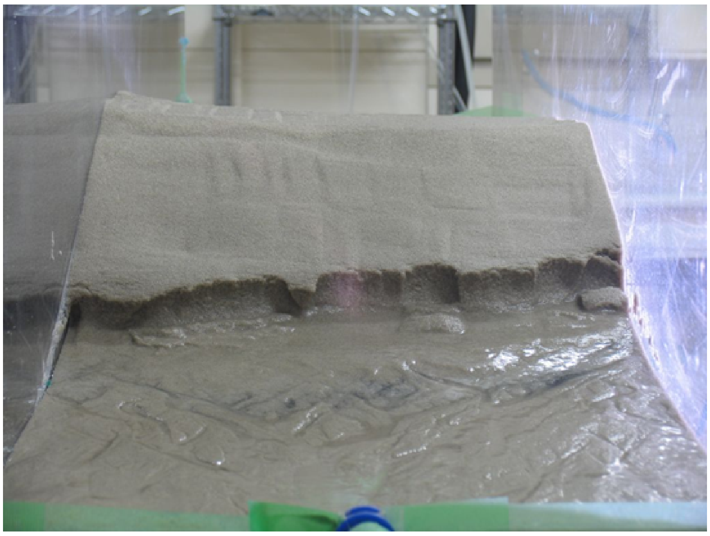

Fig. 3.1.12 Case (e), Progress of external erosion from toe to the crest

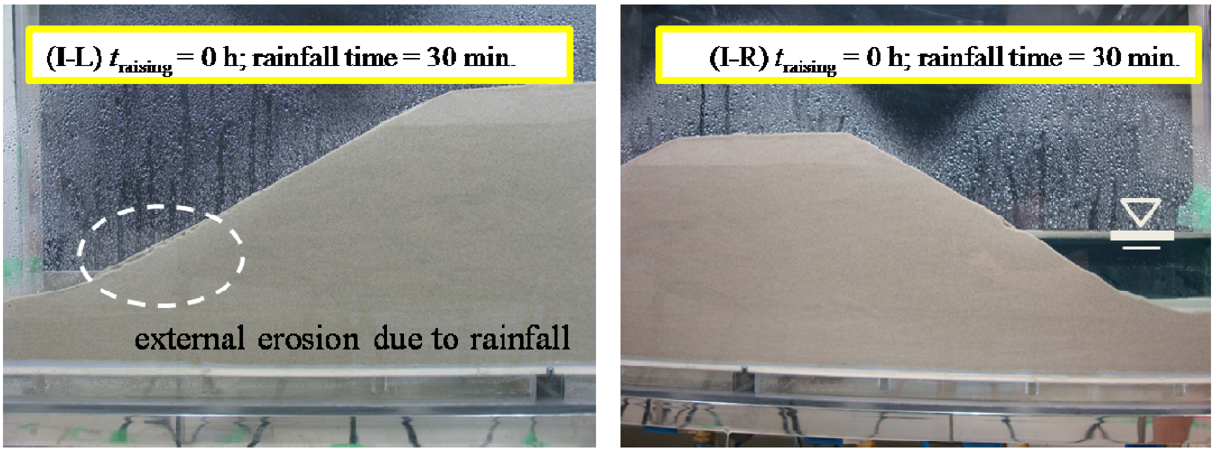

Fig. 3.1.13 Case (f), External erosion due to rainfall; Holding test, Silica sand, with rainfall (elapsed time after starting prerainfall = 30 min., $t_{\text{raising}} = 0$ h)

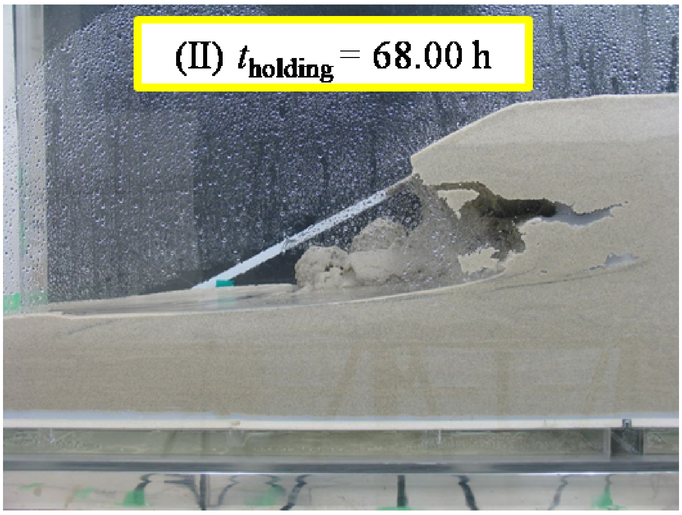

Fig. 3.1.14 Case (f), Progressive failure of the dike due to seepage and rainfall; $t_{\text{holding}} =$ 68.00 h

3.2 Residual Height against Overflow

Table 3.2.1 shows the all results of dike experiment. In monotonic raising test, the smaller coefficient of permeability is, the smaller residual height, too. And rainfall decreases the strength against overflow as shown in the result of silica sand.

In holding test, on the other hand, all results are same values as shown in Table. 3.2.1. So, it says that Toyoura sand became weak with bubble dynamics (captured bubble) due to rainfall (see Figs. 3.1.1 to 3.1.9).

And the comparison between monotonic raising test and holding test, it says that holding decrease the strength, too.

Table 3.2.1 residual height against overflow (mm)

		Monotonic raising	Holding
Toyoura sand	Without Rainfall	-	-
	Rainfall	160	129
Silica sand No.6	Without Rainfall	150	130
	Rainfall	142	132
Mixture of Silica sand No.6 and Kaolin clay	Without Rainfall	-	134
	Rainfall	135	-

3.3 Summary

In this part, appearance of the progress of phreatic line, erosion of the slope of the dike, influence of rainfall, and generation of bubble were investigated through the model test. The results obtained in this experimental study can be summarized as follows:

(1) Through almost all the experiment cases, dike was broken by overflow. So the measure against the overflow is important. In addition, there are two causes of the overflow. One is the water level rising at the upstream side, and another one is the decrease in the height of the crest due to rainfall. Therefore, to prevent from the erosion of dike slope with rainfall or overflow, protection of dike slope is needed.

(2) In case of low permeability soil use (Sec. 3.1; Case (c)), material of dike was washed out due to rainfall and seepage flow. On the other hand, high permeability materials (ex. Toyoura sand) have higher strength than low permeability materials against erosion of slope.

(3) In case of Toyoura sand use (Sec. 3.1; Case (d)), air bubble was captured by both phreatic line from lower side and rainfall. And then these bubbles caused the tension crack of dike. In addition, when these bubbles are blown off to outside, dike has some damage such as the decrease of density, local decrease in strength and local increase in seepage force (see Part 1).

(4) In some experimental conditions, micro bubbles were generated among a long period. Though these bubbles hardly influence the dike, these bubbles become bigger as time passed. So, the measure of the decrease in influence of air bubble is needed to make a strong dike in the overflow and seepage failure.

(5) In monotonic raising test, the smaller coefficient of permeability is, the smaller residual height, too. And rainfall decreases the strength against overflow as shown in the result of silica sand. In holding test, on the other hand, all results are same values. So, it says that Toyoura sand became weak with bubble dynamics due to rainfall.

PART 3

Development of the Seepage Failure Analysis Method of Ground with Smoothed Particle Hydrodynamics

Chapter 1

Outline of Smoothed Particle Hydrodynamics

Large flowage deformations and hydraulic collapse of ground (e.g. dikes) induced by permeation of water through ground, play important roles in the destabilization of dikes during floods, liquefaction and other damage mechanisms that occur during injection driving of pile and/or improvement materials into ground. It is necessary to model progressive seepage failure in the soil in order to analyze these phenomena more precisely. Reports have found important roles for interactions among all three phases in solids, liquids and gases (Kodaka and Asaoka, 1994; Nakajima, 1985; Maeda and Sakai, 2004; Sakai et al., 2005). The degree of saturation (JGS Technical Committee of mechanism of slope failure and prediction of degree of risk under heavy rains, 2003) and the super dissolved oxygen in void pores have major effects on seepage failure behavior in soil, and the occurrence of air bubbles in the base is an important issue in the weakening of dikes.

In this study, the development of a new analytical method for investigation of seepage failure was attempted in order to account for interactions among all three phases of soil, water and air. The smoothed particle hydrodynamics method (SPH), a completely mesh-free technique, was used to obtain the combined benefits of both discrete and continuum methods. SPH is a Lagrangian method employing particles that operate in place of the mesh in finite difference solutions of partial differential equations. This method was originally developed by

Gingold and Monaghan (Gingold and Monaghan, 1977) and Lucy (Lucy, 1977) in astrophysics to solve equations of motion for galaxies (Monaghan, 1988). Later, this method was applied to viscid flows and failure of solids (Monaghan and Gingold, 1983; Libersky et al., 1993; Monaghan, 1994; Benz and Asphaug, 1995; Randles and Libersky, 1996; Morris et al., 1997). In this paper, SPH with a new method for calculating density in multi-phase conditions is proposed. The seepage in the dike base is also expressed by devising equations for solid-fluid phase interactions. Very simple model experiments and qualitative analytical observations were also carried out in two dimensions.

Chapter 2

Analytical Method

In the following sections, outline of the SPH method, comparisons between continuum mechanics and SPH expressions for continuity and momentum equations are introduced with equation of state of fluid and constitutive model of soil used. Secondly, some improvements are proposed such as the calculation procedure of density with interface between different material and introduction of interactions between solid and fluid phases. Finally implementations of SPH analysis are explained.

2.1 Outline of SPH Method

The purpose of this study is to discuss and model interactions among the solid, liquid and gaseous phases. In this paper, we had an attempt to develop the analysis method to express the seepage failure. The continuity equation, equation of motion and the SPH formulations necessary to express two-dimensional seepage failure and the implementation are explained. Here, compressive stresses and strains are considered to be positive.

In the DEM, in order to examine actual particles and solve the corresponding equations of motion using finite time differences, a huge number of particles are required when handling a large analytical region. The SPH developed in this research is not intended for practical problems, but for solving an assembly of particles (Fig. 2.1.1), which are considered to be round (radius *h*), continuous bodies of finite volume. These particles overlap in the analytical region, and the equation of motion is solved with finite time differences for each particle. Soil "particles" here represent discrete volumes of soil rather than soil grains, and similarly water "particles" are finite volumes of water rather than individual molecules. Thus, this approach allows for a much faster solution for systems of large numbers of particles compared to DEM. Since this method uses the Lagrange equations, it can also express discrete behaviors such as sliding contact between particles, separation, and two- or three-phase inter-actions.

The motion of particles is dominated by the gradient of the stress exerted by neighboring particles; it, therefore, is not necessary to determine the parameters for spring elements in DEM which are hard to understand. We can calculate the stress-strain relation in particles using the same equation of state and constitutive equations as those for ordinary continuous media. This approach combines the benefits of both discrete analysis and continuum analysis into SPH.

As mentioned above, SPH describes the phase of interest as a superposition of multiple overlapping particles. The spatial mean value $<f(\mathbf{x})>$ of physical quantity $f(\mathbf{x})$ at an arbitrary point $\mathbf{x}$ is given by Eq. (2.1.1). Particles x' of physical quantity $f(\mathbf{x}')$ are located within the zone of influence of the first particle (assumed in this paper to be $2h$, double the radius h of the particle). The physical quantity is interpolated using a smoothing function (called kernel) W (see Figs. 2.1.1 and 2.1.2).

$$\begin{aligned} < f(\mathbf{x}) > &= \int f(\mathbf{x}')W(\mathbf{x}-\mathbf{x}',h)d\mathbf{x}' \\ &= \int f(\mathbf{x}')W(\mathbf{r},h)d\mathbf{x}' \end{aligned} \tag{2.1.1}$$

where $\mathbf{r} = \mathbf{x} - \mathbf{x}'$. The smoothing function W is defined by,

$$1 = \int W(\mathbf{r},h)d\mathbf{x}' \tag{2.1.2}$$

As h is zero, $<f(\mathbf{x})>$ can be denoted by $f(\mathbf{x})$. If the density at $\mathbf{x}$ is $\rho(\mathbf{x})$, Eq. (2.1.1) can be rewritten as

$$< f(\mathbf{x}) >= \int [f(\mathbf{x'})/\rho(\mathbf{x'})] W(\mathbf{r},h)\rho(\mathbf{x'})d\mathbf{x'} \tag{2.1.3}$$

The spatial differential of this function can be written as follows.

$$\nabla < f(\mathbf{x}) >= \int [f(\mathbf{x'})/\rho(\mathbf{x'})] \nabla W(\mathbf{r},h)\rho(\mathbf{x'})d\mathbf{x'} \tag{2.1.4}$$

Here, $\nabla = (\partial/\partial \mathrm{x}, \partial/\partial \mathrm{y})^{\mathrm{T}}$ is the gradient of the function.

Equation (2.1.3) is then discretized into finite particles. Let the location of the center of particle i, its mass, and density be represented by $\mathbf{x}_i$, m_i and ρ_i, respectively, and let the vector from the center of particle i to the center of particle j be represented by $\mathbf{r}_{ij}$. From Eqs. (2.1.3) and (2.1.4), $f_\mathrm{i} = <f(\mathbf{x}_i)>$, $\nabla f_i = \nabla<f(\mathbf{x}_i)>$ can be approximated as follows:

$$f_i =< f(\mathbf{x}_i) >\cong \sum_{j=1}^{N} m_j \frac{f_j}{\rho_j} W_{ij}(\mathbf{r}_{ij},h) \tag{2.1.5}$$

$$\nabla f_i = \nabla < f(\mathbf{x}_i) >\cong \sum_{j=1}^{N} m_j \frac{f_j}{\rho_j} \nabla W_{ij}(\mathbf{r}_{ij},h) \tag{2.1.6}$$

Here, N is the number of particles in the analytical region. As expressed in the next equation, N more precisely represents the number of particles within the zone of influence of the smoothing function of particle j.

$$\left|\mathbf{x}_i - \mathbf{x}_j\right| = \left|\mathbf{r}_{ij}\right| \le 2h_{ij}, \quad h_{ij} = \left(h_i + h_j\right)/2 \tag{2.1.7}$$

In SPH, the physical quantity $f_i = f(\mathbf{x}_i)$ moves with the center of particle i.

It has been proposed that the Gaussian distribution and several other distributions (Liu et al., 2003) should be used as the smoothing function W. However, the Gaussian distribution would be very inefficient for calculations because the zone of influence extends to infinity. In this study, the third-order B-spline function shown below was employed as it provides a smooth curve and a limited zone of influence whose radius $2h$. Here, $\mathbf{r}_{ij} = |\mathbf{r}_{ij}|$ and $S = \mathbf{r}_{ij}/h_{ij}$.

$$W_{ij} = \alpha_d \times \begin{cases} \frac{2}{3} - S^2 + \frac{1}{2}S^3 & 0 \le S < 1 \\ \frac{1}{6}(2-S)^3 & 1 \le S \le 2 \\ 0 & 2 < S \end{cases} \tag{2.1.8}$$

In this equation, α_d is selected in order to satisfy Eq. (2.1.2), with values of $1/h$, $15/7\pi h^2$, $3/2\pi h^3$ in one, two and three dimensions. The smoothing function and its first derivative in the two-dimensional case are shown in Fig. 2.1.2($h_i = h_j = h$).

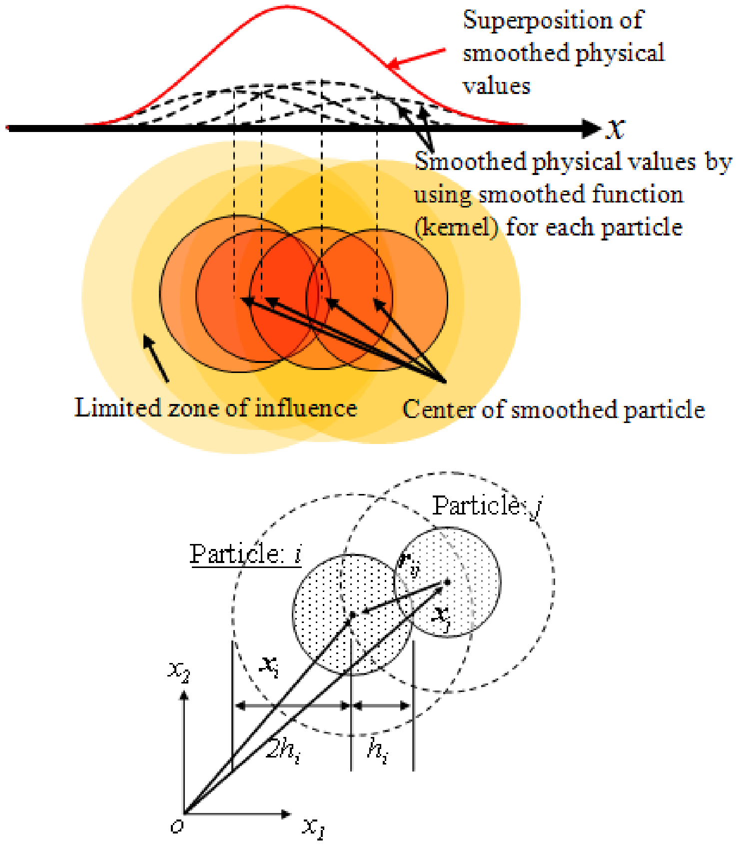

Fig.2.1.1 Expression of physical quantities using the smoothing function in SPH

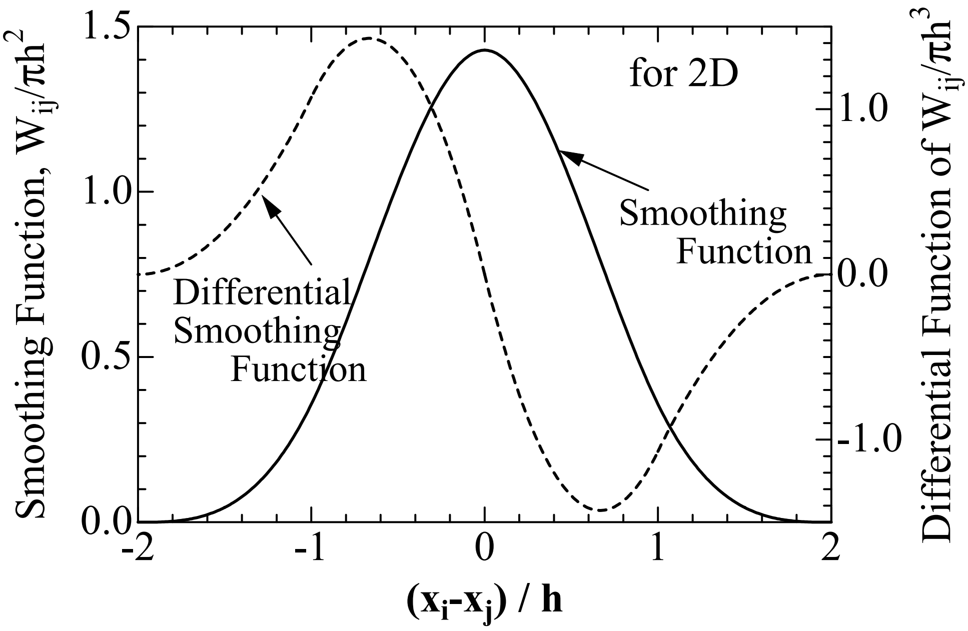

Fig.2.1.2 Characteristics of smoothing function incorporating geometric characteristics of particles in SPH

2.2 Continuum Continuity and Motion Equations

Generally, the continuity equation for material is written as follows using ρ and $\mathbf{v}$ as the density and velocity vectors, respectively:

$$\frac{d\rho}{dt} = -\rho\nabla\cdot\mathbf{v} = -\rho D \qquad (2.2.1)$$

$$\nabla\cdot\mathbf{v} = D \quad \text{(divergence)} \qquad (2.2.2)$$

where, '•' denotes the dot product of the vectors. When we observe a moving point within a body from a frame of reference moving with the body, the equation of motion using the stress tensor $\boldsymbol{\sigma}$ and the body force $\mathbf{f}$ is generally written as follows.

$$\frac{d\mathbf{v}}{dt} = -\frac{1}{\rho}\nabla\cdot\boldsymbol{\sigma} + \mathbf{f} \qquad (2.2.3)$$

Here, if the isotropic compressive stress component (mean principal stresses) and the deviator stress component are p and $\boldsymbol{\tau}$, respectively, $\boldsymbol{\sigma}$ can be re-written as

$$\boldsymbol{\sigma} = p\mathbf{I} + \boldsymbol{\tau} \qquad (2.2.4)$$

$$p = \left(\sigma_{yy} + \sigma_{xx}\right)/2 \qquad (2.2.5)$$

$$\boldsymbol{\tau} = \begin{pmatrix} -\left(\sigma_{yy} - \sigma_{xx}\right)/2 & \sigma_{xy} \\ \sigma_{yx} & \left(\sigma_{yy} - \sigma_{xx}\right)/2 \end{pmatrix} \qquad (2.2.6)$$

$$\mathbf{I} = \begin{pmatrix} 1 & 0 \\ 0 & 1 \end{pmatrix} \tag{2.2.7}$$

If the fluid is assumed to be non-viscous, $\boldsymbol{\tau} = \mathbf{0}$, and then Eq. (2.2.3) is reduced to

$$\frac{d\mathbf{v}}{dt} = -\frac{1}{\rho}\nabla p + \mathbf{f} \tag{2.2.8}$$

On the other hand, if the fluid is viscid, the Navier-Stokes equation becomes

$$\frac{d\mathbf{v}}{dt} = -\frac{1}{\rho}\nabla p + \upsilon\nabla^2\mathbf{v} + \mathbf{f}\,, \qquad \upsilon = \mu/\rho \tag{2.2.9}$$

where μ and ν represent the static and dynamic viscosities, respectively.

Next, the strain rate $\boldsymbol{\varepsilon}$ is defined by,

$$\dot{\boldsymbol{\varepsilon}} = -\frac{1}{2}\left\{\nabla\otimes\mathbf{v} + (\nabla\otimes\mathbf{v})^T\right\} \tag{2.2.10}$$

where $\otimes$ denotes the dyad product and the superscript T indicates the transverse of the matrix. As we denote shear strain and time differentiation by ε^d and ‘•’, respectively , the shear strain rate is expressed as

$$\dot{\boldsymbol{\varepsilon}}^d = \dot{\boldsymbol{\varepsilon}} - \frac{1}{2}Tr(\dot{\boldsymbol{\varepsilon}}) \tag{2.2.11}$$

The rotation speed ϖ is,

$$\varpi = -\frac{1}{2}\left\{\nabla\otimes\mathbf{v} - (\nabla\otimes\mathbf{v})^T\right\} \tag{2.2.12}$$

This purpose of study is to discuss and model interactions among the solid, liquid and gas phases. In this paper, we had an attempt to develop the analysis method to express the seepage failure. The continuity equation, equation of motion and the SPH formulations necessary to express two-dimensional seepage failure and the method of solution are explained.

2.3 Continuity and Motion Equations in SPH

Since SPH uses the Lagrangian algorithm, as long as the number of particles in the system does not increase or decrease, the continuity conditions are satisfied. Here, the method for calculating particle density is described. In this study, an improvement procedure for calculating density was employed in order to ensure that the continuity conditions are satisfied even in mixtures of materials with greatly differing densities and constitutive models. The conventional method is summarized and the schemes are described below.

2.3.1 Conventional Procedure forEestimation of Density

First, the density ρ_i of particle *i* is replaced with the density ρ_i found with function f_i in Eq. (2.1.3).

$$\rho_i = \sum_{j=1}^{N} m_j \frac{\rho_j}{\rho_j} W_{ij} = \sum_{j=1}^{N} m_j W_{ij} \qquad (2.3.1)$$

The SPH expression of Eq. (2.2.1) is also derived. First, since

$$\begin{aligned} \rho \nabla \cdot \mathbf{v} &= \nabla \cdot (\rho \mathbf{v}) - \mathbf{v} \cdot \nabla \rho \\ &\cong \nabla \cdot \langle \rho \mathbf{v} \rangle - \mathbf{v} \cdot \nabla \langle \rho \rangle \end{aligned} \qquad (2.3.2)$$

when Eq. (2.3.2) is substituted into Eq.(2.2.1) and the continuity equation for particle *i* (x_i, y_i) is $\nabla_i = (\partial/\partial x_i, \partial/\partial y_i)^T$, we have

$$\frac{d\rho_i}{dt} = -\left[\nabla_i \cdot \langle \rho \mathbf{v} \rangle - \mathbf{v}_i \cdot \nabla_i \langle \rho \rangle\right] \qquad (2.3.3)$$

Next, using Eq. (2.1.6),

$$\nabla_i \cdot \langle \rho \mathbf{v} \rangle = \sum_{j=1}^{N} m_j \mathbf{v}_j \cdot \nabla W_{ij} \tag{2.3.4}$$

$$\mathbf{v}_i \cdot \nabla_i \langle \rho \rangle = \sum_{j=1}^{N} m_j \mathbf{v}_i \cdot \nabla W_{ij} \tag{2.3.5}$$

When Eqs. (2.3.4) and (2.3.5) are substituted into Eq. (2.3.3), the differential form of the continuity equation becomes

$$\begin{aligned} \frac{d\rho_i}{dt} &= \sum_{j=1}^{N} m_j (\mathbf{v}_i - \mathbf{v}_j) \cdot \nabla_i W_{ij} \\ &= \sum_{j=1}^{N} m_j \mathbf{v}_{ij} \cdot \nabla_i W_{ij} \end{aligned} \tag{2.3.6}$$

Here, $\mathbf{v}_{ij} = \mathbf{v}_i - \mathbf{v}_j$, and ∇_i is the gradient for particle i with respect to the coordinate system (x_i, y_i).

2.3.2 Improvement in Estimation of Density Proposed

When Eq. (2.3.1) is used, since there will be fewer fixed particles than loose particles in the vicinity of the free interface, the density tends to be underestimated in that region. This problem can be avoided by using Eq. (2.3.6), the differential form. Alternatively, the next equation can also be used, in which the smoothing functions are summed for normalization (Randles and Libersky, 1996).

$$\rho_i = \frac{\sum_{j=1}^{N} m_j W_{ij}}{\sum_{j=1}^{N} \left(\frac{m_j}{\rho_j} \right) W_{ij}} \tag{2.3.7}$$

However, some improvements to this relation are necessary in order to calculate the density in the vicinity of the interface between phases in multi-phase conditions. In other words, in the vicinity of the interface between phases with greatly differing state equations and densities, even Eq. (2.3.7) will result in large errors in the calculations of density. For example, consider the situation of air bubbles in water. The state equations for air and water are different, and water is roughly one thousand times denser than air. This causes an underestimate in the water density near bubble surfaces and an overestimate of the air density on the air side of the interface. The calculation then fails because the pressure is estimated at physically impossible high or low values due to these misestimates of density. This cannot be avoided by using either of Eqs. (2.3.1), (2.3.6) or (2.3.7).

In this study, this problem is avoided by the summating (Σ) all elements of each given phase when using Eq. (2.3.7). The following equations show the present approach for a 2-phase mixture combining *Material a* and *Material b* represented by respective particles.

$$\rho_{i \in Material\ a} = \frac{\sum_{j=1 \in Material\ a}^{N} m_j W_{ij}}{\sum_{j=1 \in Material\ a}^{N} \left(\frac{m_j}{\rho_j}\right) W_{ij}} \quad \text{for Material a;} \qquad (2.3.8)$$

$$\rho_{i \in Material\ b} = \frac{\sum_{j=1 \in Material\ b}^{N} m_j W_{ij}}{\sum_{j=1 \in Material\ b}^{N} \left(\frac{m_j}{\rho_j}\right) W_{ij}} \quad \text{for Material b;} \qquad (2.3.9)$$

The above approach allows the densities of the different materials to be calculated with high precision everywhere, including the vicinity of phase interfaces. Investigations into approaches to the accurate and simple calculation of density will be continued for cases of changes in system mass (as in Eq. (2.3.6)), and in cases involving more abrupt, discontinuous changes in density.

2.3.3 Conventional Procedure for Calculation of Motion Equation

Second, the SPH adaptation of the equation for particle *i* in Eq. (2.2.8) is explained as follows. The quantity $1/\rho \nabla \rho$ must be calculated in order to solve the motion of particle *i*, as given by

$$\begin{aligned}\frac{1}{\rho}\nabla p &= \nabla\left(\frac{p}{\rho}\right)+\frac{p}{\rho^2}\nabla\rho \\ &\cong \nabla\left\langle\frac{p}{\rho}\right\rangle+\frac{p}{\rho^2}\nabla\langle\rho\rangle\end{aligned} \tag{2.3.10}$$

Substituting this equation into Eq. (2.2.8), the equation of motion for particle *i* becomes

$$\frac{d\mathbf{v}_i}{dt} = -\nabla_i\left\langle\frac{p}{\rho}\right\rangle+\frac{p_i}{\rho_i^2}\nabla_i\langle\rho\rangle+\mathbf{f}_i \tag{2.3.11}$$

In addition, Eq. (2.1.6) can be used as follows.

$$\nabla\left(\frac{p}{\rho}\right)\cong\nabla_i\left\langle\frac{p}{\rho}\right\rangle=\sum_{j=1}^{N}m_j\frac{p_j}{\rho_j^2}\nabla W_{ij} \tag{2.3.12}$$

$$\nabla\rho\cong\nabla_i\langle\rho\rangle=\sum_{j=1}^{N}m_j\nabla W_{ij} \tag{2.3.13}$$

Equations (2.3.12) and (2.3.13) can be substituted into Eq. (2.3.11) to obtain the following SPH version of the equation of motion for particle *i*:

$$\frac{d\mathbf{v}_i}{dt} = -\sum_{j=1}^{N}m_j\left(\frac{p_j}{\rho_j^2}+\frac{p_i}{\rho_i^2}\right)\nabla W_{ij}+\mathbf{f}_i \tag{2.3.14}$$

In the same way, Eq. (2.2.3) can be rewritten as

$$\frac{d\mathbf{v}_i}{dt} = -\sum_{j=1}^{N}m_j\left(\frac{\boldsymbol{\sigma}_j}{\rho_j^2}+\frac{\boldsymbol{\sigma}_i}{\rho_i^2}\right)\cdot\nabla W_{ij}+\mathbf{f}_i \tag{2.3.15}$$

The methods proposed by Morris et al. (Morris et al., 1997) and Monaghan and Gingold (Monaghan and Gingold, 1983) can also be employed for the viscosity term of a fluid and the artificial viscosity of a solid to convert Eqs. (2.3.14) and (2.3.15) into Eqs. (2.3.16) and

(2.3.17):

$$\begin{aligned}\frac{d\mathbf{v}_i}{dt} &= -\sum_{j=1}^{N} m_j \left(\frac{p_j}{\rho_j^2} + \frac{p_i}{\rho_i^2} \right) \nabla W_{ij} \\ &\quad + \sum_{j}^{N} \frac{m_j \left(\mu_i + \mu_j \right) \mathbf{v}_{ij}}{\rho_i \rho_j} \left(\frac{1}{r_{ij}} \frac{\partial W_{ij}}{\partial r_i} \right) \\ &\quad + \mathbf{f}_i\end{aligned} \tag{2.3.16}$$

$$\frac{d\mathbf{v}_i}{dt} = -\sum_{j=1}^{N} m_j \left(\frac{\boldsymbol{\sigma}_j}{\rho_j^2} + \frac{\boldsymbol{\sigma}_i}{\rho_i^2} + \Pi_{ij} \mathbf{I} \right) \cdot \nabla W_{ij} + \mathbf{f}_i \tag{2.3.17}$$

Here,

$$\Pi_{ij} = \begin{cases} \dfrac{-\alpha \bar{c}_{ij} \mu_{ij} + \beta \mu_{ij}^2}{\bar{\rho}_{ij}} & \mathit{if}\ \mathbf{v}_{ij} \cdot \mathbf{r}_{ij} < 0 \\ 0 & \mathit{otherwise} \end{cases} \tag{2.3.18}$$

$$\mu_{ij} = \frac{\mathbf{r}_{ij} \cdot \mathbf{x}_{ij}}{\left| \mathbf{r}_{ij} \right|^2 + \varepsilon_{AF} h^2}, \quad \varepsilon_{AF} = 0.1 \tag{2.3.19}$$

$$\bar{c}_{ij} = \left(c_i + c_j \right) / 2, \quad \bar{\rho}_{ij} = \left(\rho_i + \rho_j \right) / 2 \tag{2.3.20}$$

where c_i is the speed of a compression wave through the medium of particle i. The term Π_{ij} in Eq. (2.3.17) represents artificial viscosity pressure between particles i, j which are in physical proximity ($\mathbf{v}_{ij} \bullet \mathbf{r}_{ij} < 0$). This plays the role of a virtual damper to moderate interpenetration in particle collisions (ε_{AF} is a coefficient to prevent divergence). The literatures suggest $\alpha = 0.001$ and $\beta = 0.0$. It will be necessary to investigate how appropriate these values are for geomaterials.

The strain rate tensor $\dot{\boldsymbol{\varepsilon}}$ (Eq.(2.2.10)) and rotation tensor ϖ (Eq.(2.2.12)) for particle i are converted as follows.

$$\dot{\boldsymbol{\varepsilon}}_i = \frac{1}{2} \sum_{j=1}^{N} \left[\frac{m_j}{\rho_j} \mathbf{v}_{ij} \otimes \nabla_i W_{ij} + \left(\frac{m_j}{\rho_j} \mathbf{v}_{ij} \otimes \nabla_i W_{ij} \right)^T \right] \tag{2.3.21}$$

$$\varpi_i = \frac{1}{2} \sum_{j=1}^{N} \left[\frac{m_j}{\rho_j} \mathbf{v}_{ij} \otimes \nabla_i W_{ij} - \left(\frac{m_j}{\rho_j} \mathbf{v}_{ij} \otimes \nabla_i W_{ij} \right)^T \right] \tag{2.3.22}$$

2.4 Equations of State for Fluids and Constitutive Models of Soil Used

The initial pressure, the pressure at an arbitrary time, and the pressure deviation are denoted by p_0, p and p_d, respectively, and the bulk modulus is denoted by B. The equation of state for the gas phase (Batchelor, 1967) is given by

$$p_d \equiv p - p_0 = B\frac{\rho - \rho_0}{\rho_0} \qquad \text{for gas} \qquad (2.4.1)$$

where B is determined by

$$B = \gamma_{gas} \cdot p \qquad \text{for gas} \qquad (2.4.2)$$

The ratio of specific heat at constant pressure to specific heat at constant volume is γ_{gas} = 1.403 for air.

The liquid phase (e.g., water) is assumed to be incompressible. Then, as the pressure is calculated from the density in SPH, the following state equation is employed to handle quasi-incompressible fluids (Batchelor, 1967).

$$p_d \equiv p - p_0 = p_0\left\{\left(\frac{\rho}{\rho_0}\right)^{\gamma_{liq}} - 1\right\} \qquad \text{for water} \qquad (2.4.3)$$

Here, γ_{liq} was set equal to 7 (Monaghan, 1994). The lower this value is, the higher the compressibility of water is. This value was selected because the speed of compression waves in water is defined by the bulk modulus and density. In Eq. (2.4.3), changes in density have a large effect on changes in pressure; even small changes in density suffice to bring about large changes in pressure. Actual calculations using this value showed changes of density of less than 0.1%, a good approximation of incompressibility.

There is no need for special measures in the constitutive model for the solids in the analytical method proposed here, and any constitutive model appropriate for the problem can be employed. Many useful constitutive models and experimental laws are proposed in geomechanics (Wood, 2004). However, one of the most simplified models was used in the present analysis. An elastic-perfectly plastic solid was assumed. Other assumptions in this analysis were as follows: all dilatancy angles $\varphi_d = 0$, Poisson's ratio $\nu^e = 0.3$ and maximum (ultimate) shear stress of soil $\tau_f = p \tan \phi$ (with zero cohesion), where ϕ is the internal friction angle at failure. The shear stiffness G^e and Young's modulus E^e were defined as stretching odd functions of mean effective principal stress:

$$E^e = 2(1+\nu^e)G^e = E^e{}_0\left(\frac{p}{p_0}\right)^m \tag{2.4.4}$$

The bulk modulus of soil B^e is

$$B^e = \frac{E^e}{2(1-\nu^e)} = \frac{1}{2(1-\nu^e)}E^e{}_0\left(\frac{p}{p_0}\right)^m \tag{2.4.5}$$

Here, p_0 and $E^e{}_0$ are the standard stress and the stiffness corresponding to that stress, respectively. Under the above assumptions, the volumetric changes of soil particles depend only on the changes in effective mean principal stress in the elastic region such that the density of the soil is determined by its porosity n, allowing estimation of the effective mean principal stresses. When the relation of the increase in shear stress $\dot{\boldsymbol{\tau}}$ accompanying the deviator strain rate $\dot{\boldsymbol{\sigma}}$ is within the elastic region, it is common to use the relation described by Hooke's law,

$$\dot{\boldsymbol{\tau}} = 2G^e\dot{\boldsymbol{\varepsilon}}_{\mathbf{d}} \tag{2.4.6}$$

However, when rotation is taking place in the displacement field, the Jaumann rate is used instead. Then, Eq. (2.4.6) is re-written as follows (Libersky et al., 1993; Benz and Asphaug, 1995).

$$\hat{\boldsymbol{\tau}} = \dot{\boldsymbol{\tau}} - \varpi \cdot \boldsymbol{\tau} + \boldsymbol{\tau} \cdot \varpi = 2G^e\dot{\boldsymbol{\varepsilon}}_{\mathbf{d}} \tag{2.4.7}$$

Equation (2.4.7) also employs the results of Eqs. (2.2.4), (2.3.21) and (2.3.22). In this study, the initial porosity n_0 was set at 0.4 and m at 0.5. The standard stress and stiffness were set at $p_0 = 100$ kPa and $E^e{}_0 = 150$ MPa, and $\tan \phi = 0.5$ was used.

2.5 Interaction between Solid and Fluid Proposed

For this study, the solid phase, soil, and the fluids of water and air were handled on different layers (see Fig. 2.5.1). These layers were then combined to obtain the analysis of the three-phase system. Sugino and Yuu (Sugino and Yuu, 2002) successfully performed two-phase analysis by using a finite-difference method for the porous fluid (air), where SPH is used only for one phase. Since the purpose in this study is to simulate free surfaces, phase transport and separation in all phases, we applied the SPH method to all phases.

When combining the solid phase layer with the fluid phase layer, the model accounts for the physical forces described below, with due consideration of the effects of the porosity n and the coefficient of permeability k for water (or air). The frictional body forces resulting from velocity differences between two adjacent phases were employed as the above physical forces. The mixture theory (Biot, 1941; Prevost, 1979) was used here, writing the force by the solid phase on the liquid phase and the force by liquid on solid, respectively, as $\mathbf{f}^{sf}$ and $\mathbf{f}^{fs}$

$$\mathbf{f}^{sf} = n^2 \frac{\rho_f g}{k}\left(\mathbf{v}^s - \mathbf{v}^f\right), \quad \mathbf{f}^{fs} = n^2 \frac{\rho_f g}{k}\left(\mathbf{v}^f - \mathbf{v}^s\right) \tag{2.5.1}$$

By Newton’s third law of motion:

$$\mathbf{f}^{sf} = -\mathbf{f}^{fs} \tag{2.5.2}$$

where ρ_f is the density of the fluid phase, g is the gravity acceleration (9.8m/s), and $\mathbf{v}^s$

and $\mathbf{v}^f$ are the velocity vectors of the solid and liquid phases, respectively. Flowage deformation and failure behavior of the solid phase are dependent upon the effective stress. Here, the pore water pressure p was found using the method described below. The pressure in each liquid particle found using Eq. (2.4.3) was substituted into Eq. (2.1.5) for f_i for calculation of the pore water pressure. The continuity and balance in the multi-layers must be hold.

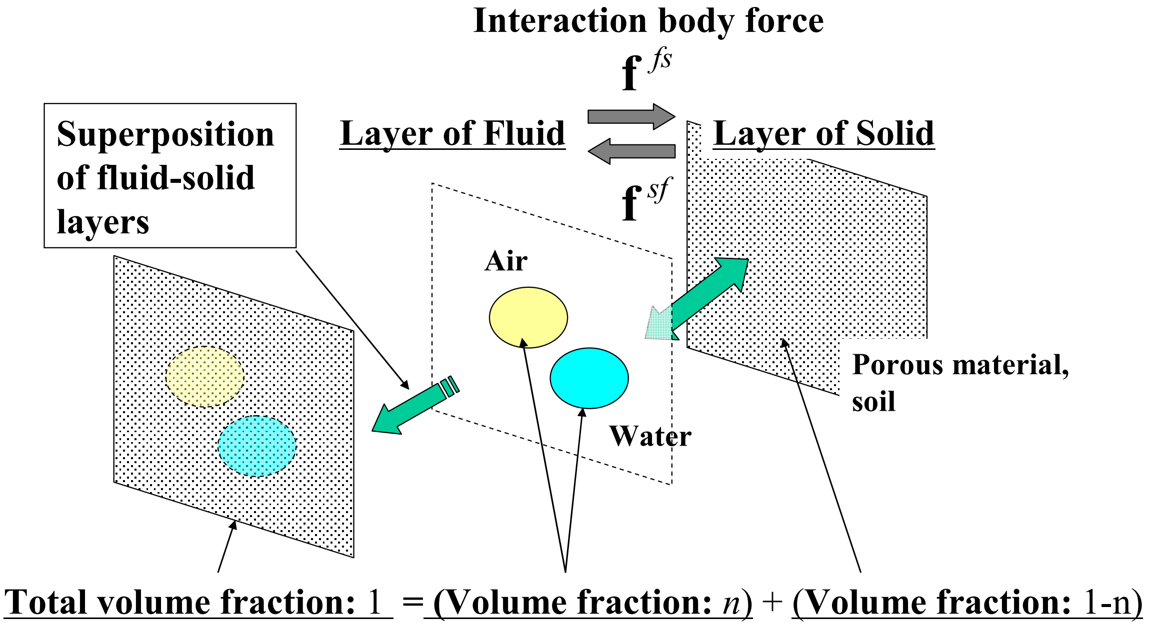

Fig.2.5.1 Equilibrium and interactions between solid phase (soil) and fluid phased (liquid, gas), superposition of fluid layer (air, water) and solid layer (porous medium, i.e. soil)

2.6 Time Integration

This analysis uses the leap-frog method (Hockney and Eastwood, 1999) with Eqs. (2.3.17) and (2.5.1) to estimate particle acceleration, location, density, strain and stress. From step n to step $n+1$, the physical quantity was calculated as shown below. The time steps from calculation step n–1 to n and from n to $n+1$ are written Δt^{n-1}, Δt^{n}, respectively:

$$\begin{aligned}
\mathbf{v}^{n+1/2} &= \mathbf{v}^{n-1/2} + 1/2\left(\Delta t^{n} + \Delta t^{n-1}\right)\frac{d\mathbf{v}}{dt}\bigg|^{n} \quad , \\
\rho^{n+1} &= \rho^{n}\left(1 - D^{n-1/2}\Delta t\right), \\
\mathbf{x}^{n+1} &= \mathbf{x}^{n} + \mathbf{v}^{n+1/2}\Delta t\,, \\
\boldsymbol{\sigma}^{n+1} &= S\left(\rho^{n+1}, \mathbf{x}^{n+1}, \ldots\right).
\end{aligned} \tag{2.6.1}$$

Time step Δt was determined using the Courant-Friedrichs-Levy (CFL) conditions, as follows.

$$\begin{aligned}
\Delta t_1 &\le 0.25\min\left(h_i / c_i\right), \\
\Delta t_2 &\le 0.25\min\sqrt{\left(h_i / \left|\dot{v}_i\right|\right)}, \\
\Delta t_3 &\le 0.125\min\sqrt{\left(h_i / \nu_i\right)}, \\
\Delta t &= \min\left\{\Delta t_1, \Delta t_2, \Delta t_3\right\}.
\end{aligned} \tag{2.6.2}$$

2.7 Treatment of Boundary

To realize a better physical meaning of the boundary, the behavior of phase boundary was reproduced by creating an array of virtual boundary particles, as shown in Fig. 2.7.1. If each boundary particle is defined with the proper location and momentum, it will be possible to apply slip and non-slip boundary conditions for the fluid phase. This treatment resembles the use of ordinary virtual cells used in the finite difference method with grids. When calculating the density and solving the equations of motion for particle a (free particle) moving freely in the analysis region, a virtual velocity is applied to boundary particles B within the affected range (satisfying Eq. (2.1.7)), which are then handled as ordinary particles. However, the positions of the boundary particles are not updated using the virtual velocity and there are no interactions between boundary particles.

The method of Morris et al. (Morris, 1997) that improved the method of Takeda et al. (Takeda et al., 1994) was used here to handle the virtual velocity $\mathbf{v}_B$ of boundary particle B. The effect of $\mathbf{v}_B$ on free particle a was calculated according to the distance between the particle a and the boundary using the following equation. The conditions are non-slip and the boundary shape is a straight line (Fig. 2.7.1).

$$\mathbf{v}_{aB} = \mathbf{v}_a - \mathbf{v}_B = \beta \cdot \mathbf{v}_a \tag{2.7.1}$$

The maximum permitted value of β ($\beta_{\max}$) is pre-determined.

$$\beta = \min\left(\beta_{\max},\ 1 + d_B / d_a\right) \tag{2.7.2}$$

Here, the lower the value of d_a, the greater the value of β. In this case, $\beta_{\max}$ was set to 2.0 to prevent β from reaching extreme values and overestimating the reaction forces exerted on other particles near the boundary. This approach, allowing adjustment of different parameters, seems promising for modeling of various boundary conditions.

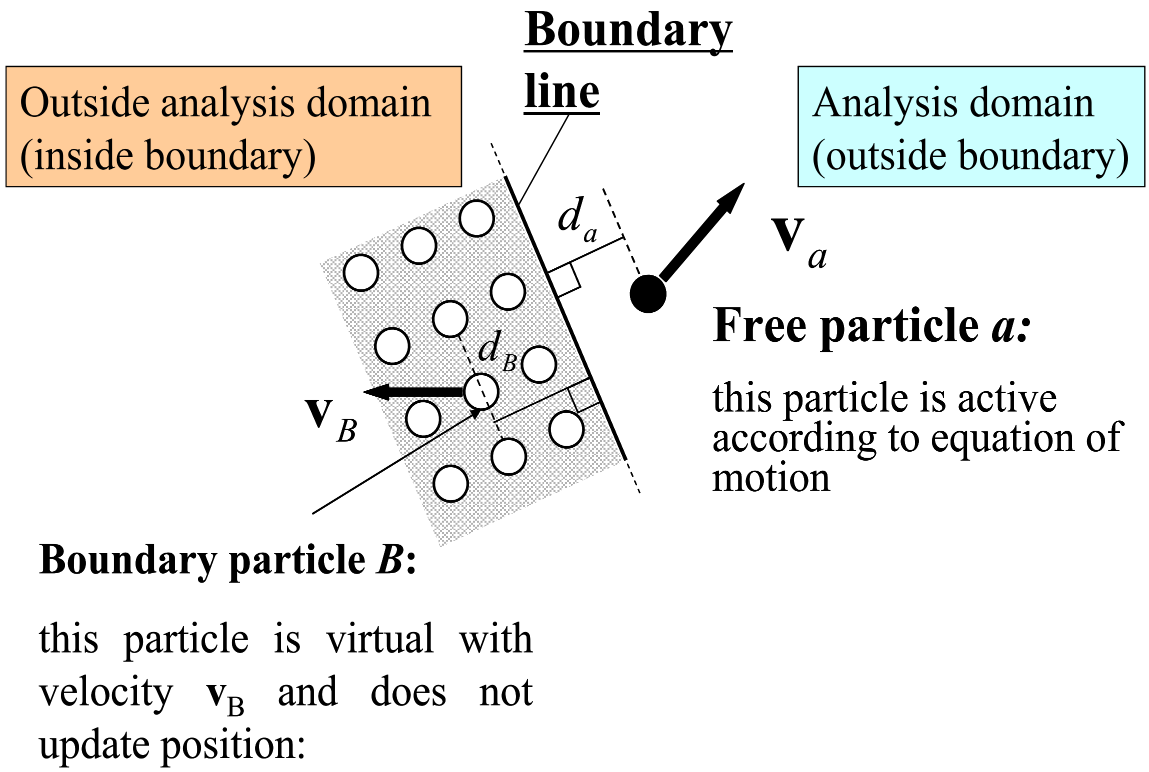

Fig.2.7.1 Virtual velocity of particles under non-slip boundary condition; boundary particle B is located on the opposite side of the boundary line of the analysis domain of free particles

2.8 Introduction of Suction

As shown in section 3.1, PART 2, it is easily understood that suction has acted remarkably in the dried dike. So, we proposed the method of easily expressible of the effect of suction.

First, capillary height of pore water in the soil is expressed as follows (Yamaguchi, 1988);

$$h_c = \frac{0.38}{D\sqrt{e}} \tag{2.8.1}$$

Here, h_c, D and e are, respectively, capillary height (unit: cm), mean diameter of soil particle (unit: cm) and void ratio. In this study, D has been treated as the 50 percent particle size, D_{50}. To use the capillary height, it is necessary to provide both surface of the water and rising speed of the water. The former is decided by the boundary condition. At this time, the original density calculation method (equation 2.3.1) is used to examine the position of the surface of the water. The lattar is provided by using the saturate-unsaturated coefficient of permeability of the soil

Calculation procedure is as follows;

(1) The water particle that exists in the soil is found.
(2) Void ratio and water volume content is calculated at the position of the water particle.
(3) Capillary height is calculated by void ratio and mean diameter of the soil particle.
(4) Rising speed of the water is calculated by using the relationship between saturate-unsaturated coefficient of permeability, k (cm/s), and water volume content, θ.
(5) The increment of capillary height is added to the position of the water particle.

In this analysis, D_{50} and e_0 (initial void ratio) were set up 0.2 (mm) and 0.7. Approximation of relationship between k and θ is as follows;

$$\ln(k) = \begin{cases} 1.0\times 10^{-5} & \theta \le 0.1 \\ 0.6356 + 5.514\times \ln\theta & 0.1 < \theta < 0.4 \\ 1.0\times 10^{-2} & \theta \ge 0.4 \end{cases} \tag{2.8.2}$$

2.9 Implementation of SPH Analysis

Figure 2.9.1 shows a flow diagram of the calculations in SPH.

First, a particle is located in the analysis region and its initial mass, density and other parameters are set. In this study, the particles were placed on an orthogonal grid. Each particle was initially defined with an identical radius *h* and an identical zone of influence, of radius 2*h*.

The value of *h* was updated in each calculation step in accordance with the changes in density (divergence D_i) (Benz and Asphaug, 1995).

$$h^{n+1}{}_i = h_i^n - \Delta t \frac{h_i^n}{\rho_i^n \cdot d} \sum_{j=1}^{N} m_j \left(\mathbf{v}_i^n - \mathbf{v}_j^n \right) \cdot \nabla_i^n W_{ij} \tag{2.9.1}$$

As often performed in DEM, the analysis region was partitioned into cells, and the particles within each particle's zone of influence were efficiently identified and recorded. This procedure was performed using a linked list in order to minimize memory usage in PC (Hockney and Eastwood, 1999). After determining the density, the fluid pressure and other parameters were calculated from the equation of state. The exerted forces and accelerations were then found from the inter-particle stress gradient, with consideration of the interactions between the solid and fluid layers. For the present assumption of quasi-compressibility of the fluid instead of incompressibility in SPH (Eq. (2.4.3)), Monaghan has proposed an approach called "*XSPH*" in which the velocity is revised. The velocity vector $\mathbf{v}'_i$ found in the previous process is thusrevised as velocity $\mathbf{v}_i$, which is given by

$$\mathbf{v}_i = \mathbf{v}'_i - \varepsilon_{XSPH} \sum_{j=1}^{N} m_j \mathbf{v}'_{ij} W_{ij} \tag{2.9.2}$$

where ε_{XSPH} is a constant ($0 \le \varepsilon_{XSPH} \le 1$). The larger ε_{XSPH} is, the greater the effect of this operation for moderating the velocity of the particle of interest to match the average velocity of the surrounding particles is. This avoids one particle penetrates into adjacent particles in high-speed flows.

The strain rate is calculated by the revised velocity, and the overall strain is then updated. The internal strain condition of each particle is also updated by calculating the strain rate from the constitutive equation.

Finally, the location of the particle is updated, and the above process is repeated. Next chapter describes the analytical results obtained using this SPH method with the objective of reproducing two-dimensional fracture. The initial particle radius h_0 and inter-particle distances were identical in all cases examined. The gravitational constant g was set equal to 9.8 m/s^2.

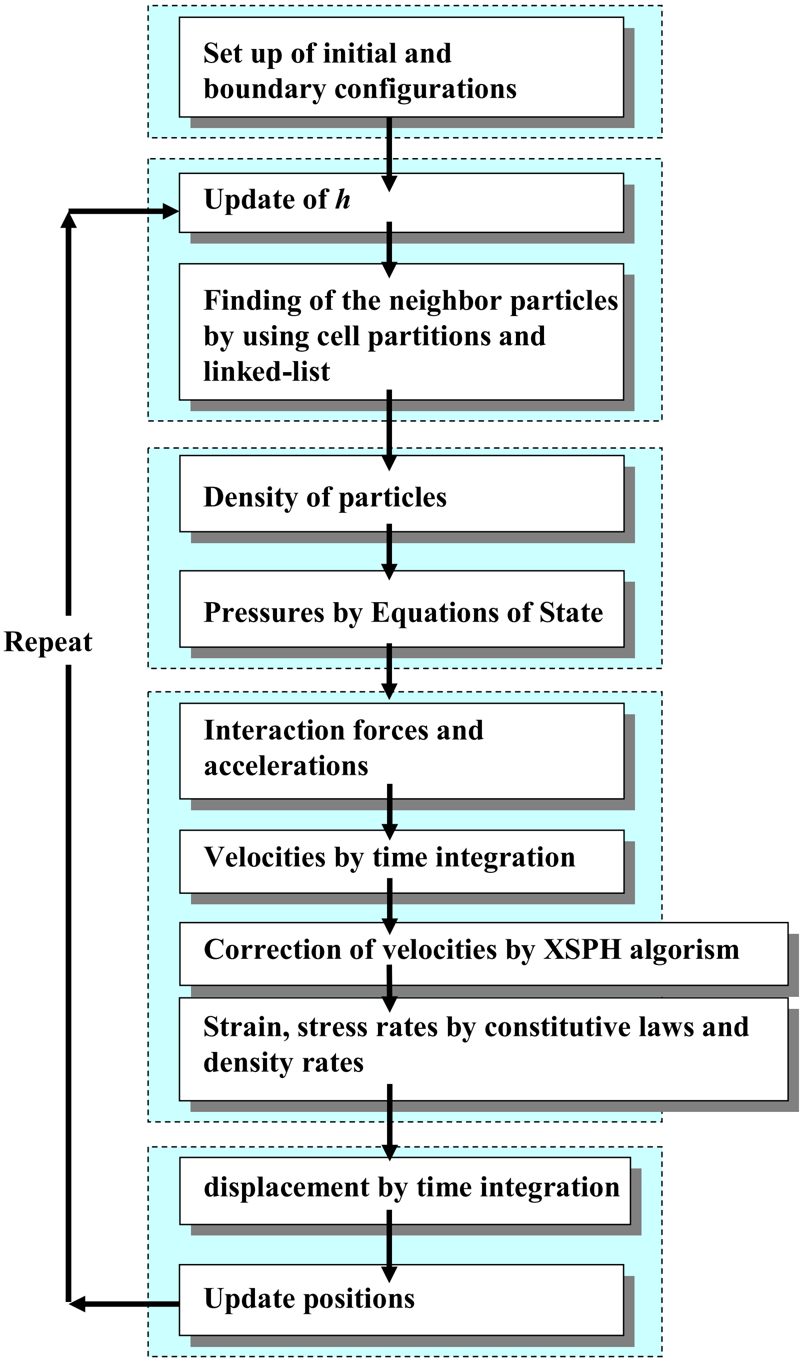

Fig.2.9.1 Flow of calculations in SPH

Chapter 3

Analytical Results and Discussions

3.1 Liquid phase (Single-phase)

Figures 3.1.1 and 3.1.2 show the results of the SPH analyses for the collapse of liquid columns over a range of μ values (Monaghan, 1994). The viscosity for Fig. 3.1.1 is 1.002×10^{-3} N·s/m^2, and that for Fig. 3.1.2 is 1.002 N·s/m^2, 1,000 times higher than the case of Fig. 3.1.1. The centers of the particles along the right side of the column (the boundary particles) were initially aligned with the center of the vessels. The radii of the dots in the figures are 1/4 of the size of the particles analyzed in the models. The red dots represent boundary particles, and blue dots denote liquid particles; we confirmed that the analysis results were fitted to experimental results (Martin and Moyce, 1952).

The initial density of all particles was set at ρ_0 = 1000 kg/m^3 and zero initial speeds in the figure were applied to the liquid particles on the right side of the column (H, y as defined in the figures). Figure 3.1.1 shows a time series of the collapse, consisting of a sideward flow with speed increasing with distance downward from the upper surface. After sufficient time, the water surface took a flat shape. In Fig. 3.1.2, not only did the collapse take much more time due to the higher viscosity, but the initial shape was also held for longer. Thus, the SPH method successfully reproduces the fluid flow phenomena.

Figure 3.1.3 shows the comparison between benchmark experimental results and analytical results. As shown in this figure, analytical results have quantitatively good agreement with benchmark test.

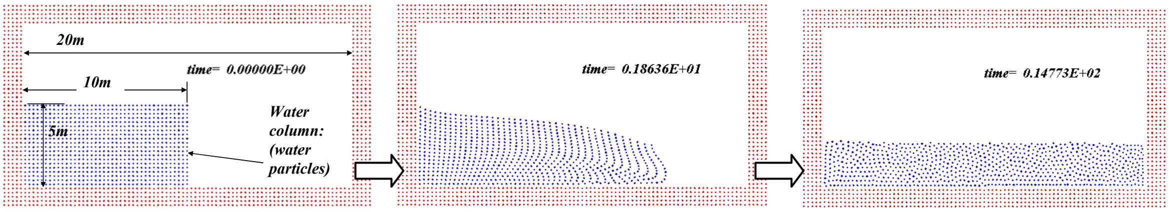

Fig.3.1.1 Analysis of collapse pf fluid column (dam break); viscosity of water, time in seconds

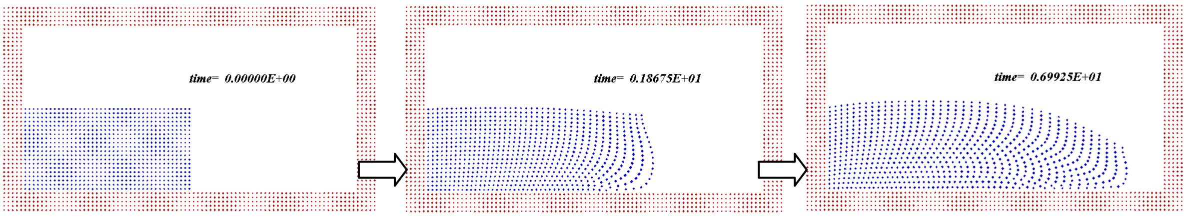

Fig.3.1.2 Analysis of collapse of fluid cokumn; fluid viscosity is 1000 times that of water

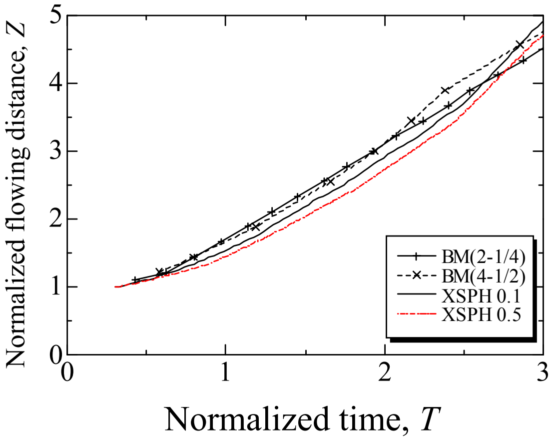

Fig.3.1.3 Comparison between benchmark experimental results and analytical results by using normalization type density equation

3.2 Gas-Liquid System (Two-phases)

Figures 3.2.1 and 3.2.2 show the results of analyses of the rise, burst and coalescence of bubbles in fluids, as predicted by SPH. The liquid was assigned the same characteristics as the water in the previous section. The properties of the gas were set at values characteristic of air: initial density $\rho_0 = 1.207$ kg/m^3, viscosity $\mu = 1.810 \times 10^{-5}$ N·s/m^2.

No particles were located higher than the upper surface of the water. However, this volume was assumed not to be a vacuum but to have a pressure of100 kPa (about 1 atm.) Accordingly, the bubbles in the liquid were assigned a pressure of 100 kPa and densities corresponding to the pressure at the water depth predicted by Eqs. (2.4.1) and (2.4.2). The bubbles were simulated using clusters of SPH gas particles. Figure 3.2.1 shows the analytical results with consideration of the surface tension of the water-air surface. The bubble rises with the passage of time, simulating the effect of buoyancy. The outline of the bubble changes as it rises and the surface of the water also lifts above the bubble. Circulation occurs as the liquid fills the space below the bubble. As it rises, the bubble breaks into a nearly straight row of smaller rising bubbles. This process clearly shows the changes in rise speed when it is viewed as a movie. The collapse of the water surface is also portrayed. The particles of air in the bubble continue rising into the air after emerging from the water surface. Thus, the SPH method appears to reproduce a variety of motions and hydraulic collapse behaviors in fluid phases.

Surface tension occurs when different substances are in contact, and this tension varies with the substances and with the shape of the interface. Although a number of existing analytical approaches search for the interface and calculate the surface tension, since the surface tension is a fundamental force between molecules, this intermolecular force is incorporated into SPH taking full advantage of the discrete properties defined by SPH. This study referred the method of Nugent and Posch (Nugent and Posch, 2000) to add an intermolecular force term $-(a/m^2)\cdot\rho^2$ resembling the effect of van der Waals forces to the p pressure term in Eq. (2.3.16). Here, a is a constant characteristic of the materials. The acceleration caused by this term is given by

$$\left(\frac{d\mathbf{v}_i}{dt}\right)_a = 2\frac{a}{m_i^2}\sum_j^N m_j \nabla_i W_{ij} \tag{3.2.1}$$

Figure 3.2.2 shows the analytical results when the effect of Eq. (3.2.1) is included in the calculations for air (*a*=1). In comparison with Fig. 3.2.1, the bubbles broke into two smaller bubbles rather than many finer fragments. In other approaches, Lennard-Jones potential functions and other tools have been used to tie intermolecular potentials (Israelachvili, 1991) with surface tension forces. Models with the greatest promise for general application will be investigated further in the future.

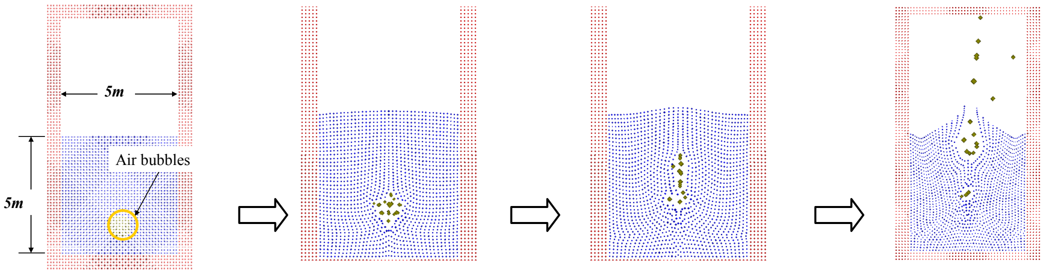

Fig.3.2.1 Analysis of bubbles in water: Effect of zero virtual surface tension (Eq. (3.2.1) not applied)

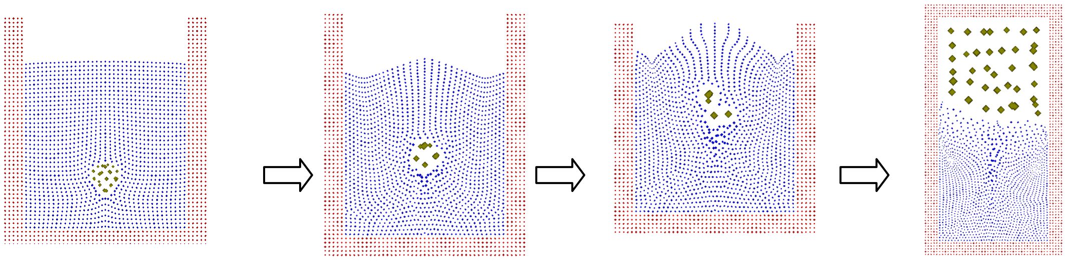

Fig.3.2.2 Analysis of bubble in water, showing the effect of virtual surface tension of water (Eq. (3.2.1) applied)

3.3 Solid-Liquid System (Two-phases)

3.3.1 1D Consolidation of Soil

Figure 3.3.1 presents a comparison between the SPH solution and Terzaghi's theoretical one-dimensional solution (Wood, 2004) for consolidation of a saturated soil (drains on upper and lower surfaces) of thickness *H*. The phenomenon of consolidation in the saturated soil occurs because of excess pore pressure u_e and is described by the following expression:

$$\frac{\partial u_e}{\partial t} = c_v \frac{\partial^2 u_e}{\partial t^2}, \quad c_v = \frac{k}{B_e^{-1} \rho_w g} \tag{3.3.1}$$

where ρ_w and k are the density of water and the coefficient of permeability of the filter, respectively. It is assumed that the initial pore pressure ratio distribution has a sinusoidal shape, with a median value of 1.0. The figure shows curves for the excess pore water pressure ratio at various times as a function of the depth y. The elapsed time t is shown in terms of the time coefficient T_v, a function of parameters of diffusivity:

$$T_v = \frac{k}{B^{e^{-1}} \rho_w g} \frac{t}{H^2} \tag{3.3.2}$$

Here, soil was assumed to be a linear elastic solid with a bulk modulus B^e independent of stress conditions (no fracture was assumed to occur). The results according to SPH conformed well with exact solution by Terzaghi's theory, indicating that this two-phase, soil-water model was appropriate.

3.3.2 2D Peameability Analysis using of some Soil Columns

Figure 3.3.2 shows a peameability analysis. Three geomaterials, only coefficient of permeability is different, were prepared. These coeficients were set to 1.0×10^{-2},1.0×10^{-5} and 1.0×10^{-8} cm/s, respectively. This result shows that the difference of the coefficient of permeability can be reproduced by using SPH. In addition, this method can be also expressed rainfall easily.

3.3.3 2D Solid-Liquid Analysis with Suction in the Box

Figure 3.3.3 shows effect of suction. There are two soil boxes with a little water. One has suction, and another has not the effect of suction. As shown in Fig. 3.3.3, height of water surface of the case to have suction effect is higher than the non-suction case. Thus, the suction effect can be easily expressed by using proposed method.

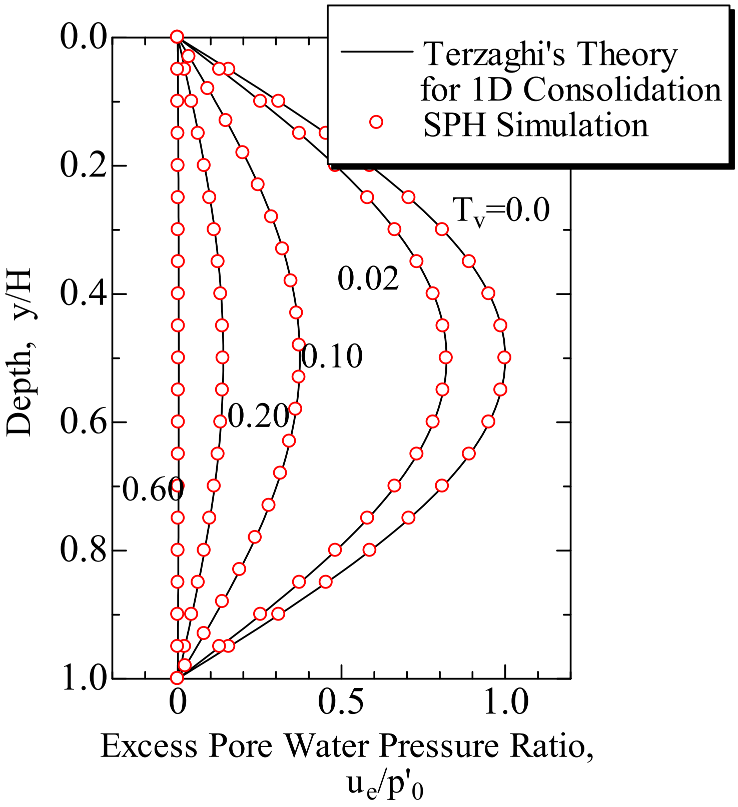

Fig.3.3.1 One-dimensional simultaneous excess pore pressure ratios. Comparison of SPH results with Terzaghi predictions. Drain at upper and lower surfaces, sinusoidal initial pressure distribution

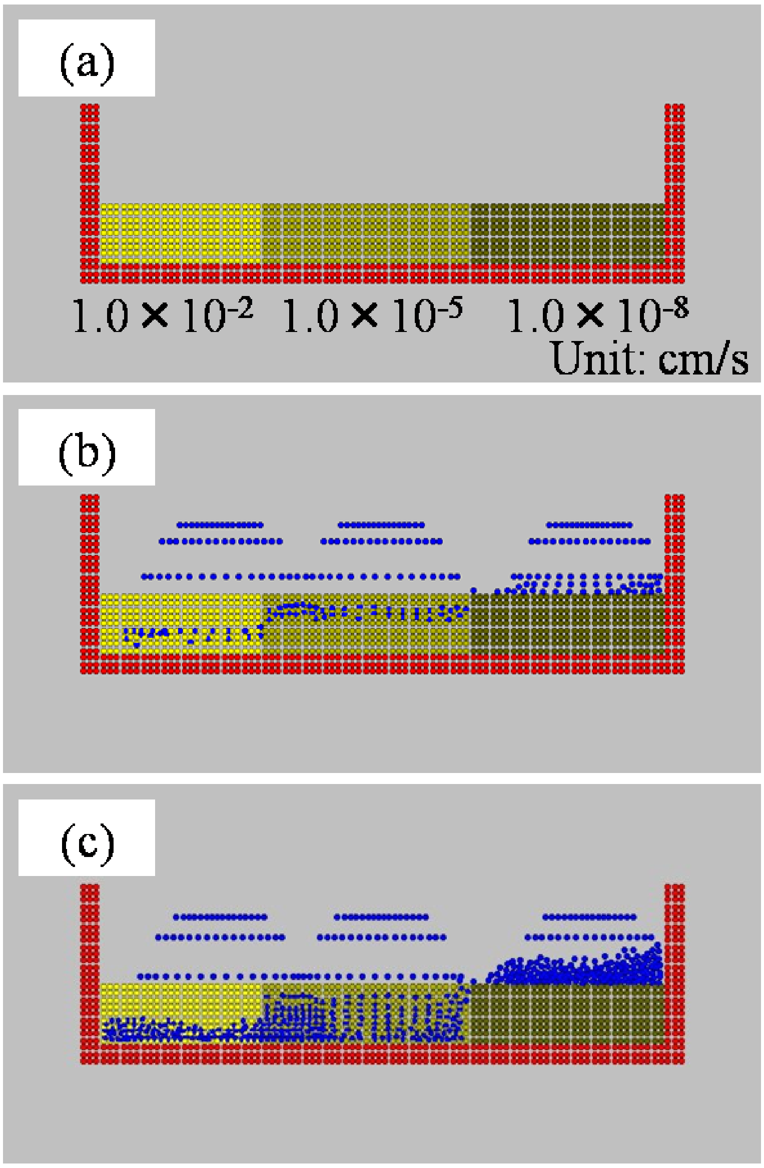

Fig.3.3.2　Permeability analysis of soil columns due to rainfall; coefficients of permeability are 1.0×10^{-2}, 1.0×10^{-5} and 1.0×10^{-8} cm/s, respectively

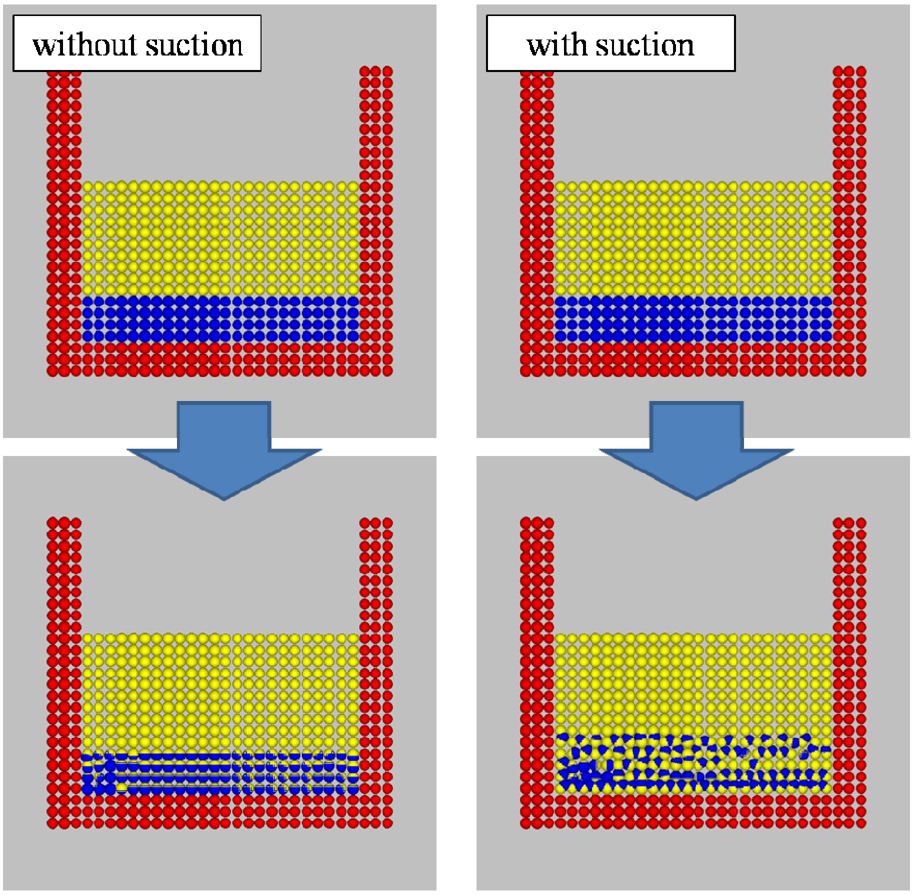

Fig. 3.3.3 Comparison between the case to have suction effect and the case to have not suction effect; left side: without suction, right side: with suction

3.4 Seepage Failure around Sheet Pile Solid-Fluid System (Two-phases and Three-phases)

3.4.1 Soil-Water System (Two-phases)

Figure 3.4.1 shows an SPH model of the experiment shown in Fig. 1.1.1. The yellow particles are the sand base. As occurred in Fig. 1.1.1, the base near the sheet pile deformed, followed by flow and failure of the base. This model thus reproduced characteristics of seepage failure well. In addition, the value of height difference at failure analyzed is almost same as that obtained in the experience.

Figures 3.4.2 and 3.4.3 show the quantitative comparison of a velocity field and pressure field, respectively about Fig. 3.4.1. At the point of tip of the sheet pile, maximum velocity values of the experimental result (using PIV analysis) and numerical simulation are both about 0.25 m/s. In addition, pressure field at the same position indicates also quantitatively good agreements (Fig. 3.4.3).

3.4.2 Soil-Water-Gas System (Three-phases)

Fig. 3.4.4 shows an SPH prediction of seepage failure around sheet pile with air bubbles, where the air bubbles (green dots) are forced to be placed around the sheet pile at initial state in Fig. 3.4.1. In this case, the water column height difference is 60% of that in the case shown in the Fig. 3.4.1. Even under lower height difference, the failure of ground is induced by air bubbles rise: This result fits to the experimental results (Nakajima, 1985; JGS Technical Committee of mechanism of slope failure and prediction of degree of risk under heavy rains, 2003), indicating that air bubbles induce deformation-failure of ground even under lower height difference.

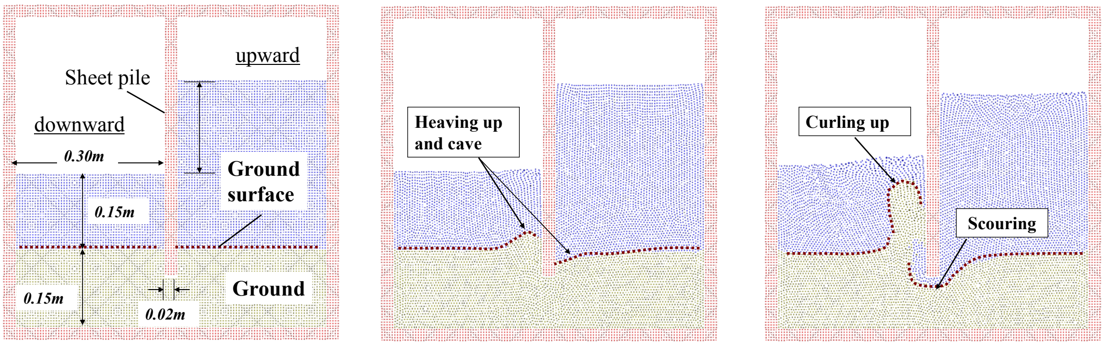

Fig.3.4.1 SPH analysis of seepage failure around sheet pile: flow from right to left

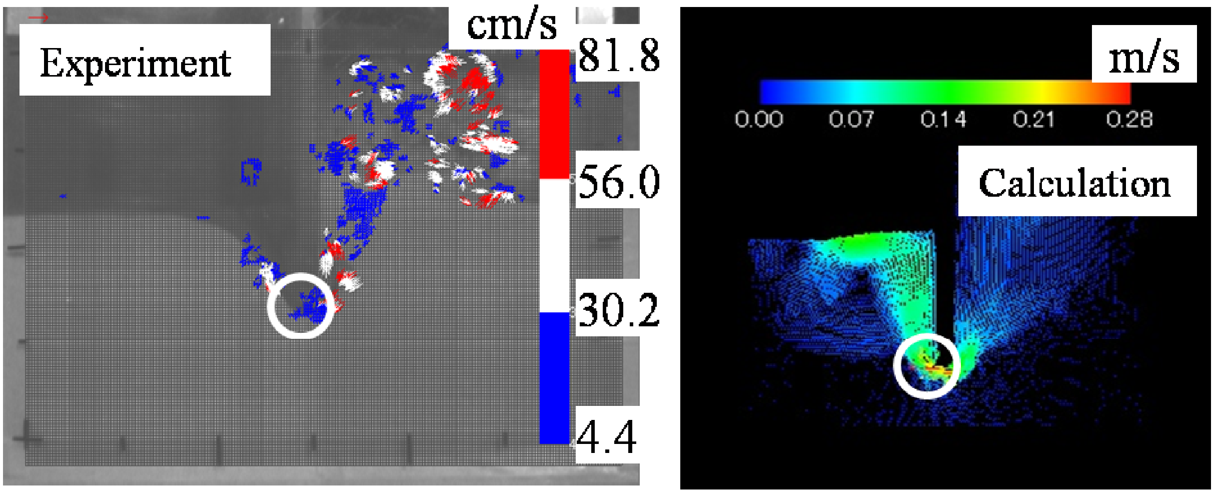

Fig.3.4.2 Comparison of the experimental result and numerical analysis (velocity field)

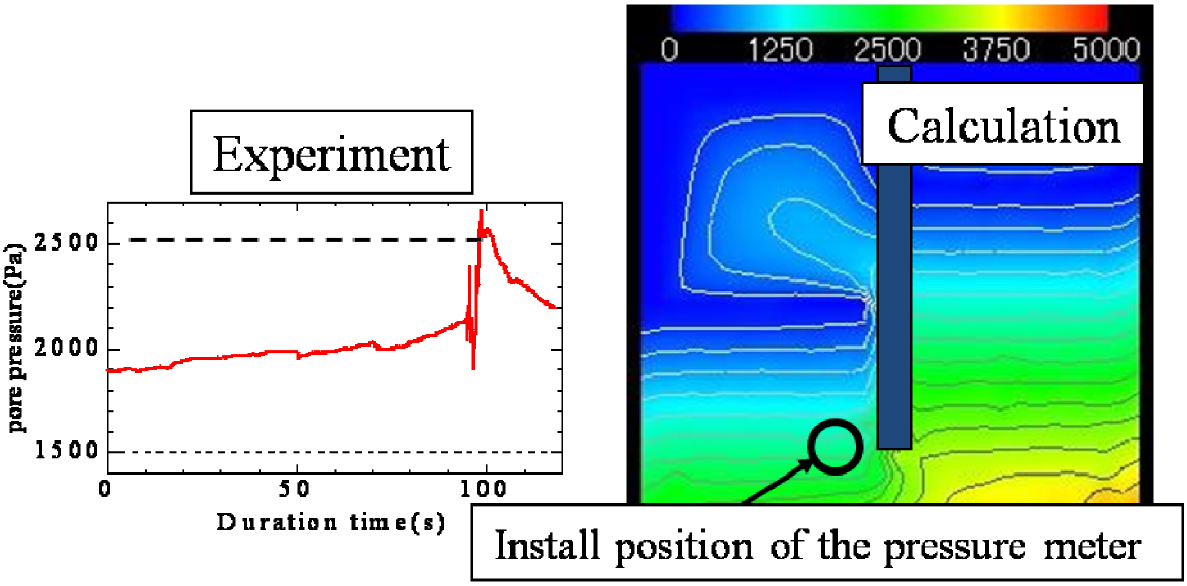

Fig.3.4.3 Comparison of the experimental result and numerical analysis (pressure field)

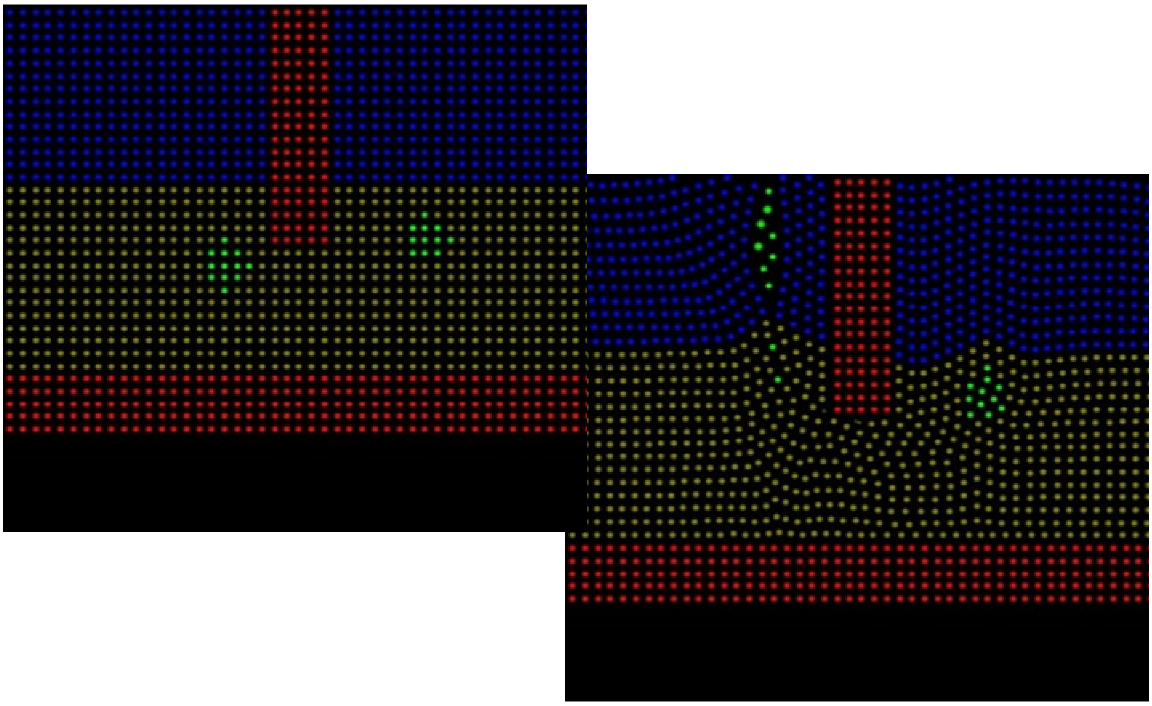

Fig.3.4.4 SPH analysis of seepage failure around sheet pile with air bubbles under the 60% of difference height to the case of Fig. 3.4.1

3.5 Seepage Failure Analysis of Dike Solid-Fluid System (Two-phases and Three-phases)

3.5.1 Appearance of the Progression of Phreatic Line (Two-phases)

Figure 3.5.1 shows the appearance of the progression of a phreatic line. As the water level rises, phreatic line progresses in the dike from right to left. Thus, the observation of the phreatic line of every time can be facilitated by using this method.

3.5.2 Analysis of Seepage Failure of Saturated Dike (Two-phases)

SPH analysis was then used to examine the situation of dike seepage and failure. The parameters were those used in section 3.2.4. The figure shows the case when the rate of water level rise on the exterior side of the dike was higher than on the interior side.

The case of the dike being saturated at the time of water level rise is shown in Fig. 3.5.2. The figure shows the velocity vectors of soil particle transport. Sliding collapse accompanying flowage deformation due to seepage was successfully reproduced by this model. The tendency for initiation of collapse at the toe of the inner side of the dike and continuous progression upward to the crest, as seen in the tank model, was also apparent in the SPH model.

Figure 3.5.3 depicts the events for a dry dike. The figure shows seepage lines (interface between water and air) as dashed lines. As seen in the tank experiment, these lines bowed downward as they developed. It was thus found that the SPH model successfully reproduced the different behaviors of seepage lines under differing dike saturation levels. Therefore, it appears that the SPH method is capable of qualitatively reproducing seepage failure phenomena in dikes.

3.5.3 Comparison between Prototype Dike Experiment and Numerical Simulation with account for Air Bubbles (Three-phases)

Figures 3.5.4 and 3.5.5 shows the comparison between prototype dike experiment and numerical simulation with suction effect. In case of without rainfall (Fig. 3.5.4), progress speed of phreatic line calculated from numerical analysis is faster than the prototype experiment result. The reason is that simulated air bubbles were blown out rapidly due to non-rainfall.

As shown in Fig. 3.5.5 (with rainfall), phreatic lines of prototype experiment is very complicated due to rainfall. But in the numerical simulation, behaviors of these phreatic lines were able to reproduce qualitatively. So, it says that proposed method can simulate three-phase analysis.

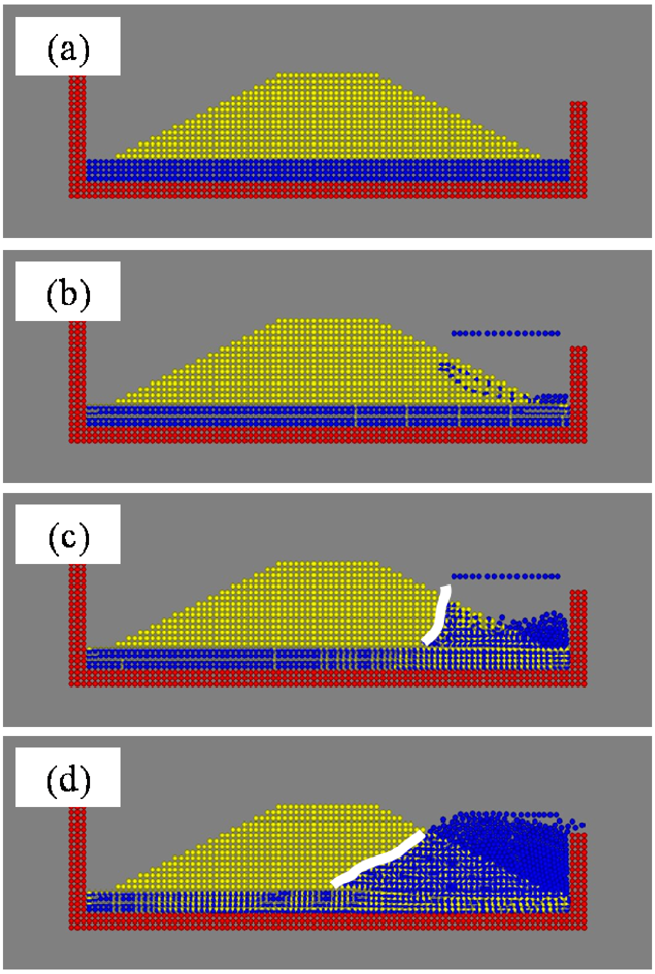

Fig.3.5.1 Appearance of the progression of phreatic line

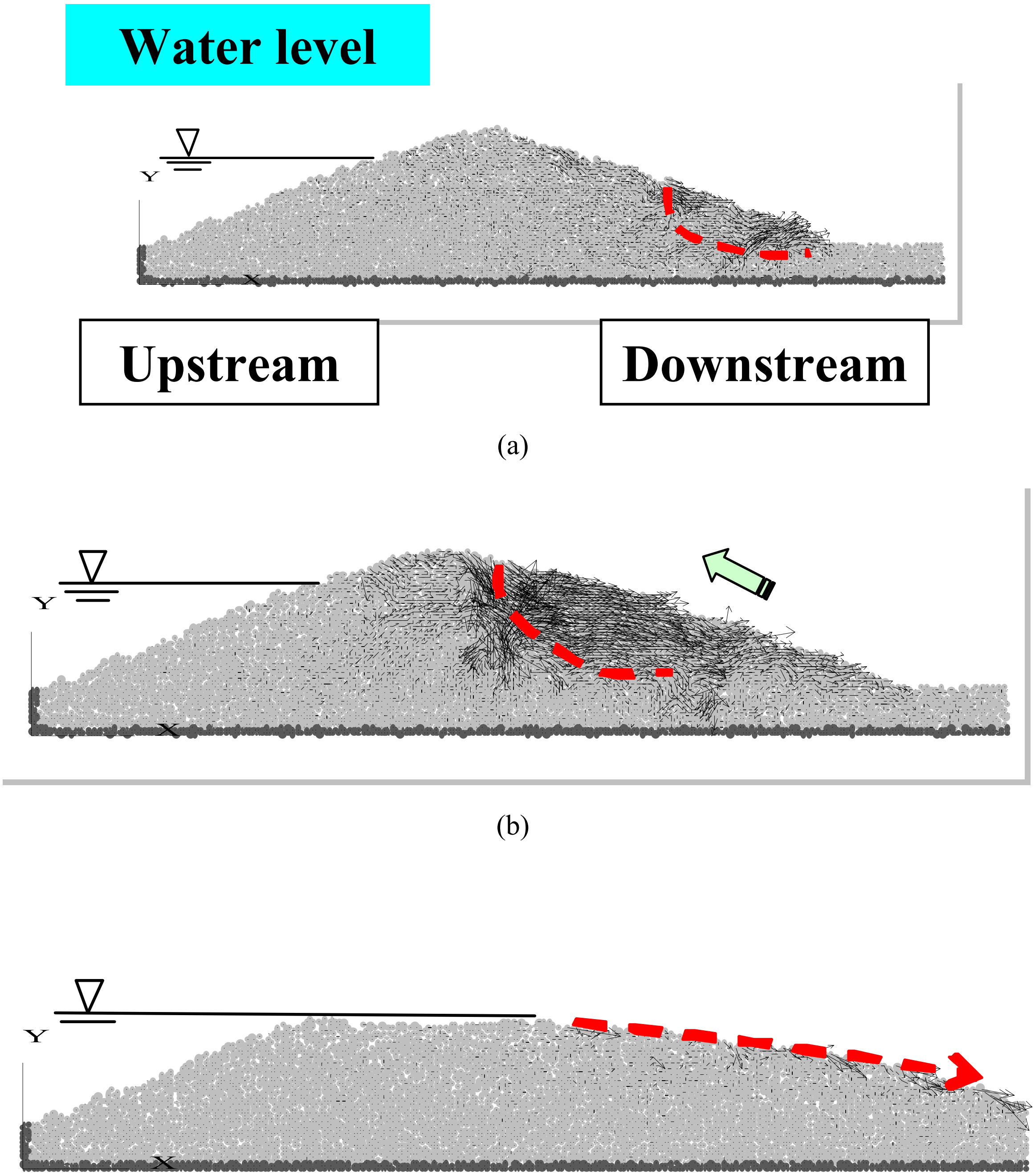

(a)

(b)

(c)

Fig.3.5.2 Analysis of seepage failure of saturated dike; (a) sliding collapse of dike toe (b) propagation of collapse up dike (c) overflow (a black arrow show vector of a SPH particle velocity)

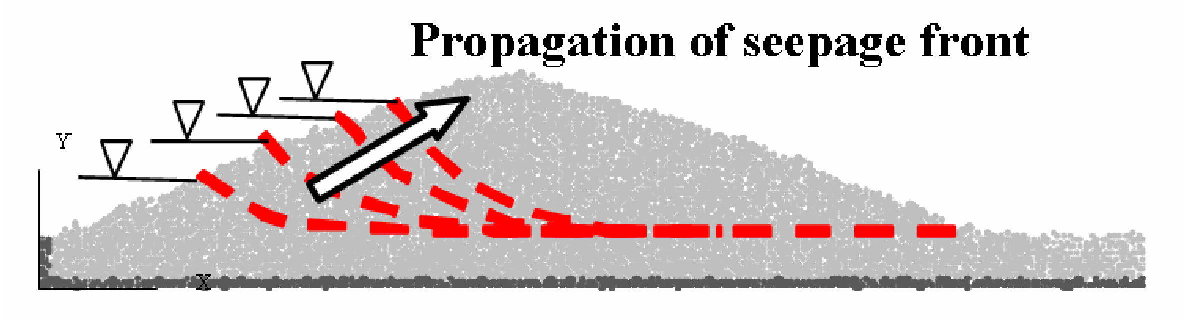

Fig.3.5.3 Analysis of seepage process in dry dike

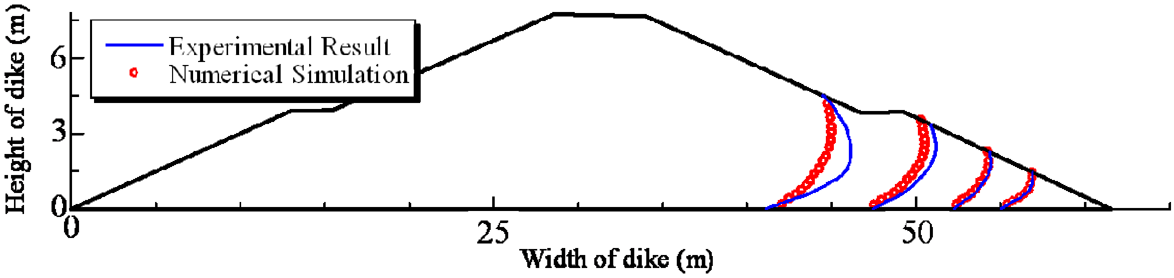

Fig. 3.5.4 Comparison between a result of prototype dike experiment and numerical simulation with account for air bubble (without rainfall); the infiltration velocity of the numerical simulation is faster than the experimental result

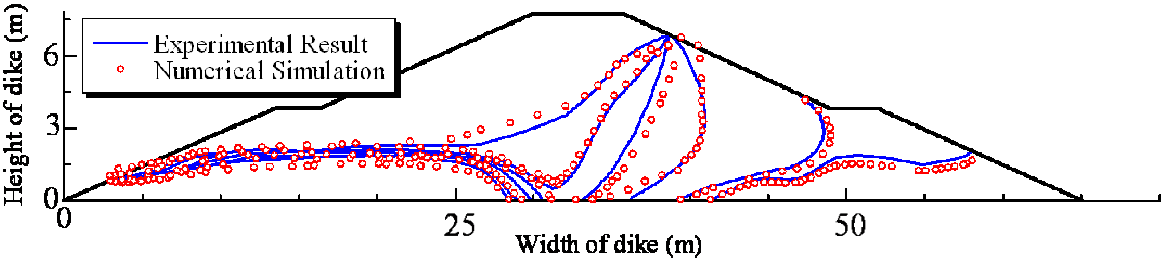

Fig. 3.5.5 Comparison between a result of prototype dike experiment and numerical simulation with account for air bubble (with rainfall); the infiltration velocity of the numerical simulation is slower than the experimental result in early stage

3.6 Summary

In this part, we proposed numerical analysis method using Smoothed Particle Hydrodynamics with account for air bubble. The results obtained in this study can be summarized as follows:

(1) The improvement of density allows the densities of the different materials to be calculated with high precision everywhere, including the vicinity of phase interfaces. Investigations into approaches to the accurate and simple calculation of density will be continued for cases of changes in system mass, and in cases involving more abrupt, discontinuous changes in density.

(2) In addition, we improved the interaction between solid and liquid layers, surface tension, and boundary conditions.

(3) As shown in single-phase analysis, proposed method has both qualitatively and quantitatively good agreement. In addition, in case of seepage failure analysis (two-phases), it has also good agreements compared with the experimental results.

(4) In case of three-phase dike analysis, the influence of the bubble due to rainfall was able to be reproduced qualitatively.

(5) Through the SPH analysis, it is understood that two countermeasures have enough effect. One is the installation of the hole to remove air bubbles in a dike. And another is the installation of the seepage control sheet with high permeability against air

PART 4

Suggestion of Countermeasure Method against Rainfall and Overflow of Dike with account for Air Bubble

Chapter　1

Outline of the Suggestion

In PART 1, the influence of air bubble in the seepage failure phenomenon was considered, and it was shown that bubble dynamics, that is generation, development and blow, causes seepage failure of the ground. In PART 2, it was observed that air bubble in the dike is caught by the rainfall. And finally, the bubble is blown out from the dike by the increment of the water level. In addition, strength of the dike including air bubble is decreased as well as PART 1. In PART 3, there was a new attempt to develop the procedure by Smoothed Particle Hydrodynamics with account for the interaction among three phases: solid, liquid and gas.

Therefore, in this part, we propose some reinforcement methods against the influence of air bubble, rainfall and overflow. And these effects of the reinforcement are verified by both experimental approach and analytical approach.

There are two reinforcement methods as follows:

(1) Installation of the hole to remove air bubbles in a dike (Fig. 1.1); existence of air bubble in a dike gives dike negatively affect. So, we propose installation of the hole to remove air bubbles in the dike. Actually, many old deversoirs in Japan (ex. Watarase Yusuichi in Japan,

Otai Yusuichi in Japan) have already installed these holes in the dike. So, it is thought that the effect can be expected by giving such measures to the river dike, too.

(2) Installation of the seepage control sheet with high permeability against air (Fig. 1.2); as we know, dike is weak to external erosion by the overflow or rainfall. In addition, rainfall becomes a factor to capture air bubbles in the dike. So, it is thought that the effect can be expected protecting surface of dike by using material, which is not easy to through water and through air easily.

First, the effect of the reinforcement of the seepage control sheet is verified by experimental approach. In this part, effect of the seepage control sheet is compared with the sheet that has impermeability against both air and water (this means the reinforcement like asphalt facing of the dike). And then, the effect of seepage control sheet that has different setting position is examined.

Next, effects of two reinforcements are verified by analytical approach using Smoothed Particle Hydrodynamics. In this approach, there are two patterns to examine; one is the installation of the hole in the dike from the center of the dike to the crest, another is the installation of the seepage control sheet whole of the dike.

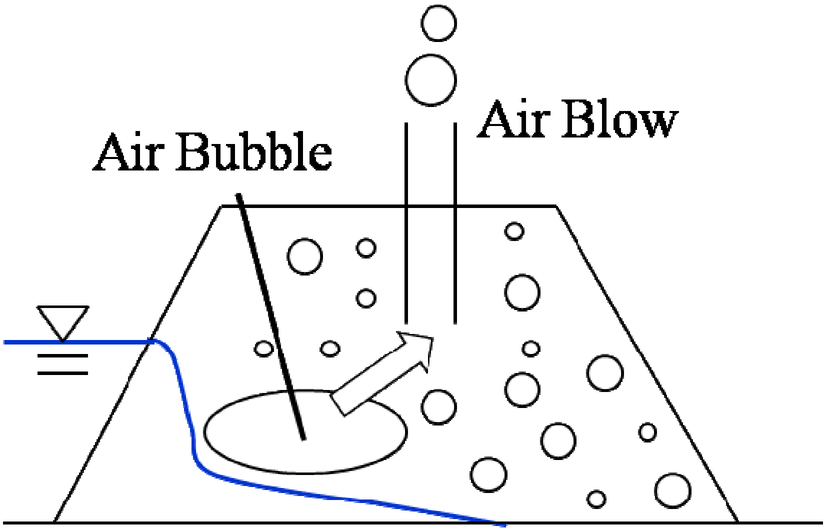

Fig.1.1 Installation of the hole to remove air bubbles in a dike (Image)

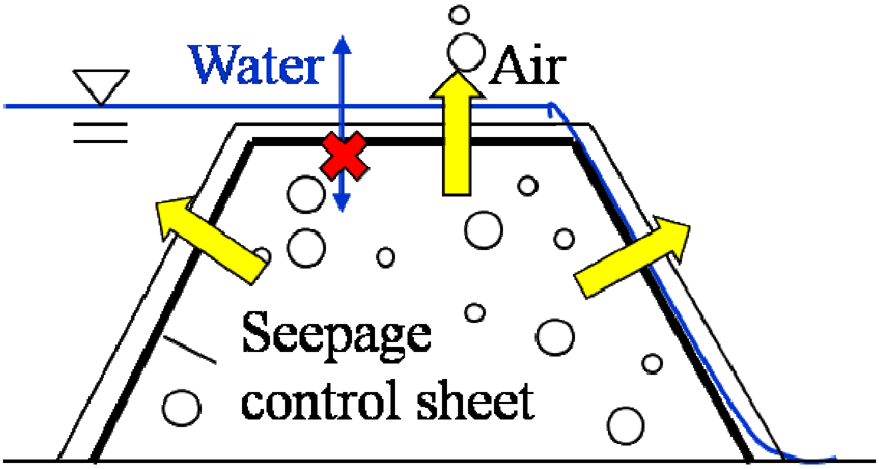

Fig.1.2 Installation of the seepage control sheet with high permeability against air (Image)

Chapter 2

Experimental and Analytical Conditions

2.1 Experimental Condition

Figure 2.1.1, Table 2.1.1 and Fig. 2.1.2 show the photograph of a seepage control sheet which is made by Taiyo Kogyo Corporation, experimental conditions, and experimental apparatus including the setting position of the sheet, respectively. When the sheet is set up in the slope surface of the prototype dike, there is a possibility to damage the sheet by the influence of the wind, rainfall or sunlight. So it is thought that the sheet setting position needs some overburdens. Therefore, in this experiment, the sheet was set up from the surface of the dike to the depth of 50 mm. Toyoura sand was used, and DO value of tap water was controlled supersaturation state by a thermo regulator, air generator and heater. As the countermeasure method, the presence of the rainfall is considered.

First, effect of the seepage control sheet is compared with the sheet that has impermeability against both air and water.

Case (1): In the case of impermeability sheet against air and water; whole of the dike

Next, the effect of seepage control sheet that has different setting position is examined.

The sheet setting position has three cases as follows:

Case (2a): upstream side including the crest of the dike
Case (2b): downstream side including the crest of the dike
Case (2c): whole of the dike

Through these experiments, the appearance of phreatic lines and residual height of the dike caused by the overflow were examined.

Fig. 2.1.1 Seepage control sheet with high permeability against air

Table 2.1.1 Experimental condition

Case	Kind of the sheet	Sheet Setting Position	Rainfall time
(1)	impermeability sheet against air and water	Whole	45 min. (to the end)
(2a)	Seepage control sheet	Upstream side	45 min.
(2b)		Downstream side	45 min.
(2c)		Whole	45 min.

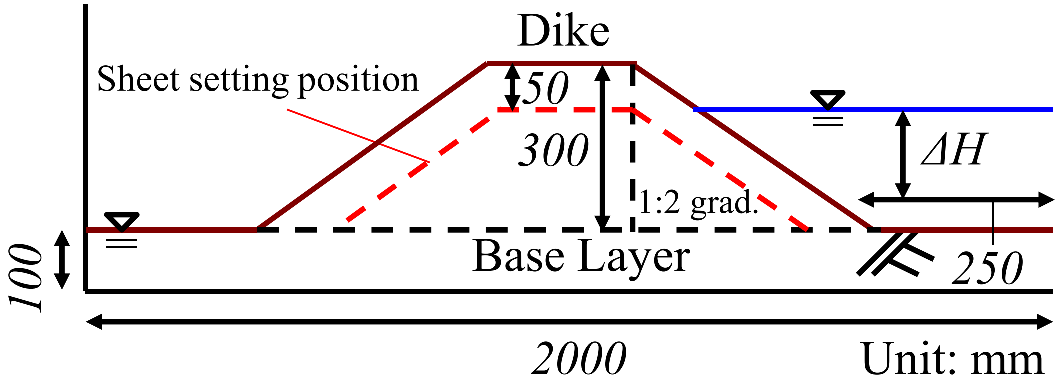

Fig. 2.1.2 Sheet setting position

2.2 Analytical Condition

The analytical scale is the same as the experimental scale, and it took the rainfall into consideration. There are two cases as the countermeasure method as follows:

(1) In the case of setting the seepage control sheet whole of the dike (see sec. 2.1)

(2) In the case of setting the hole in the center of the dike to remove air bubbles

Parameters of each material were the same as analysis in PART 3. The coefficient of permeability and the coefficient of air peameability of the seepage control sheet were 1.0×10^{-8} and 1.0×10^{-3} cm/s, respectively. Here, the sheet was treated as a rigid material, and the hole was set to be able to pass through only the water and air.

Chapter 3

Results and Discussions

3.1 Experimental Results

3.1.1 Case(1): In the case of impermeability sheet against air and water; whole of the dike (prerainfall time: 45 minutes, to the end)

Figure 3.1.1(i-ii) show photos of the front part of the dike. From Fig. 3.1.1 (ii), phreatic line in the dike after rainfall shows very complex shape. It is thought that pore air in the dike was compressed by the seepage water, and this air prevented the permeation of water. In the same time, downside slope of the dike was washed out slowly. This means that the surface of impermeability sheet becomes seepage route.

After the overflow, there were a lot of air bubble between the sheet and dike (Fig. 3.1.2). In addition, just before the overflow, the value of water volume content decreased rapidly (Fig. 3.1.3). On the other hand, pressure meter increased in this moment. That is, very compressed air exists in the dike just before overflow. In this experiment, space between the sheet and the soil tank are bonded by the tape. But in the real case, sheet can move freely. So actually, this compressed air uplifts the sheet, and there is a possibility of increasing damage by the overflow.

3.1.2 Case(2a): In the case of setting up on the upstream side, using seepage control sheet (prerainfall time: 45 minutes)

Figure 3.1.4(i-v) show photos of the front part of the dike. Difference of the phreatic line by a prerainfall was not seen by the existence of the sheet. But, when water level on the upstream side was raised, the soil in upper part of the sheet got wet in suction (Fig. 3.1.4(ii)). And the phreatic speed in the dike decreased compare with the case where the sheet didn't exist. When overflow was begun, downstream side of the dike from the toe of the sheet in the crest was washed out by the overflow, and difference of the residual height of the dike after seepage failure was not seen by the existence of the sheet (Fig. 3.1.4(v)). Fig. 3.1.5 shows photos of the downstide slope surface and crest of the dike after failure (the elapsed time is same as Fig. 3.1.4(v)). Whole dike was perfectly washed out by the overflow from the toe in the crest to downstream side, and lower part of the crest was also washed out (Fig. 3.1.5). On the other hand, when the case of overflow continues, water level on the upstream side didn't become the sheet height of the crest or less. In other words, seepage control sheet that was installed on the upstream side has an ability to prevent the external erosion from the upstream side into the dike. This tendency is also expected in the case of impeameability sheet on the upstream side.

Figure 3.1.6 shows some photos of the slope surface on the downstream side (the elapsed time is same as Fig. 3.1.4(iii)). Some points on the downstream side surface were swelled because of air bubble in the dike. These swellings disappeared with the blow out of the bubble after the edge had cracked (Fig. 3.1.5(A2 or B2)). It is thought that these swelling on the toe of slope occurred by air bubble which has a buoyancy.

3.1.3 Case(2b): In the case of setting up on the downstream side, using seepage control sheet (prerainfall time: 45 minutes)

Figure 3.1.7(i-vi) show photos of the front part of the dike. Difference of the phreatic line by a prerainfall was not seen by the existence of the sheet. But the phreatic speed on the upper side of the sheet is faster than the case where the sheet didn’t exist (Fig. 3.1.7(ii)). It is thought that the upper side of the sheet became a stream line by using seepage control sheet. When the water level was raised, a large bubble appeared in the dike in the upstream side: 35 minutes after starting the rainfall (Fig. 3.1.7(iii)). Afterwards, the bubble rose in the dike surface with the rising of the phreatic line (Fig. 3.1.7(iv)), and it reached near the crest: 46 minutes after starting the rainfall (Fig. 3.1.7(v)). The overflow was begun from the water-level raising 54 minutes after, and overflow continued for 10 minutes, but lower side of the dike from the sheet was not washed out (Figs. 3.1.7(vi) and 3.1.8). Therefore, it is thought that seepage failure which is caused by the overflow can be prevented by the sheet on the downstream.

Figure 3.1.9 shows the front of the dike, slope surface on the upstream side and the crest, at the same time of Fig. 3.1.7(v). A sinking of ground could be seen at the top of the bubble, and some cracks were also seen in the border of the crest and slope of the upstream. Therefore, it is thought that setting of the sheet in the crest is needed to prevent these phenomena.

In addition, some swellings were seen on the downsteam side slope surface as well as Case (2a) (Fig. 3.1.10).

3.1.4 Case(2c): In the case of setting up whole of the dike, using seepage control sheet (prerainfall time: 45minutes)

Figure 3.1.11(i-v) show photos of the front part of the dike. Difference of the phreatic line by a prerainfall was not seen by the existence of the sheet, but a large bubble appeared between in the dike on the upsream side and the seepage control sheet 17 minutes after starting the rainfall (Fig. 3.1.11(ii)). Afterwards, the bubble rose in the dike surface with the rising of the phreatic line (Fig. 3.1.11(iii,iv)), and the bubble disappeared 46 minutes after starting the raising the water level (Fig. 3.1.11(v)). It is thought that the bubble was blow out slowly through the seepage control sheet at that time.

Figure 3.1.12 shows the appearance of downstream side slope after overflow. The dike inside of the sheet was perfectly protected from overflow, and the effect of the seepage control sheet against air blow and overflow could be checked. However, it is thought that covering the dike perfectly by using the sheet is inefficiency, when thinking about constraction cost and time in the dike of a real scale.

Figure 3.1.13(a-d) show the difference in the phreatic line of three cases; non-countermeasure case, in case of impermeability sheet, and in case of seepage control sheet. These cases are compared at time that the amount of the water supply becomes equal. Progress of the phreatic line of the non-countermeasure case is faster than other cases. In other words, covering of the sheet that has impermeability of water makes progress of the phreatic line slow.

As shown in Fig. 3.1.13(a), the phreatic line in the case of low permeability sheet is very complex compared with the case of seepage control sheet. And in this case, compared with the case of seepage control sheet, it is understood that the permeation speed becomes slow as time goes by. On the other hand, in the case of the seepage control sheet, it is understood that the permeation speed doesn’t decrease even if time passes. This means air in the dike is smoothly substituted for water by the effect of the air permeable sheet. Therefore, seepage control sheet has the following two advantages; one is able to resist the rainfall and the overflow by delaying permeation in the dike, another is able to prevent the air blow of the dike at the time of overflow, by the substitution for water of air.

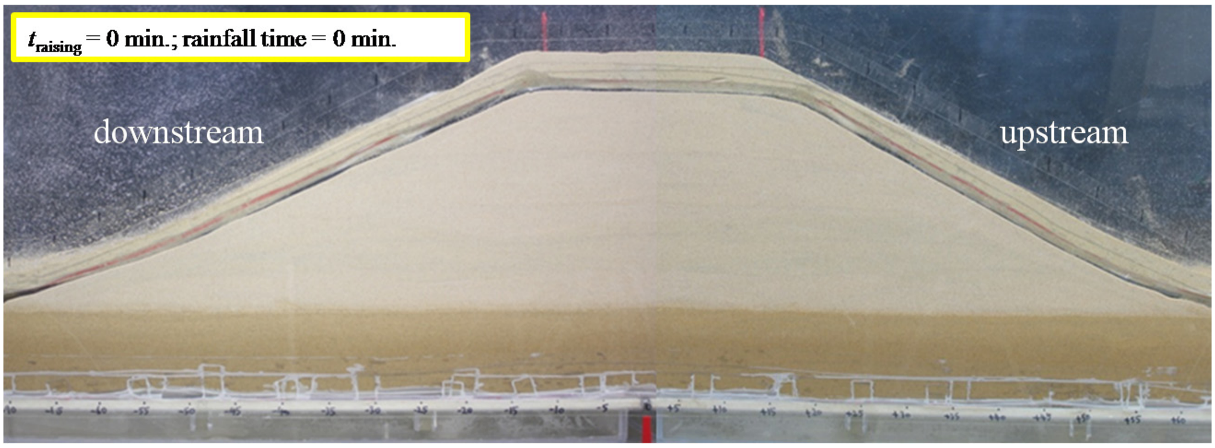

Fig. 3.1.1 (i) Appearance of the seepage front; Case (1), elapsed time of rainfall = 0 min.

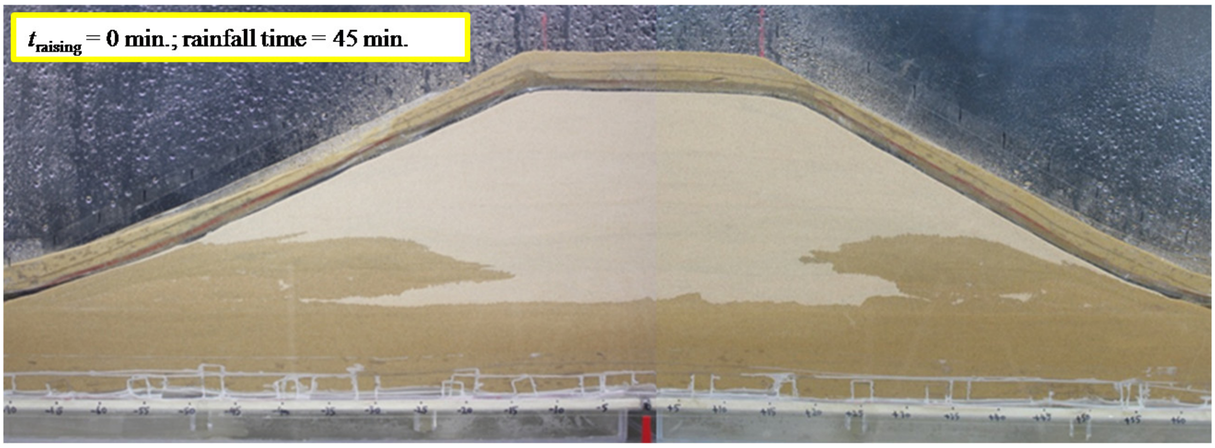

Fig. 3.1.1 (ii) Appearance of the seepage front; Case (1), elapsed time of rainfall = 45 min.

Fig. 3.1.2 Appearance of the downstream side slope after overflow; Case (1)

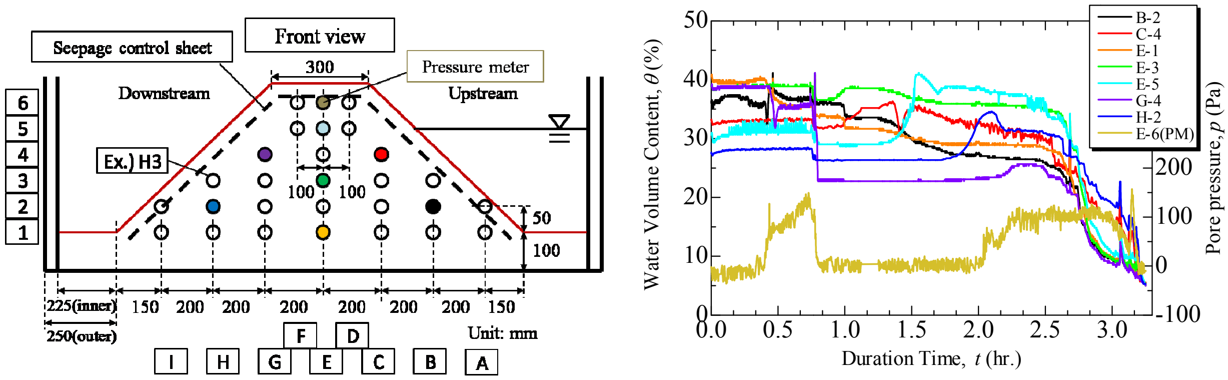

Fig. 3.1.3 Install position of moisture meters and the tensiometer, and changing in the water volume content and pore pressure; Case (1)

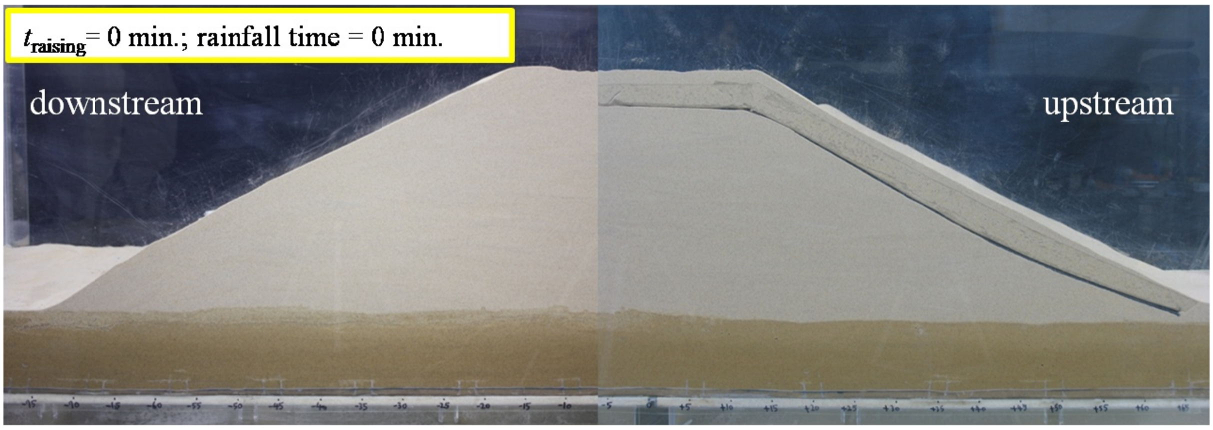

Fig. 3.1.4 (i) Appearance of the seepage front; Case (2a), elapsed time after ending prerainfall = 0 min.

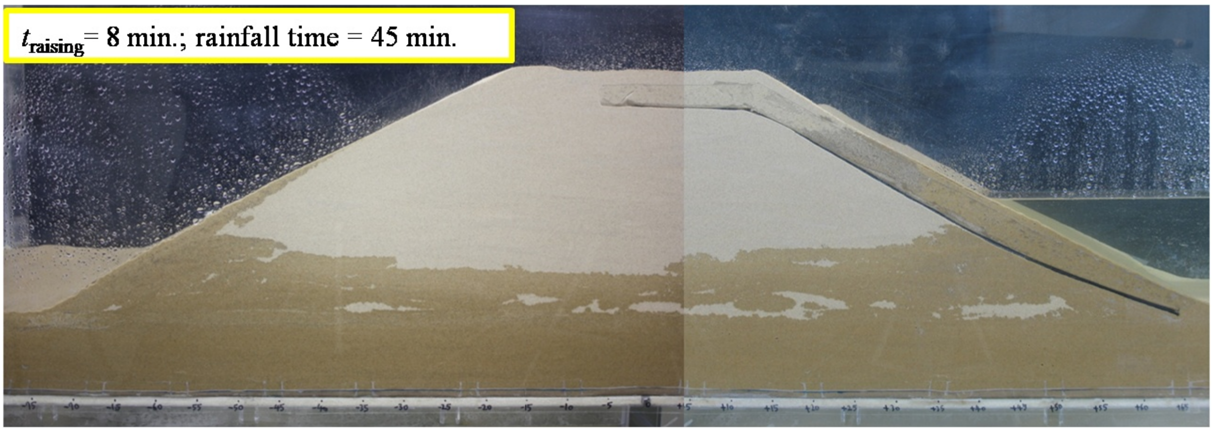

Fig. 3.1.4 (ii) Appearance of the seepage front; Case (2a), elapsed time after ending prerainfall = 8 min.

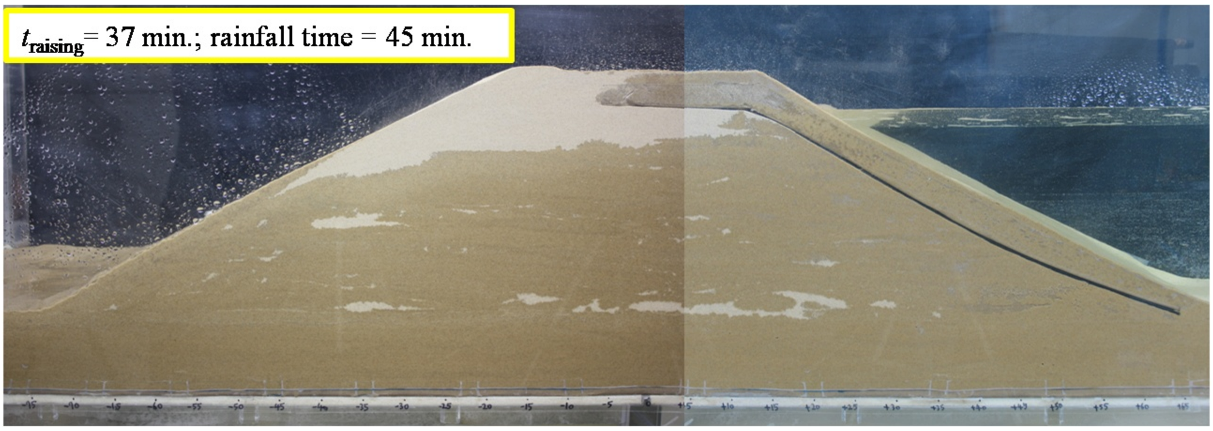

Fig. 3.1.4 (iii) Appearance of the seepage front; Case (2a), elapsed time after ending pre-rainfall = 37 min.

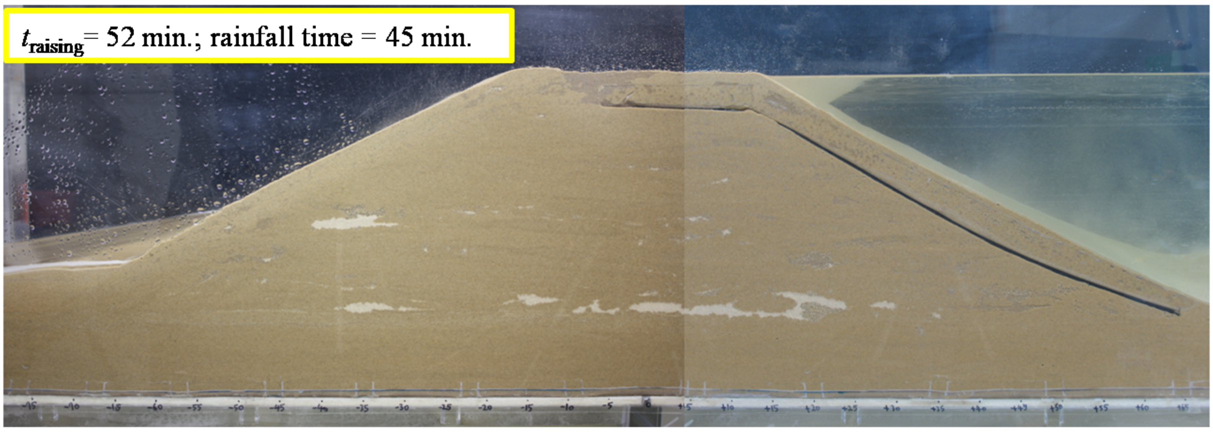

Fig. 3.1.4 (iv) Appearance of the seepage front; Case (2a), elapsed time after ending pre-rainfall = 52 min.

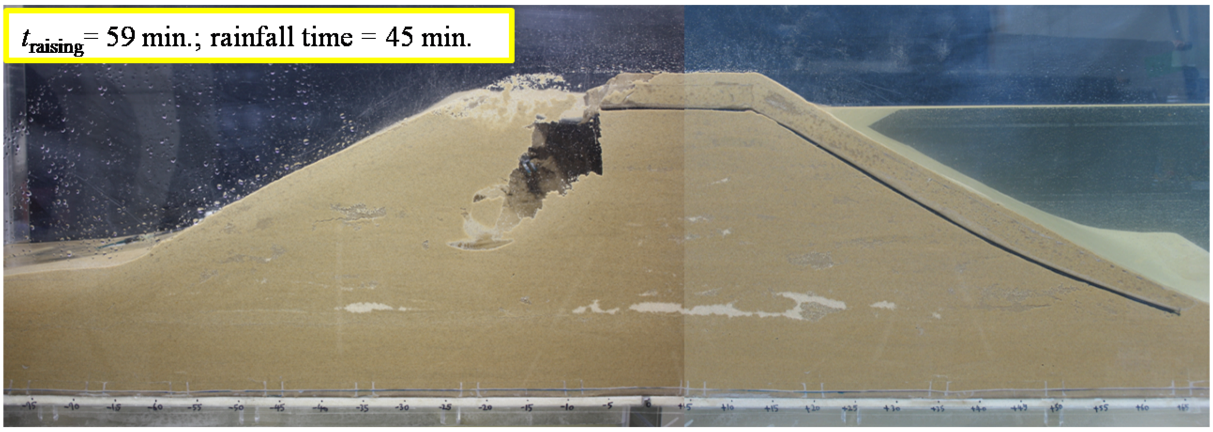

Fig. 3.1.4 (v) Appearance of the seepage front; Case (2a), elapsed time after ending prerainfall = 59 min.

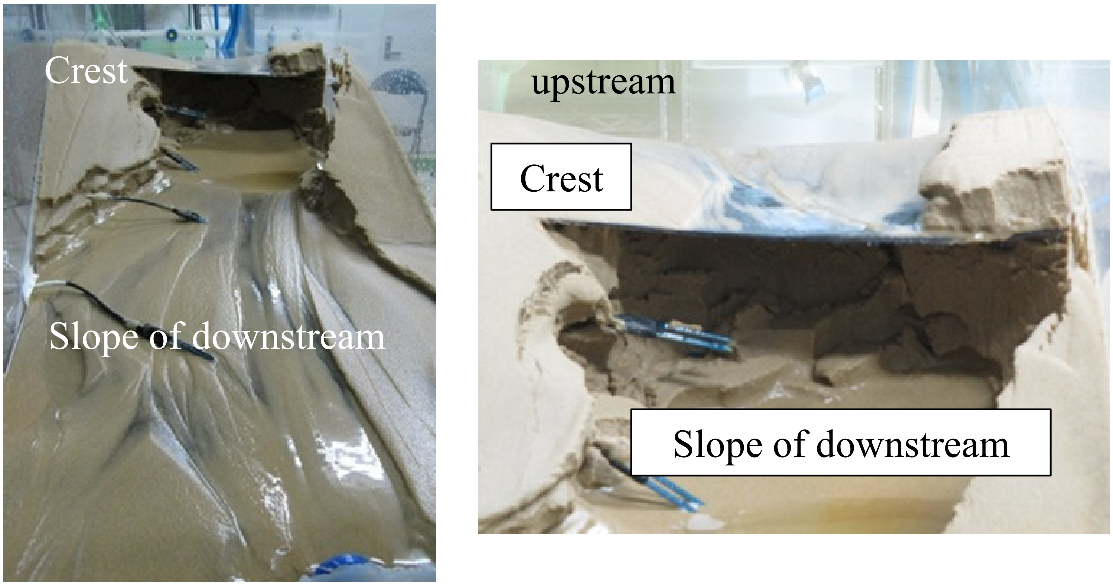

Fig. 3.1.5 Air blows at the downstream side, Case (2a), elapsed time after ending prerainfall = 59 min.

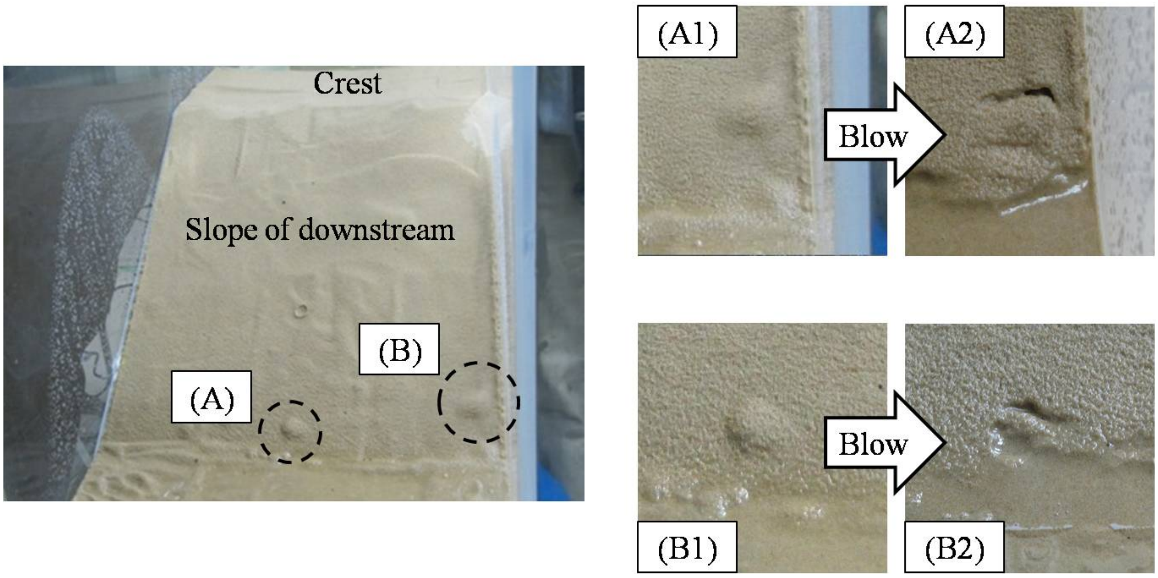

Fig. 3.1.6 Air blows at the downstream side, Case (2a), elapsed time after ending prerainfall = 37 min.

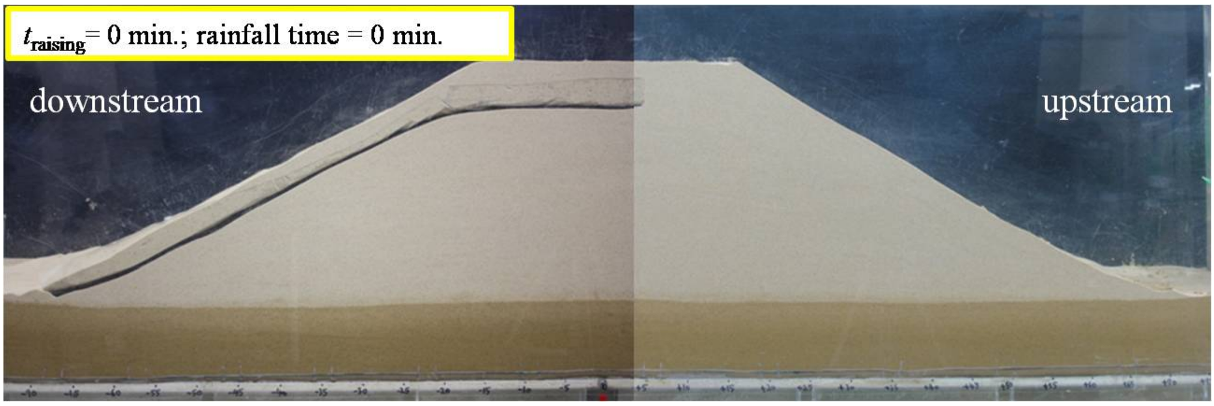

Fig. 3.1.7 (i) Appearance of the seepage front; Case (2b), elapsed time after ending prerainfall = 0 min.

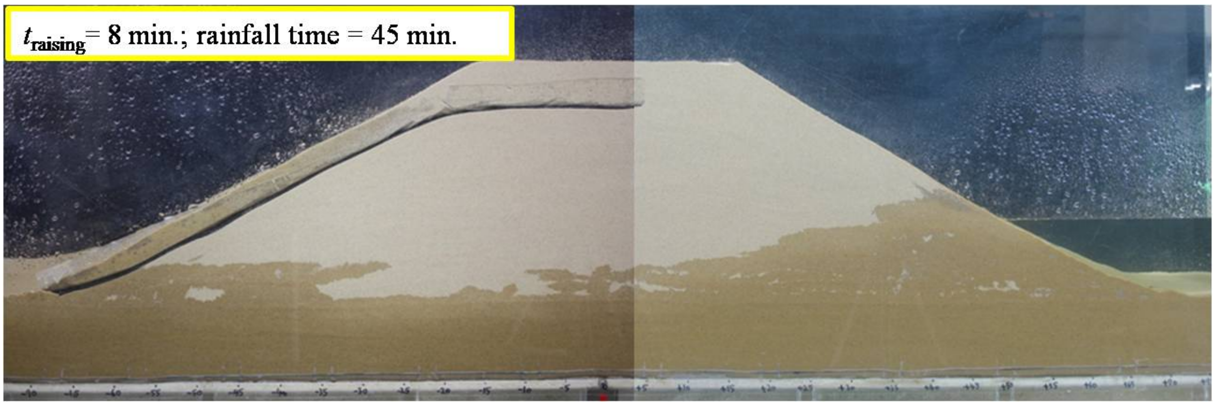

Fig. 3.1.7 (ii) Appearance of the seepage front; Case (2b), elapsed time after ending prerainfall = 8 min.

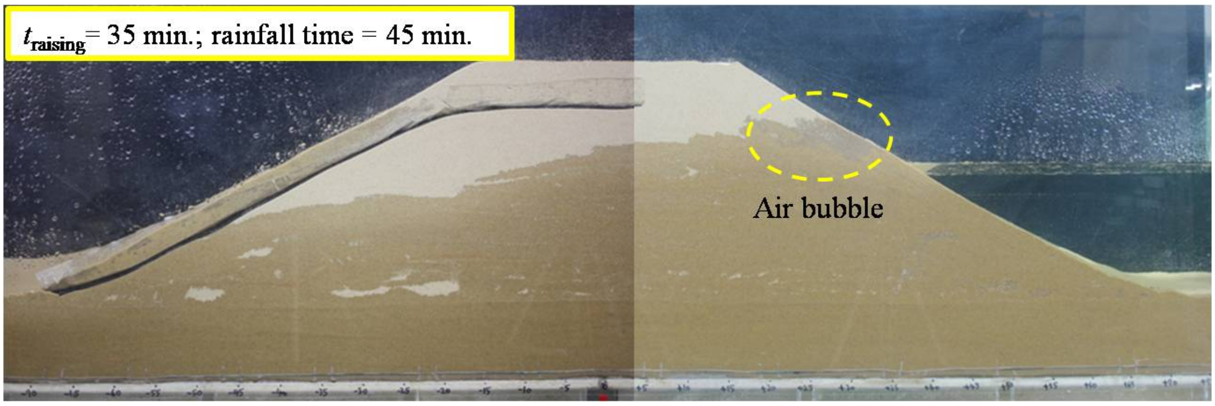

Fig. 3.1.7 (iii) Appearance of the seepage front; Case (2b), elapsed time after ending prerainfall = 35 min.

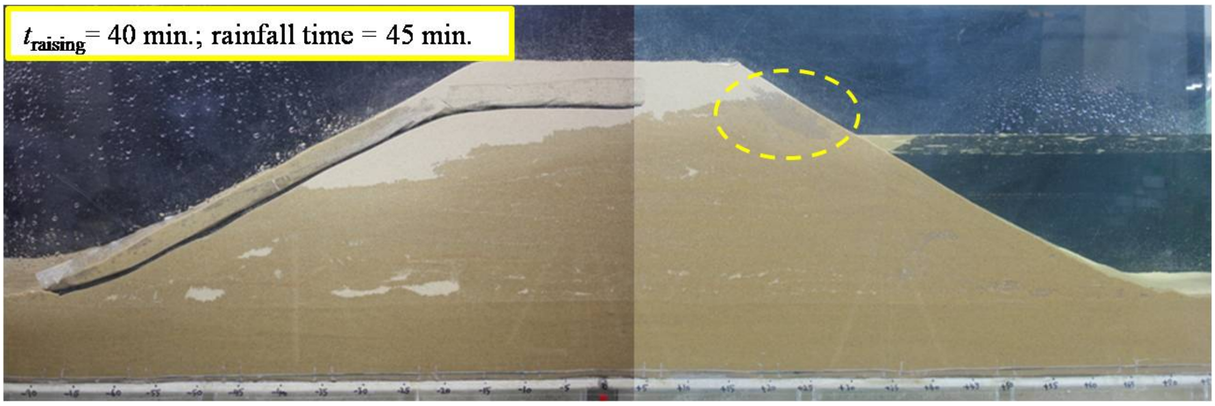

Fig. 3.1.7 (iv) Appearance of the seepage front; Case (2b), elapsed time after ending pre-rainfall = 40 min.

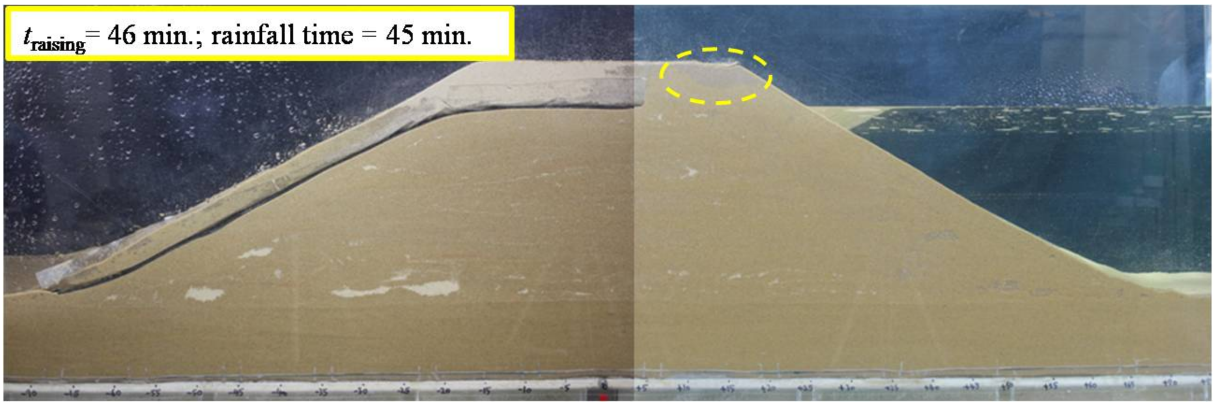

Fig. 3.1.7 (v) Appearance of the seepage front; Case (2b), elapsed time after ending pre-rainfall = 46 min.

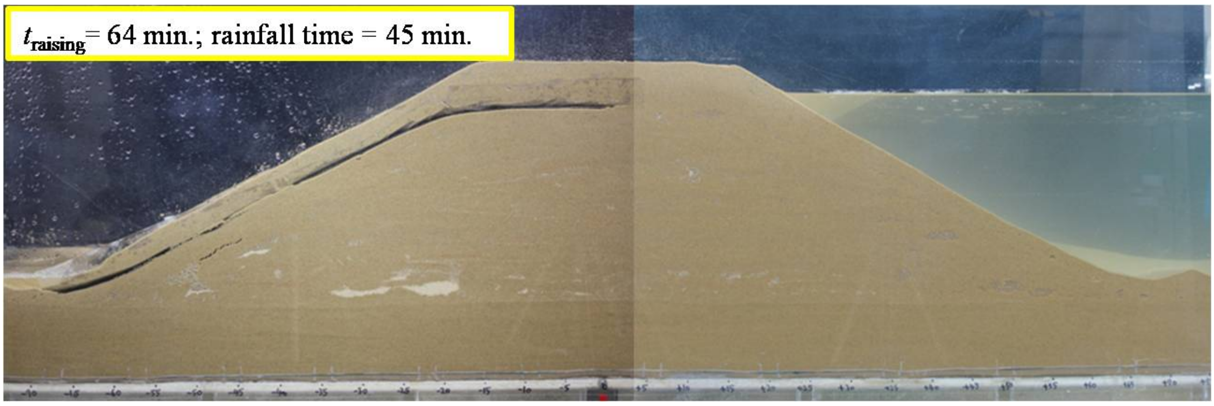

Fig. 3.1.7 (vi) Appearance of the seepage front; Case (2b), elapsed time after ending pre-rainfall = 64 min.

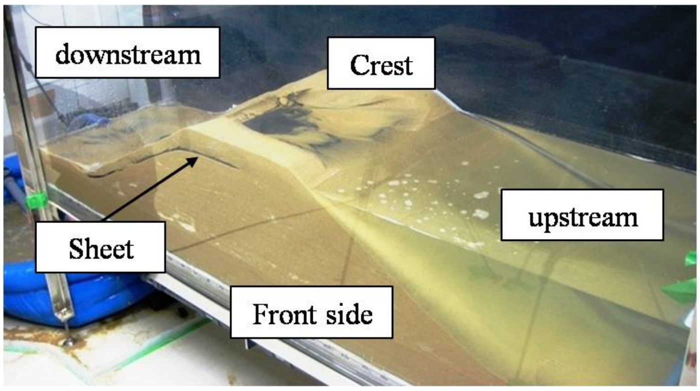

Fig. 3.1.8 Panorama of the dike after failure; Case (2b), elapsed time after ending prerainfall = 64 min.

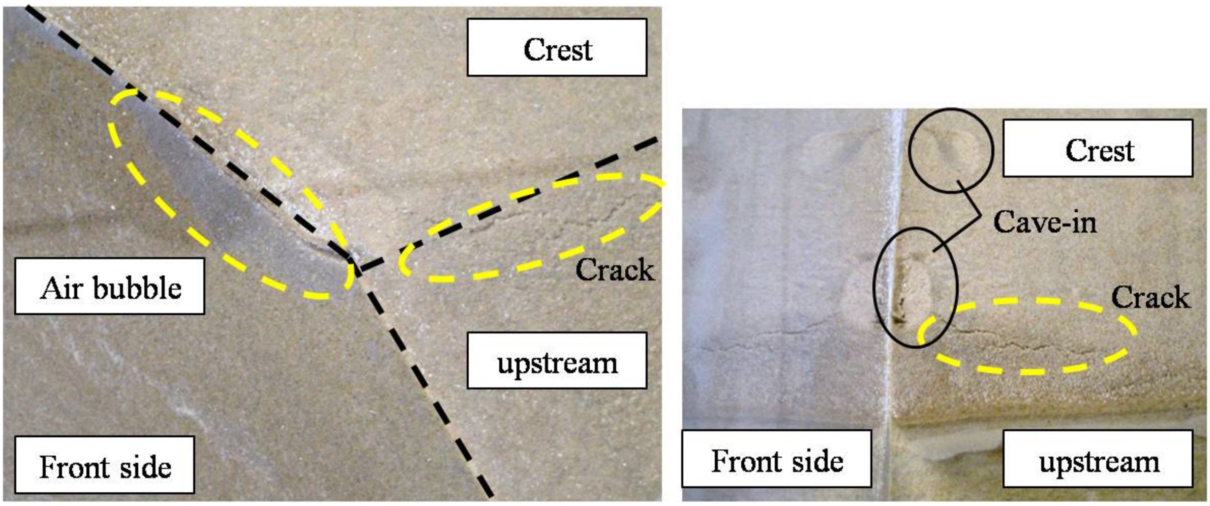

Fig. 3.1.9 Appearance of ground cave-in and crack around the bubble; Case (2b), elapsed time after ending prerainfall = 46 min.

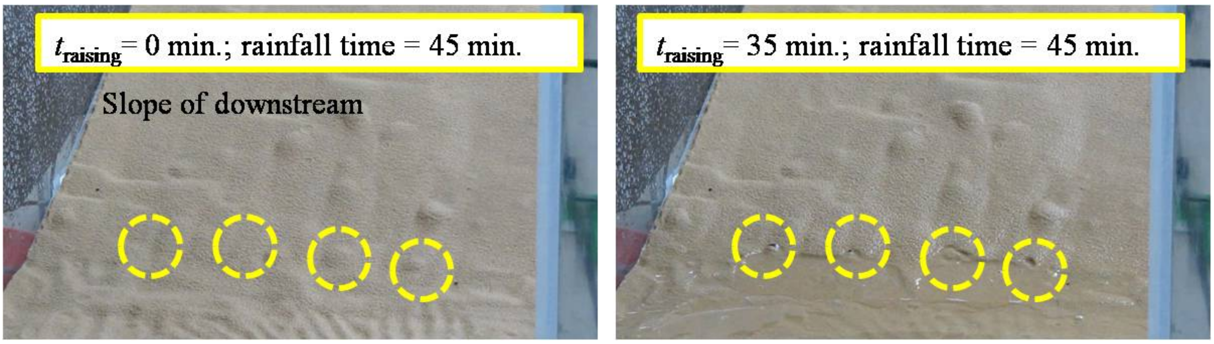

Fig. 3.1.10 Air blows at the downstream side, Case (2b), elapsed time after ending prerainfall = 0 min. (left side) and 35 min. (right side)

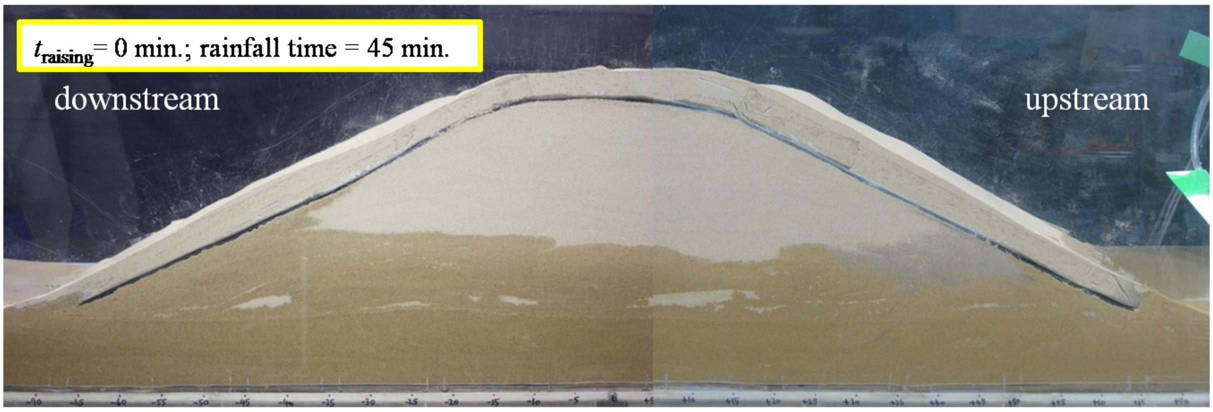

Fig. 3.1.11 (i) Appearance of the seepage front; Case (2c), elapsed time after ending pre-rainfall = 0 min.

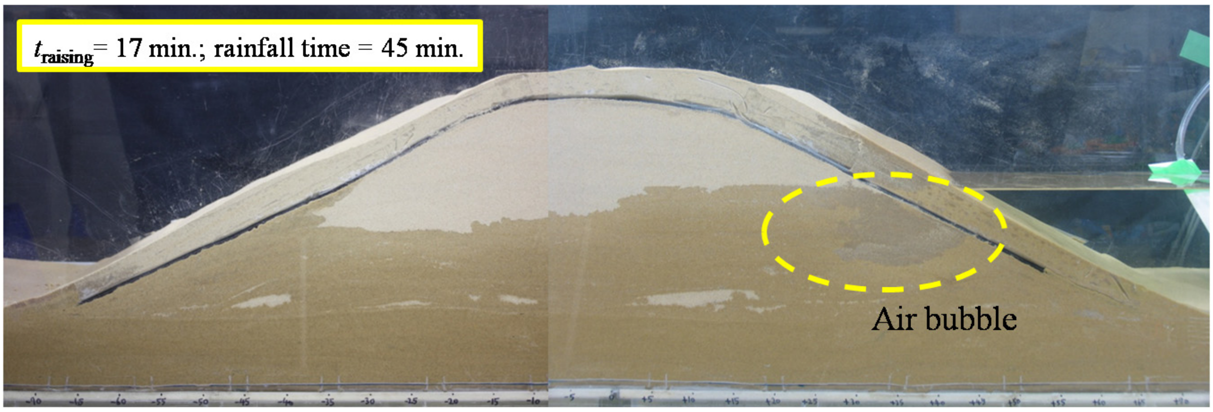

Fig. 3.1.11 (ii) Appearance of the seepage front; Case (2c), elapsed time after ending pre-rainfall = 17 min.

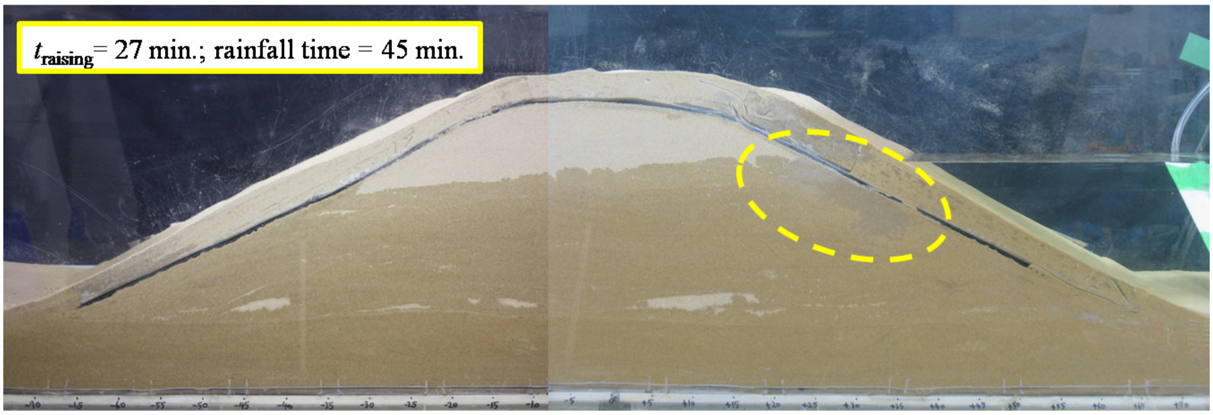

Fig. 3.1.11 (iii) Appearance of the seepage front; Case (2c), elapsed time after ending pre-rainfall = 27 min.

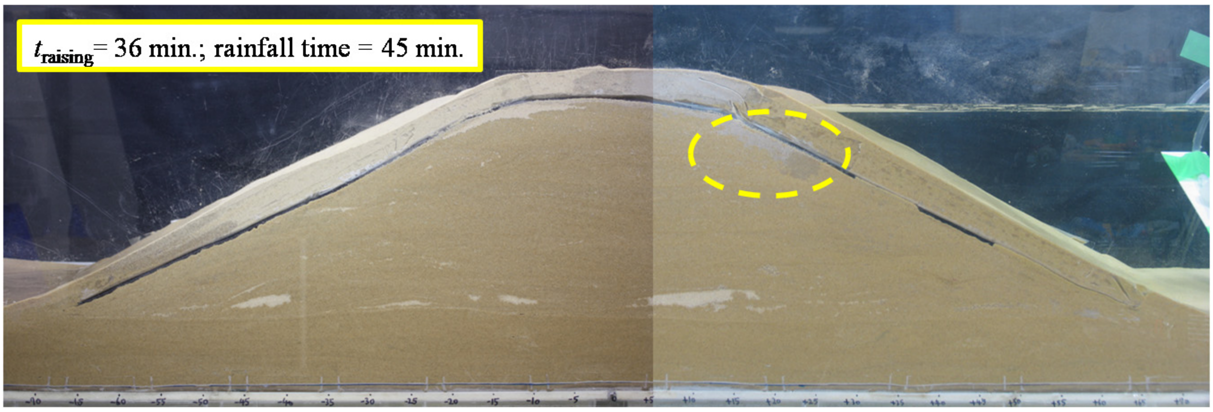

Fig. 3.1.11 (iv) Appearance of the seepage front; Case (2c), elapsed time after ending pre-rainfall = 36 min.

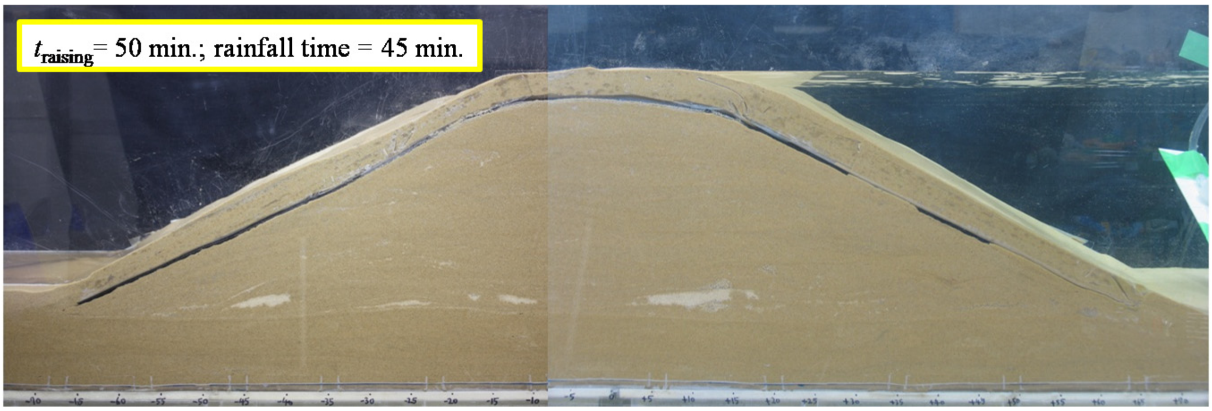

Fig. 3.1.11 (v) Appearance of the seepage front; Case (2c), elapsed time after ending pre-rainfall = 50 min.

Fig. 3.1.12 Appearance of the downstream side slope after overflow; Case (2c)

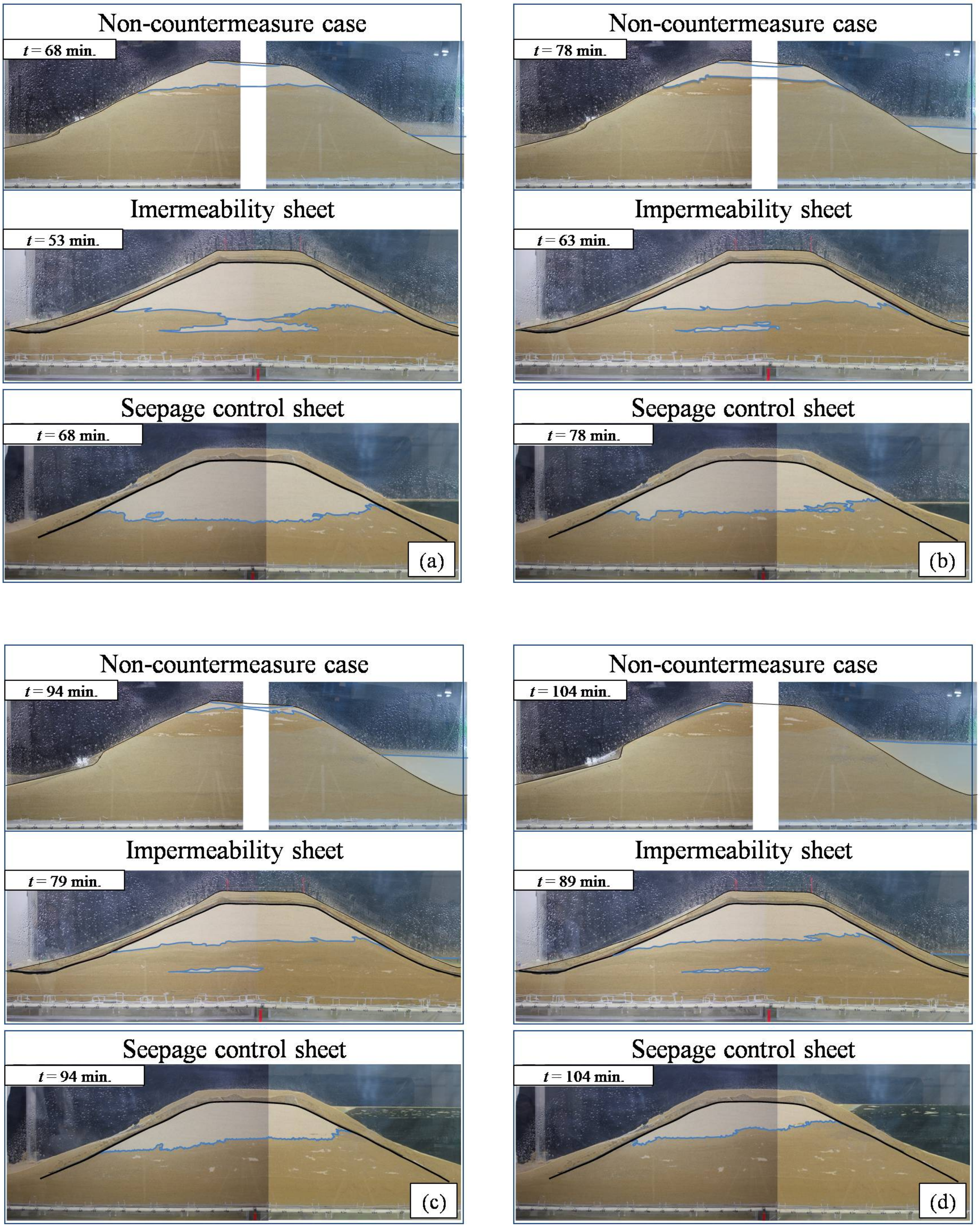

Fig. 3.1.13 Difference in the phreatic line; non-countermeasure case (Case (d), PART 2), in case of impermeability sheet (Case (1), PART 4) and in case of seepage control sheet (Case (2c), PART 4)

3.2 Analytical Results

Table 3.2.1 shows analytical results of residual height, respectively, in the case of non-countermeasure, in the case of installation of the hole to remove air bubbles from the center to the crest of the dike, and in the case of installation of the seepage control sheet with high permeability against air whole of the dike. In the case of non-countermeasure, almost all of dike was washed out by the overflow. In the case of the installation of the hole, loose area in the dike decreses by removing the air, dike became a little stronger than the case of non-countermeasure. In the case of installation of seepage control sheet, it was checked that dike in the sheet was perfectly protected as well as the experimental result as shown in section 3.1.4, PART 4. That is, it says that proposed countermeasure method increases strength of the dike against rainfall and overflow.

Table 3.2.1 Effectiveness of the countermeasure: residual height against overflow (mm); Monotonic raising test with rainfall

Countermeasure method	Residual height (mm)
Without countermeasure	5
Installation of a hole (center)	95
Installation of a seepage control sheet	246

3.3 Summary

In this part, we propose some reinforcement methods against the influence of air bubble, rainfall and overflow. And these effects of the reinforcement are verified by both experimental and analytical approach. The results obtained in this study can be summarized as follows:

(1) Seepage control sheet has the following two advantages, compared with the impermeability sheet. One is able to resist the rainfall and the overflow by delaying permeation in the dike. Another is able to prevent the air blow of the dike at the time of overflow, by the substitution for water of air.

(2) From the result of experimental approach in the case of setting the seepage control sheet in the dike, in spite of the difference of the setting position of the sheet, remarkable difference was not seen in the movement of the phreatic line by a prerainfall. But, when the seepage control sheet exists on the upstream side of the dike, phreatic speed in the dike was slower than the outside of the sheet. When the sheet exists on the downstream side of the dike, appearance of the phreatic line was similar to the case without sheet.

(3) When the sheet was set on the upstream side in the dike, whole dike was perfectly washed out by the overflow from the toe in the crest to downstream side, and lower part of the crest was also washed out. On the other hand, when the case of oveflow continues, water level on the upstream side didn’t become the sheet height of the crest or less. In other words, seepage control sheet that was installed on the upstream side has an ability to prevent the external erosion from the upstream side into the dike. In addition, some points on the downstream side surface were swelled because of air bubble in the dike. These swellings disappeared with the blow out of the bubble after the edge had cracked. It is thought that these swelling on the toe of slope occurred by air bubble which has a buoyancy.

(4) When the sheet was set on the downstream side in the dike, lower side of the dike from the sheet was not washed out by the overflow. Therefore, it is thought that seepage failure which is caused by the overflow can be prevented by the sheet on the downstream. In addition, a sinking of ground could be seen at the top of the bubble. And when water level on the upstream side increases, some cracks were seen in the border of the crest and slope of the upstream. If the seepage control sheet exists on the crest, these phenomena can be prevented. Therefore, it is thought that setting of the sheet in the crest is needed to prevent these phenomena.

(5) When the sheet was set whole of the dike, a large bubble appeared between in the dike on the upsream side and the seepage control sheet. Afterwards, the bubble rose in the dike surface with the rising of the phreatic line, and the bubble disapperared. It is thought that the bubble was blow out slowly through the seepage control sheet. The dike inside of the sheet was perfectly protected from overflow, and the effect of the seepage control sheet against air blow and overflow could be checked. However, it is thought that covering the dike perfectly by using the sheet is inefficiency, when thinking about constraction cost and time in the dike of a real scale.

(6) From the analytical result, proposed countermeasure method, installation of the hole in the dike to remove the air, and installation of the seepage control sheet, increases strength of the dike against rainfall and overflow.

PART 5

Conclusions

Chapter 1

Experimental Study on the Seepage Failure around Sheet Pile of Sandy Ground and Image Analysis by using Particle Image Velocimetry

(1) The monotonic raising test showed that ground surface displacement started at approximately 80% of the critical water-level difference ΔH_{cr}, at which time the ground surfaces on both the upstream and downstream sides of the sheet pile were symmetrically deformed. The amount of ground surface displacement required for seepage failure was greater in dense ground than in loose ground.

(2) In the holding test, ground surface displacement occurred on both the upstream and downstream sides just after maintaining the water-level difference in loose ground. In dense ground, the ground surface displacement did not occur until later, but it progressed rapidly. Ground displacement on the upstream side occurred when air bubbles escaped from the ground on the downstream side. The region of ground displacement gradually propagated upstream the first air bubbles escaped from the ground on the downstream side.

(3) In the re-raising test, seepage failure first occurred at a water-level difference less than the

critical water-level difference ΔH_{cr} (80%–90% of ΔH_{cr}). This means that the ground strength against seepage failure decreased by a maximum of 20% because of air bubbles.

(4) The index of supersaturation I_{ss} (similar to the relative density in geotechnical engineering) allowed the DO values measured during the tests to clearly express the degree of pore water supersaturation.

(5) Contrary to the results reported by Kodaka and Asaoka, air bubble generation was confirmed in the dense ground holding test, even when pore water was undersaturated. Air bubbles were believed to have been generated when during seepage, soil particles forcefully agitated pore water by.

(6) The speed of air bubble development depended on the ground density and I_{ss}. The speed increased as the ground density or I_{ss} increased. In dense ground, the development speed was not greatly affected by I_{ss}. The likely reason for this was that in dense ground, air bubble development was easier than in loose ground because many soil particles held air bubble nuclei and agitation was high. In other words, ground density substantially affected the initial development of air bubbles.

(7) In ground where air bubbles were already generated but had not yet been released, the strength against loading was 1/4–1/5 that of normal ground. The strength of the ground against loading decreased further because of the large quantity of accumulated air bubbles caused by a large overburden.

Chapter 2

Experimental Study on the Seepage Failure of Dike with account for Air Bubble Dynamics and Rainfall

(1) Image analysis of ground displacement around a single air particle showed that an air bubble moved toward the ground surface while expanding and compressing owing to interactions among the bubble, the surrounding ground, and the seepage force. The air bubble would then escape from the ground while forcefully shearing the surrounding ground.

(2) The principles required to explain the life of an air bubble were the Young-Laplace equation, Henry’s law, surface tension, void diameter, air bubble diameter, Boyle’s law, and balance between air bubble buoyancy and the vertical earth pressure above.

(3) A pore water supply was required for air bubble nuclei or generation of fine air bubbles (microbubbles). The development of microbubbles required the incorporation of pore water DO. Air bubbles became visible at the tip of the sheet pile downstream, where the hydraulic gradient i was largest and the static water pressure had begun to decrease. This finding agreed with those of Kodaka and Asaoka.

(4) From air bubble generation to escape, bubble’s shapes changed from slender to globular to flat, and the bubbles gradually moved toward the surface while developing. Just before escaping, the air bubble shapes became slender, and the bubbles sheared the ground above forcefully as they escaped. At this moment, i increased locally and macroscopic seepage failure occurred.

(5) In the period between the holding test start and subsidence of the ground surface on the upstream side, the seepage distance L increased because of ground uplift on the downstream side accompanied by air bubble generation. When the ground upstream side started to subside, the seepage distance L decreased and became shorter than the initial distance in dense ground. The permeable water volume Q exhibited a similar trend. Even though the water-level difference was fixed, i increased as time progressed, and seepage failure also accelerated. In addition, the local deformation width W from the sheet pile was about $D/2$–D of the penetration depth of the sheet pile D in the ground upstream. This was about $D/2$ in the ground downstream, as pointed out by Terzaghi.

Chapter　3

Seepage Failure Analysis Method of Ground with Smoothed Particle Hydrodynamics

(1) Seepage failure occurred when the safety factor was nearly at its smallest value (nearly 1.0 to 1.1, these values are very severe for a dike) in every case. Moreover, in L-1, where seepage failure did not occur, the safety factor did not change substantially. Therefore, ground seepage failure where the water-level difference is fixed is believed to occur because of the synergistic effect of the increase in the hydraulic gradient, a macroscopic process. This is associated with the decrease in the seepage distance and decrease in the critical hydraulic gradient, accompanied by an increase in the quantity of air bubbles, which are microscopic processes.

(2) We clarify the seepage failure mechanism with bubbles Seepage failure of ground containing air bubbles basically occurs because of the decrease in the critical hydraulic gradient i_{cr}, an increase in the void ratio e because of air bubble generation, and the increase in i accompanied by the decrease in L.

(3) To monitoring upstream ground surface displacement is particularly important for

predicting seepage failure. However, since ground deformation is localized, particularly in dense ground, a system that can measure displacement over a wide area or a system that can predict the location of deformation would be required.

Chapter 4

Suggestion of Countermeasure Method against Rainfall and Overflow of Dike with account for Air Bubble

(1) Seepage control sheet has the following two advantages, compared with the impermeability sheet. One is able to resist the rainfall and the overflow by delaying permeation in the dike. Another is able to prevent the air blow of the dike at the time of overflow, by the substitution for water of air.

(2) From the result of experimental approach in the case of setting the seepage control sheet in the dike, in spite of the difference of the setting position of the sheet, remarkable difference was not seen in the movement of the phreatic line by a prerainfall. But, when the seepage control sheet exists on the upstream side of the dike, phreatic speed in the dike was slower than the outside of the sheet. When the sheet exists on the downstream side of the dike, appearance of the phreatic line was similar to the case without sheet.

(3) When the sheet was set on the upstream side in the dike, whole dike was perfectly washed out by the overflow from the toe in the crest to downstream side, and lower part of the crest

was also washed out. On the other hand, when the case of oveflow continues, water level on the upstream side didn't become the sheet height of the crest or less. In other words, seepage control sheet that was installed on the upstream side has an ability to prevent the external erosion from the upstream side into the dike. In addition, some points on the downstream side surface were swelled because of air bubble in the dike. These swellings disappeared with the blow out of the bubble after the edge had cracked. It is thought that these swelling on the toe of slope occurred by air bubble which has a buoyancy.

(4) When the sheet was set on the downstream side in the dike, lower side of the dike from the sheet was not washed out by the overflow. Therefore, it is thought that seepage failure which is caused by the overflow can be prevented by the sheet on the downstream. In addition, a sinking of ground could be seen at the top of the bubble. And when water level on the upstream side increases, some cracks were seen in the border of the crest and slope of the upstream. If the seepage control sheet exists on the crest, these phenomena can be prevented. Therefore, it is thought that setting of the sheet in the crest is needed to prevent these phenomena.

(5) When the sheet was set whole of the dike, a large bubble appeared between in the dike on the upsream side and the seepage control sheet. Afterwards, the bubble rose in the dike surface with the rising of the phreatic line, and the bubble disapperared. It is thought that the bubble was blow out slowly through the seepage control sheet. The dike inside of the sheet was perfectly protected from overflow, and the effect of the seepage control sheet against air blow and overflow could be checked. However, it is thought that covering the dike perfectly by using the sheet is inefficiency, when thinking about constraction cost and time in the dike of a real scale.

(6) From the analytical result, proposed countermeasure method, installation of the hole in the dike to remove the air, and installation of the seepage control sheet, increases strength of the dike against rainfall and overflow.

ACKNOWLEDGEMENT

The author would like to express his sincere gratitude to Associate Professor Kenichi Maeda at Nagoya Institute of Technology for his continual guidance and encouragement given through the study in his bachelor, master and doctor’s courses and his critical reading of this manuscript. The author also wishes to express his indebtedness to Professor Teruo Nakai and Professor Feng Zhang at Nagoya Institute of Technology for their kind advice and valuable suggestions during the course of this study.

The author would like to emphasize that the present study has been supported by many colleagues and graduates in the Geomechanics Group of Nagoya Institute of Technology. He is grateful to Messrs. Tomohiro Konaka, Tatsuya Imase and Satoshi Shibata for their support. He was vastly indebted to Messrs. Hiroki Hirabayashi, Keisuke Kume, Hisateru Hashimoto, Mamoru Sakai, Yousuke Yamagoshi, Mari Kakefu, Daisuke Kanou, Toshio Yamazaki, Masatoshi Fukuma, Hiroyuki Hoshi and Takashi Matsumoto. He is also grateful to students in Geomechanics Group, especially to Messrs. Nobuhiko Oishi, Emi Nukudani, Tomoyo Yamaguchi, Tomohide Yuasa, Akihiko Kondou and Megumi Tachii for their help.

The author wishes to express his anknowlegement to Professor Takeshi Kodaka at Meijo University, Professor Makoto Nishigaki and Associate Researcher Mitsuru Komatsu at Okayama University, Professor Toshio Sugii at Chubu University, Professor Atsushi Yashima, Associate Professor Masaya Hinokio and Dr. Shuuji Moriguchi at Gifu University, Associate Professor Takashi Matsushima at Tsukuba University, Associate Professor Hossain Md. Shahin and Associate Researcher Mamoru Kikumoto at Nagoya Institute of Technology, Mr. Kanji Baba at Oyo Corporation, and Mr. Takayuki Masuo at Taiyo Kogyo Corporation for their discussion and advice.

The author is grateful to the Japan Society for the Promotion of Science for its financial support with Grants-in-Aid for JSPS Fellows 20-8411.

Finally, and the most importantly, the author is deeply grateful to his family for their support, encouragement, endless love, faith in him and continuously sustaining him.

Hirotaka SAKAI
Nagoya Institute of Technology
December 2009

REFERENCES

1. Akai, K., Ohnishi, Y. and Nishigaki, M. (1977): Finite element analysis of saturated-unsaturated seepage in soil, *Journal of the Japan Society of Civil Engineers,* 264, 87–96 (in Japanese).

2. Asaoka, A. and Kodaka, T. (1992): Seepage failure experiments and their analyses of loose and medium dense sands, *Soils and Foundations*, **32**(3), 117-129.

3. Batchelor, G.K. (1967): An Introduction to Fluid Dynamics, *UK: Cambridge Univ. Press*.

4. Benz, W. and Asphaug, E. (1995): Simulating of brittle solids using smooth particle hydrodynamics, *Computer Physics Communications*, 253-265.

5. Biot, M. A. (1941): General theory of three-dimensional consolidation, *Journal of Applied Physics*, **12**, 152-164.

6. Campbell. J., Vignjevic. R. and Libersky, L. (2000): A contact algorithm for smoothed particle hydrodynamics, *Computer methods in applied mechanics and engineering*, **184**, 49-65.

7. Chunichi Shimbun (2000): 15th September, *Chunichi Shimbun morning newspaper* (in Japanese).

8. Gingold, R. A. and Monaghan, J. J. (1977): Smoothed particle hydrodynamics, theory and application to non-spherical stars, *Monthly Notices of the Royal Astronomical Society*, **181**, 375-389.

9. Hockney, R. W. and Eastwood, J. W. (1999): Computer simulation using particles, *Bristol and Philadelphia*, Institute of Physics Publishing.

10. Israelachvili, J. N. (1991): Intermolecular and surface forces (2nd ed.), *Academic Press*, London.

11. Kamiya, K., Uno, T. and Matsushima, T. (1996): Measurement of the distribution of sandy soil void diameter by air intrusion method, *Japan Society of Civil Engineers*, No. 541/III-35, 189–198.

12. Kodaka, T. and Asaoka, A. (1994): Development phenomenon of bubble in seepage process of the sandy soil, *Journal of Japan Society of Civil Engineers*, 487/III-26, 129–138 (in Japanese).

13. Konaka, T., Sakai, H. and Maeda. K. (2008): Influence of air bubbles on stability of sandy ground against seepage flow, *Proc. of 43th annual conference of JGS*, 548–549 (in Japanese).

14. Leighton, T. G. (1994): The Acoustic Bubble, *Academic Press*, London.

15. Libersky, L. D., Petschek, A. G., Carney, T. C., Hipp, J. R. and Allahdadi, F. A. (1993): High strain Lagrangian hydrodynamics, A three-dimensional SPH code for Dynamic Material response, *Journal of Computational Physics*, **109**, 67-75.

16. Liu, G. R. and Liu. M. B. (2003): Smoothed Particle Hydrodynamics, *World Scientific*.

17. Liu, M.B., Liu, G. R. and Lam, K. Y. (2003): Constructing smoothing functions in smoothed particle hydrodynamics with applications, *Journal of Computational and Applied Mathematics*, **155**(2), 263-284.

18. Lucy, L. B. (1977): A numerical approach to the testing of the fission hypothesis. *Astronomical Journal*, **82**, 1013-1024.

19. Maeda, K. and Sakai, M. (2004): Development of seepage failure analysis procedure of granular ground with Smoothed Par-ticle Hydrodynamics (SPH) method, *Journal of Applied Mechanics,* JSCE, **7**, 775-786. (in Japanese).

20. Maeda, K., Sakai, H. and Sakai, M. (2006): Development of seepage failure analysis method of ground with smoothed particle hydrodynamics, *Structural Engineering / Earthquake Engineering*, 307–319.

21. Martin, J.C. and Moyce, W.J. (1952): An experimental study of the collapse of liquid column on a rigid horizontal plane, *Trans. R. Soc. London*, Ser. A, 244, 312-324.

22. Ministry of Land, Infrastructure, Transport and Tourism (2004): A detailed check of the river dike, http://www.mlit.go.jp/kisha/kisha04/05/050609/03.pdf (in Japanese).

23. Ministry of Land, Infrastructure, Transport and Tourism (2008): Water Information System, http://www1.river.go.jp/ (in Japanese).

24. Miura, K., Hayashi, M. and Yoshida, N. (1991): Applicability of Analytical Methods for Seabed Response to Ocean Waves, *Proc, Geo-Coast '91*, 609–614.

25. Monaghan, J.J. and Gingold, R.A. (1983): Shock simulation by the particle method SPH, *Journal of Computational Physics*, **159**, 290-311.

26. Monaghan J.J. (1988): An introduction to SPH, *Computer Physics Communications,* **48**, 89-96.

27. Monaghan, J.J. (1994): Simulating free surface flows with SPH, *Journal of Computational Physics*, **110**, 399-406.

28. Morris, J. P., Fox, P. J. and Zhu, Y. (1997): Modeling low Reynolds number incompressible flows using SPH, *Journal of Computational Physics*, **136**, 214-226.

29. Nakajima, Y. (1985): Piping in polder dike, *Tsuchi-to-Kiso*, JGS, **13**(2), 83–88 (in Japanese).

30. Nugent, S. and Posch, H. A. (2000): Liquid drops and surface tension with smoothed particle applied mechanics, *Physical Review E*, **64**(4), 4968-4975.

31. Ohnishi, Y. and Nishigaki, M. (1981): Analysis of unsaturated flows, *Tsuchi-to-Kiso*, JGS, **29**(7), 65–72 (in Japanese).

32. Ohnishi, Y. and Nishigaki, M. (1981): Analysis example of unsaturated flows, *Tsuchi-to-Kiso*, JGS, **29**(8), 37–45 (in Japanese).

33. Prevost, J. H. (1979): Mechanics of continuous porous media, Int. J. *Engng Sci.*, **18**, 787-800.

34. Randles, P. W. and Libersky, L. D. (1996): Smoothed Particle Hydrodynamics: some recent improvements and applications, *Computational Methods in Applied Mechanics and Engineering*, **139**, 375-408.

35. Sakai, H. and Maeda, K. (2007): A study on seepage failure of sand ground with account for generation and development of air bubbles, *13th Asian Regional Conference of Soil Mechanics and Geotechnical Engineering*, **1**(2), 571–574.

36. Sakai, H., Sakai, M. and Maeda, K. (2005): Observation on seepage failure of ground around sheet pile with account for evolution of bubbles with PIV, *Proc. of 40th annual conference of JGS* (in Japanese).

37. Sills, G. C., Whehler, S. J., Thomas, S. D. and Gardner, T. N. (1991): Behaviour of offshore soils containing gas bubbles, *Geotechnique*, **41**(2), 227–241.

38. Sugino, T. and Yuu, S. (2002): Numerical analysis of fine powder flow using smoothed particle method and experimental verification, *Chemical Engineering Science*, **57**, 227-237.

39. Takeda, H., Miyama, M. and Sekiya, M. (1994): Numerical simulation of viscous flow by Smoothed Particle Hydrodynamics, *Progress of Theoretical Physics*, **92**(5), 939-960.

40. Techno System Co. Ltd. (2005): Concepts in Basic Bubble and Foam Engineering, 139–153 (in Japanese).

41. Terzaghi, K. (1942): Theoretical Soil Mechanics, *John Wiley and Sons, INC.*, 235–264.

42. The chemical Society of Japan (2004): 5th ed., Chemical handbook (Basic chapter), **2**, 144–149 (in Japanese).

43. The Japanese Geotechnical Society (2003): JGS Technical Committee of mechanism of slope failure and prediction of degree of risk under heavy rains, JGS (in Japanese).

44. The Japanese Geotechnical Society Chubu (2001): Lesson of Tokai floods disaster, JGS (in Japanese).

45. The Visualization Society of Japan (2002): Handbook of Particle Image Velocimetry (in Japanese).

46. Wheeler, S. J. (1988): A conceptual model for soils containing large gas bubbles, *Geotechnique*, **38**, 389–397.

47. Wood, D.M. (2004): Geotechnical modeling, *Oxon, Spon Press*.

48. Yamaguchi, H. (1988): Soil mechanics; Lecture and practice (3rd ed.) (in Japanese).

49. Yamamoto, T. (1977): Wave induced instability in seabeds, *Proc. Coastal Sediments ’77*, ASCE, 898–913.

50. Yamamoto, T., Koning, S. L. and Van Hijum, E. (1978): On the response of a poro-elastic bed to water waves, *Journal of Fluid Mechanics*, **87**(1), 193–206.

51. Yamamoto, T. (1981): Wave-induced pressures and effective stresses in inhomogeneous seabed foundations, *Ocean Engineering*, **8**, 1–16.

52. Zen, K. and Yamazaki, H. (1993): Liquefaction of seabed sand ground due to ocean waves, *Report of Port and Airport Research Institute*, PARI, **31**(5).